



Universitat
de les Illes Balears

MASTER'S THESIS

SEARCHING FOR POST-GLITCH SIGNALS FROM PULSARS WITH GRAVITATIONAL WAVE DETECTORS

Joan Moragues Roca

Master's Degree in Advanced Physics and Applied Mathematics

(Specialisation/Pathway *Astrophysics and Relativity*)

Centre for Postgraduate Studies

Academic Year 2020-21

Searching for post-glitch signals from pulsars with gravitational wave detectors

Joan Moragues Roca

Master's Thesis

Centre for Postgraduate Studies

University of the Balearic Islands

Academic Year 2020-21

Key words:

Gravitational waves, continuous waves, neutron star, pulsar, glitch

Thesis Supervisor's Name: David Benjamin Keitel

Tutor's Name (if applicable)

Tutor's Name (if applicable)

Abstract

Pulsars are neutron stars –remnants of very massive stars– that emit intense electromagnetic radiation and rotate at great speed. Depending on their position and axis of rotation, we can detect this radiation from Earth and catalogue a huge number of these stellar objects. As a consequence of various factors, pulsars may suffer spontaneous increases in their rotation frequency, even though they tend to lose energy over time: this phenomenon is what we know as glitches. It has been widely theorized that glitches make pulsars act as gravitational waves emitters.

With the help of the LIGO and VIRGO detectors, essential for detecting gravitational waves in the past, we aspire to detect the disturbances in space-time produced in this case by the mentioned pulsars, never detected before. These are a particular kind of gravitational waves known as transient continuous waves, because they are fainter and more durable than the waves generated in the merger of two compact objects, already detected, but not lasting as long as truly continuous waves. Specifically, we are looking for signals with duration between hours and months, coming from pulsars that suffered one or more glitches during the Advanced LIGO and Virgo O3 period (between April 2019 and March 2020).

Using electromagnetic ephemerides to have a good estimation of the gravitational wave signal we expect to detect, we will perform a “narrow-band” search: the sky position of the pulsar is fixed, but we allow some uncertainty on the values of the frequency and its derivatives.

We will work with a search pipeline using the \mathcal{F} -statistic and the \mathcal{B} -statistic. The process will go through some preparation steps, mainly to select suitable targets for our purposes and cleaning the Short Fourier Transforms previously generated for each of the detectors.

Using the statistics we will search for relevant points in a template bank formed by the parameters of our search and, if there are no significant outliers, then we will use simulated signal injections to derive upper limits, a test to see at which GW strain we are capable of actually detecting some signal from each target.

Finally, we also want to study the possibility of making more and better detections in the future. On the one hand, analyzing improvements in current detectors, and on the other, thinking about the new detectors that will be available in the next decade.

This work is part of an international, more exhaustive, project with a journal publication, planned to be out in the next months.

CONTENTS

CHAPTER	TOPIC	PAGE NUMBER
1	Gravitational waves	1
1.1	General relativity	1
1.2	Gravitational waves: emission	4
1.3	Gravitational waves: detection	5
1.3.1	Detectors	5
1.3.2	LVC observing runs until now	7
1.3.3	Noise and sensitivity	9
1.3.4	Matched filters	12
2	Neutron stars and continuous waves	15
2.1	Characterization of neutron stars	15
2.1.1	General characteristics	15
2.1.2	Population	16
2.2	Pulsar glitches	18
2.3	Continuous waves	20
2.3.1	Frequency of a CW	21
2.3.2	Amplitude of a CW	22
2.4	Long duration transient GWs	22
3	Search method	25
3.1	CW model and search methods	26
3.1.1	5n-vector narrow-band pipeline	26
3.1.2	\mathcal{F} -statistic method	27
3.1.3	Frequency-domain \mathcal{F} -statistic pipeline for CWs	29
3.2	Transient \mathcal{F} -statistic and \mathcal{B} -statistic	29
3.3	General search procedure	32

4	Search on LIGO-Virgo O3 data	35
4.1	Target selection	36
4.1.1	Processing of catalogs	36
4.1.2	Analysis of promising glitches	37
4.1.3	Glitches reanalysis	38
4.1.4	Indirect upper limits	40
4.2	Data selection	43
4.3	Search setup	46
4.3.1	Signal start times: t_0	48
4.3.2	Signal duration: τ	48
4.3.3	Frequency and spindown bands	49
4.3.4	Evaluation of template bank and runtime estimation	51
4.3.5	Running jobs via condor	52
4.3.6	Determining a threshold for detection candidates	53
4.4	Upper limits	54
4.4.1	General Procedure	54
4.4.2	Setup	55
4.5	Results	57
4.5.1	J1813-1749 full results	57
4.5.2	Preliminary J1105-6107 results	65
4.5.3	Overview of the full search	69
5	Conclusion and future work	71

Chapter 1

Gravitational waves

1.1 General relativity

The general theory of relativity is the current theory that allows us to understand gravity, its behaviour and consequences. This new vision of the universe was first proposed by Albert Einstein in 1915 [1], and it was the generalization of special relativity, published a decade before.

As a consequence of the axioms that the laws of physics are invariant in all inertial systems and that the speed of light in vacuum is the same for all observers –regardless of the motion of the light source–, Einstein introduced the special relativity (SR). Afterwards, the principle of equivalence among others forced the emergence of a generalisation of SR: general relativity (GR). Already in the first one, the concept of spacetime was introduced: the idea that both 3-dimensional space and 1-dimensional time are fused in a 4-dimensional manifold. This idea was crucial because later in GR it gave rise to many new concepts in the field of astrophysics such as the possible existence of gravitational waves.

But before trying to fully understand the key of this project, gravitational waves, one should first deeply understand how spacetime works. First, the Einstein Field Equations (EFE), which show how matter and geometry are related, may be written as:

$$G_{\mu\nu} = \kappa T_{\mu\nu} \tag{1.1}$$

with $G_{\mu\nu}$ the Einstein tensor, $\kappa = \frac{8\pi G}{c^4}$ and $T_{\mu\nu}$ the stress energy tensor.

This equation is basically telling us the relation between the spacetime geometry – described by the Einstein tensor $G_{\mu\nu}$ – and the stress-energy tensor $T_{\mu\nu}$, which describes the density and flux of energy and momentum. So, in other words, matter curves spacetime, and similarly, spacetime makes matter flow in a particular way.

Defining the constants $c = 1$, $G = 1$, introducing the Ricci curvature tensor $R_{\mu\nu}$, the scalar curvature R and the metric tensor $g_{\mu\nu}$ we can rewrite (1.1) as:

$$G_{\mu\nu} = R_{\mu\nu} - \frac{1}{2}Rg_{\mu\nu} = 8\pi T_{\mu\nu} \quad (1.2)$$

The EFE are crucial to understand some astrophysical objects and events, which could not be properly described before the theory of relativity. One example could be black holes (regions where the manifold is so curved that not even light can escape from it), and, of course, gravitational waves. So given the fact that the EFE are non-linear tensor equations, highly difficult to solve –even though they might seem simple as we express them in 1.2–, to derive the (simpler) equations behind the GWs, one should try to work with a linearized version.

First, we assume the metric tensor $g_{\mu\nu}$ as a Minkowski metric $\eta_{\mu\nu}$ with some small perturbation:

$$g_{\mu\nu} = \eta_{\mu\nu} + \epsilon h_{\mu\nu}, \quad 0 < \epsilon \ll 1 \quad (1.3)$$

Here we have just developed the curvature terms of 1.3 in 0 and 1 powers of ϵ . Also, general relativity, just like electromagnetism has a gauge freedom related with the choice of coordinate system. In this case the “Transverse Traceless” gauge is a convenient choice, where

$$h_{0\mu} = 0, \quad h^\mu{}_\mu = 0 \quad (1.4)$$

Now defining

$$\bar{h}_{\mu\nu} = h_{\mu\nu} - \frac{1}{2}\eta_{\mu\nu}h_{\alpha\beta}\eta^{\alpha\beta} \quad (1.5)$$

and introducing the D’Alembertian operator, we obtain

$$\square \bar{h}_{\mu\nu}^{TT} = 2\kappa T_{\mu\nu}, \quad \square = \eta_{\mu\nu}\partial^\mu\partial^\nu \quad (1.6)$$

And with a null stress-energy tensor, $T_{\mu\nu} = 0$, the equation becomes the gravitational wave equation:

$$\square h_{\mu\nu}^{TT} = 0 \quad (1.7)$$

This equation first derived by Einstein [1][2][3] at the beginning of the 20th century predicts the existence of perturbations in the Minkowski space that travel at the speed of light. These are perturbations perpendicular to the direction of propagation of the waves. Henri Poincaré previously proposed them in 1905 [4] and called them gravitational waves,

and recently, approximately 100 years later, they have been detected for the very first time [5].

As mentioned above, using the suitable TT gauge to describe these perturbations allows us to write

$$h_{\mu\nu}^{TT}(x) = \begin{pmatrix} 0 & 0 & 0 & 0 \\ 0 & h_+ & h_\times & 0 \\ 0 & h_\times & -h_+ & 0 \\ 0 & 0 & 0 & 0 \end{pmatrix} \exp[ik \cdot x] \quad (1.8)$$

This is essentially the equation of a wave propagating in the \hat{z} direction with dependence on h_+ and h_\times , which are the amplitudes of the two perpendicular polarizations. As we can see in figure 1.1, these two polarizations have a 45° difference in the direction of perturbation.

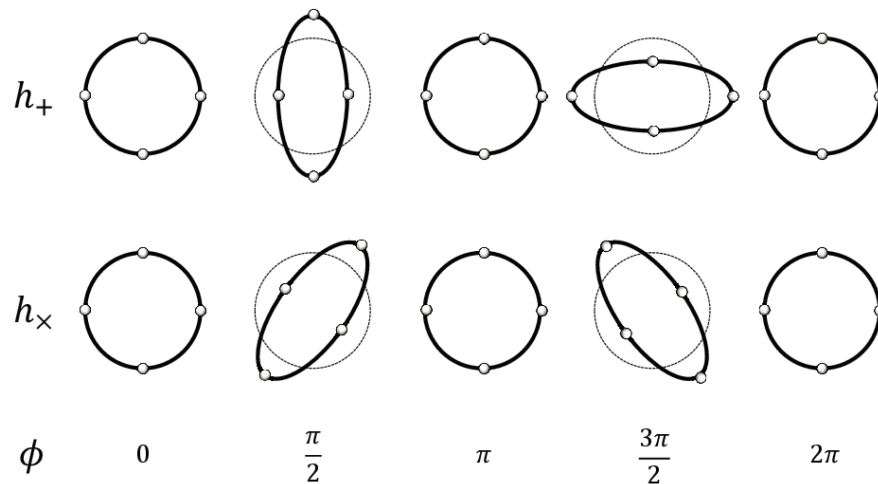


Figure 1.1: Result of both $+$ and \times polarizations in a ring of test particles. When we have a phase multiple of π , the ring maintains its spherical symmetry, but otherwise it warps in different directions depending on the polarization (with a difference of 45°), reaching its maximum elongation at $(n + \frac{1}{2})\pi$. Credit: [6]

Summarizing, gravitational waves are perturbations of the spacetime itself, travelling at the speed of light, caused by high energy processes –as we will go over in the following section– which can be studied with two complementary polarizations.

1.2 Gravitational waves: emission

In astrophysics, when we talk about extremely high energy processes we should immediately think of extremely massive and dense objects, like black holes or neutron stars. When a pair of this kind of objects orbit each other they generate perturbations in the spacetime around them that start travelling in the form of waves. In fact, the peak of intensity of a GW occurs when these two objects collide, when the release of energy is at its maximum. This is what we call “Compact Binary Inspiral Gravitational Waves”. On the other hand, GWs can also be the result not of two compact objects colliding, but just orbiting each other long before merging, or even a single star rotating about its axis with some kind of irregularity on it. Since they evolve over longer periods, these sources produce significantly weaker gravitational waves: continuous waves, the ones that we study in this project and will be explained in detail in [Chapter 2](#). Some other gravitational wave emitters could be supernovae, which would cause what is called a “Burst Gravitational Wave”, a kind of wave that we have not detected yet, or even “Stochastic Gravitational Waves”, e.g. a cosmological background, again, not detected yet.

An important difference between this kind of waves and electromagnetic waves is that GWs interact less with matter, so even though they are difficult to detect, they bring us much clearer information of the sources that have produced them. Another difference is that, in electromagnetism, radiation can be emitted by a dipole source ($l = 1$); only monopolar emissions are not possible due to charge conservation. Instead, gravitational waves only allow quadrupoles ($l = 2$) as the lowest multipole. Both monopoles and dipoles are forbidden due to mass conservation and momentum conservation, respectively.

From equation [1.6](#) we can derive the gravitational radiation:

$$h^{\mu\nu} = -\frac{\kappa}{4\pi} \int_V d^3x' \frac{T^{\mu\nu}(t - |\vec{x} - \vec{x}'|, \vec{x}')}{|\vec{x} - \vec{x}'|} \quad (1.9)$$

Which implies that the amplitude of the wave depends on the second derivative in time of the quadrupole moment of the source:

$$h^{\mu\nu} = \frac{2G}{r c^4} \ddot{\mathcal{J}}_{jk}(t - r/c), \quad \mathcal{J}_{jk} = \int \rho(x) \left[x_j x_k - \frac{1}{3} r^2 \delta_{jk} \right] d^3x \quad (1.10)$$

Being \mathcal{J} the mass-quadrupole moment of a source with weak internal gravity, expressed in terms of the mass density $\rho(x)$. In the quadrupole formalism one can also define the energy emission rate L_{GW} [\[7\]](#):

$$L_{\text{GW}} = \frac{G}{5c^5} \langle \ddot{\mathcal{J}}_{jk} \ddot{\mathcal{J}}^{jk} \rangle \quad (1.11)$$

This has only recently been tested: it was 1974 when the existence of gravitational waves

was indirectly proven, thanks to the discovery of a binary pulsar [8] which should emit GWs. As a result, the astrophysics community put more and more effort into trying to achieve the gigantic task of finding them, until on September 14, 2015, LIGO was finally capable to detect and quantify the gravitational waves emitted by two colliding black holes [5]. In other words, the search for GWs signals is a very modern field, but even so we have improved a lot our techniques and capacity of detection.

1.3 Gravitational waves: detection

One of the reasons why it took so long to detect GWs is the fact that even though they are highly energetic events, they take place at billions of light-years away, so when they finally reach the Earth they are much weaker and hard to detect. This leads to important detectability problems that we will go through in this section.

1.3.1 Detectors

The instruments in charge of achieving this difficult task are the so called interferometers. Those are instruments used in many science fields that combine two laser beams to study the interference pattern that they create. Albert Michelson in 1887 first used an interferometer with which him and Edward Morley disproved the existence of “aether” [9]. LIGO detectors [10] have basic similarities with that first Michelson-Morley interferometer: they have two perpendicular arms –that is why we say that they are L-shaped, as we can see in [Figure 1.2](#)–, and a laser beam is emitted, then passes through a beam splitter and it is reflected in one mirror at the end of each arm. After bouncing back from the two arms, both laser beams meet each other at the central beam splitter, which makes them go to the photodetector and form an interference pattern there. Measuring the fringes in the photodetector one can conclude if light has travelled under the same conditions through the different arms.

The basic idea in order to detect GWs is that when some event takes place, the space stretches and compresses in perpendicular directions (as discussed earlier in [figure 1.1](#)), the length of the arms change and the light beams travelling through different arms do no longer make the same interference pattern they did under “normal” conditions. If we set the length of the interferometers’ arms to be L and ΔL is the differential change between the two arms, then the strain of an event can be easily calculated with:

$$h = \frac{\Delta L}{L} \quad (1.12)$$

What is relevant here is that with a weak signal like the ones we aim to detect, changes in length of the arms can be very small: 10000 times smaller than the diameter of a proton.

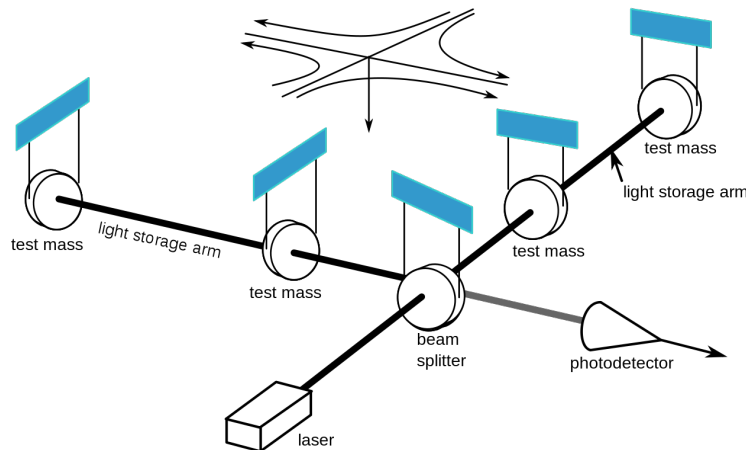


Figure 1.2: Diagram of a gravitational wave interferometer. Credit: [11]

To achieve this precision we cannot work with a simple Michelson interferometer. This is why GW detectors are special, because they have important differences with any other existing interferometer. With arms of 4 km of length, the LIGO detectors are the biggest ones ever created. As has been mentioned, we need an enormous precision to detect GWs, and the more distance the light travels, the more precision we will obtain. In fact, 4 km would not be enough if it was not for another improvement: Fabry Perot cavities. These are made by additional mirrors placed in each arm which allow every light beam to bounce between those mirrors and the ones at the end of each arm before merging both beams at the center of the instrument, as mentioned before. This process increases LIGO’s sensitivity first by building up the light, and second by increasing the distance travelled by it.

There are other modifications of the LIGO interferometer with respect to the classic Michelson. For example an increasing laser power (that allows the instrument to generate sharper fringes to observe) thanks to power recycling mirrors. They also possess “signal recycling” mirrors to enhance the signal received by the photodetector and mechanisms to damp out vibrations from the environment that would cause noisy signals continuously. Finally, in order to make the motion of the test masses (mirrors) equivalent to those of free-falling ones within the local gravitational field, they have to be suspended in some way, supporting against gravity but enabling free movement. Our interferometers contain a pendulum suspension system for each test mass to mitigate all the seismic noise, as discussed further down in [figure 1.5](#).

Currently we work with two interferometers from LIGO, located at opposite sides of the US, one in Hanford and the other in Livingston, and since 2007 one detector from Virgo [12], in Italy. The two LIGO ones are pioneers in the gravitational wave detection project, and they operate in coincidence to filter out local noise. Also we want preferably at least two detectors –before the incorporation of Virgo it was only these two interferometers

operating— to calculate better the direction and polarization of a GW by measuring the difference between times of detection for each detector.



Figure 1.3: Operative interferometers from LIGO in Hanford (top left) and Livingston (bottom right), Virgo in Italy (bottom left) and the most recent KAGRA in Japan (top right). Credit: [13]

1.3.2 LVC observing runs until now

Since the first gravitational wave detection in 2015, the LSC has grown both in number of scientists and technological capacity. But that is the result of nearly half a century of work, since the early MIT studies on interferometers and noise estimations in 1972 [14]. The first working detectors operated for the “Initial LIGO” project, which started in 2002 and lasted until 2010. During those years, as mentioned, a new observatory -from the Virgo Collaboration- in Europe started working in coordination with LIGO, but no gravitational wave signal was detected.

It was then between 2010 and 2015 when the interferometers were improved significantly to achieve sufficient precision and sensitivity, as it is explained in detail further down. From 2014 on, the new “Advanced LIGO” project raised the expectations of the whole field and started with a first run, O1 in 2015-2016. Finally, on September 14th, 2015 the first signal of gravitational waves from two colliding black holes was detected [5]. Two more events were also detected during that periods: in October 12th, a binary black hole

merger (not significant enough to claim an unambiguous detection) and two months later, another binary coalescence signal, just before the end of O1 [15].

Following O1, two more runs have been done so far: O2, from December 2016 to August 2017, and O3, from April 2019 to March 2020.

During O2 not only other signals from colliding black holes were detected [16], but also the first detection of gravitational waves from colliding neutron stars was achieved [17].

Finally, during O3, the last run to date, 39 new CBC events were catalogued only in the first part of the run, during 6 months [18]. In addition to these new events, 8 continuous waves related works were made, with special relevance for this project.

The first CW published paper with data from O3 was released on July 28, 2020 [19]. It had the objective of placing constraints on the GW emission from five pulsars, and with the improved sensitivity they could look below the spindown limit of two millisecond pulsars (meaning they spin very rapidly, typically reaching periods of some milliseconds) for the first time.

After that, a more general search using a variation of the Hough transform [20], the “BinarySkyHough” [21], was made. They tried to find CWs from unknown NSs in unknown binary systems in the most sensitive band of the detectors [22] [23].

Two studies centered on J0537-6910 (a pulsar that we will work with in this project) have also been done, trying to reveal why this pulsar is slowing down very rapidly –due to the fact that it is losing energy faster than any of the other known pulsars–, [24] [25]. The last one, published in April 29, 2021, 4 months later than the previous one, tested if the star is being spun down mainly by gravitational waves due to r-mode oscillations, which are a kind of fluid waves that exists in rotating stars, caused by the Coriolis force. The results excluded the possibility that this pulsar is a high mass neutron star emitting gravitational waves due to r-modes.

Afterwards, two papers were released at the end of May and one more on July 1st, 2021. The first of them [26] was a search for CWs from young supernova remnants (SNRs), which covered fifteen young SNR between 100 and 10000 years old. These objects are expected to contain NSs on their centers, with unknown frequency of rotation. The second one [27] was focused on trying to find out if and with what strength dark photons can couple to the interferometers, and the results indicated that it is no bigger than one part in 1040 of the electromagnetic coupling for all ultralight masses. And the third one [28] was a search for non-axisymmetric NSs, looking for isolated stars everywhere in the sky.

Finally, the most recent CW publication up to date was released on September 20, 2021, and it is centered on continuous GWs from a specific category of neutron star: accreting millisecond X-ray pulsars (AMXPs) [29]. The pulsars that receive this name feed off another star, located nearby, and pull matter from it onto their surface, and also emit X-ray pulses and spin at a high frequency.

None of these studies reported any CW detection.

Returning to the general calendar of GW observation runs, more recently, and before the COVID-19 pandemic forced the project to stop in March 2020, a new observatory in Japan, the “Kamioka Gravitational Wave Detector” (KAGRA), joined LIGO and VIRGO collaboration –during the second part of O3– [30], forming the LVK community.

1.3.3 Noise and sensitivity

One of the constant goals of the LVK is to increase more and more the sensitivity of the instruments that we are using. The most important improvements are the ones made to the interferometers themselves, as has been already mentioned in the [Detectors section](#). But to deeply understand why they are necessary and what we are achieving with these improvements, we need to start understanding what is limiting our capacity of detection.

Starting from the luminosity equation in, 1.11, one can deduce the strain h of GWs emitted from a rotating deformed NS:

$$h = 10^2 \frac{G}{c^4} \frac{\epsilon I_{zz} f^2}{d} \sim 3 \cdot 10^{-25} \left(\frac{\epsilon}{10^{-6}} \right) \left(\frac{I_{zz}}{10^{38} \text{kgm}^2} \right) \left(\frac{f}{100 \text{Hz}} \right)^2 \left(\frac{100 \text{pc}}{d} \right) \quad (1.13)$$

where d is the distance to the neutron star, f is the frequency of GWs and I_{zz} is the principal moment of inertia. The ellipticity, ϵ , is given by

$$\epsilon = \frac{|I_{xx} - I_{yy}|}{I_{zz}}. \quad (1.14)$$

Typical maximum strains for compact binaries (CBs) are of the order of 10^{-21} , so it is easy to see how the instruments must be very sensitive in order to observe them.

In other words, any event with a typical strain not greater than 10^{-21} causes a displacement in the LIGO detectors of less than 10^{-18} meters: it would be impossible to detect any of the signals without a huge instrumental sensitivity.

The biggest enemy of the interferometers in order to precisely detect and quantify gravitational waves is noise. We define the Power Spectral Density (PSD) in order to quantify all kind of noise with one single function. We assume that the noise is white or coloured Gaussian –as will be shown next– and also stationary over a limited time:

$$\langle \bar{n}(f) \bar{n} * (f') \rangle = \frac{1}{2} \delta(f - f') S_n(f) \quad (1.15)$$

where S_n is the one-sided PSD, only relative to the positive frequencies, with units of inverse frequency. But the most commonly used variable is the Amplitude Spectral Density (ASD), or the square root of S_n .

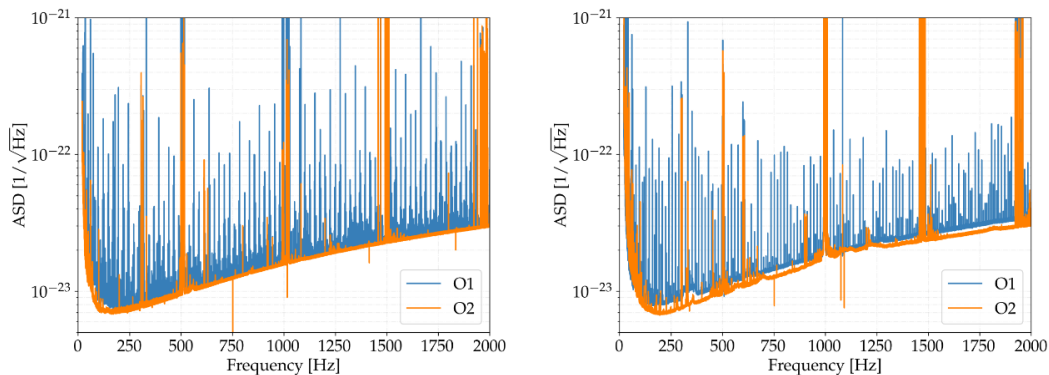


Figure 1.4: Livingston (left) and Hanford (right) amplitude spectral densities for the last two runs, O1 and O2. Credit: [31]

In figure 1.4 one can appreciate the typical shape of the LIGO sensitivity curve -ASD-, very similar for both Livingston and Hanford interferometers.

Noise can appear as a result of instrumental vibrations, or natural seismic movements, even thermal and quantum fluctuations, affecting different ranges of frequencies. In fact, the reason why the ASD and PSD curves have this typical shape is only due to the fact that each mechanism affects the sensitivity of the interferometers at different frequencies. For example, seismic and thermal noise dominate at low frequencies. The former is caused by inevitable ground vibration, only mitigated by the multistage seismic isolation system, and the latter is caused by the motion of the center of mass of the test mass driven by thermal fluctuations, and acquires more importance at higher frequencies. On the other hand, from 20 or 30 Hz on, coating brownian noise and specially quantum noise, dominate the curve. In fact, at high frequencies –1000 Hz– quantum fluctuations of light are nearly the only kind of noise that survives. And no matter how sophisticated the interferometer could be, it will always present quantum noise issues.

Besides these noise contributors one should not forget that there are also many other noisy vibrations in the surroundings, either for natural causes or due to human activity. For that reason interferometers should ideally be built as far away from civilization as possible and in seismically stable regions.

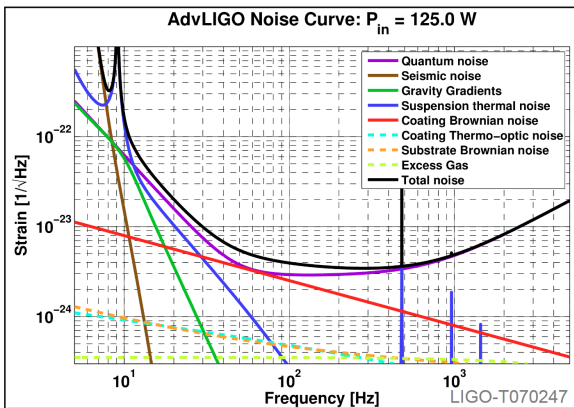


Figure 1.5: Different contributors to detector noise depending on frequency. Credit: [32]

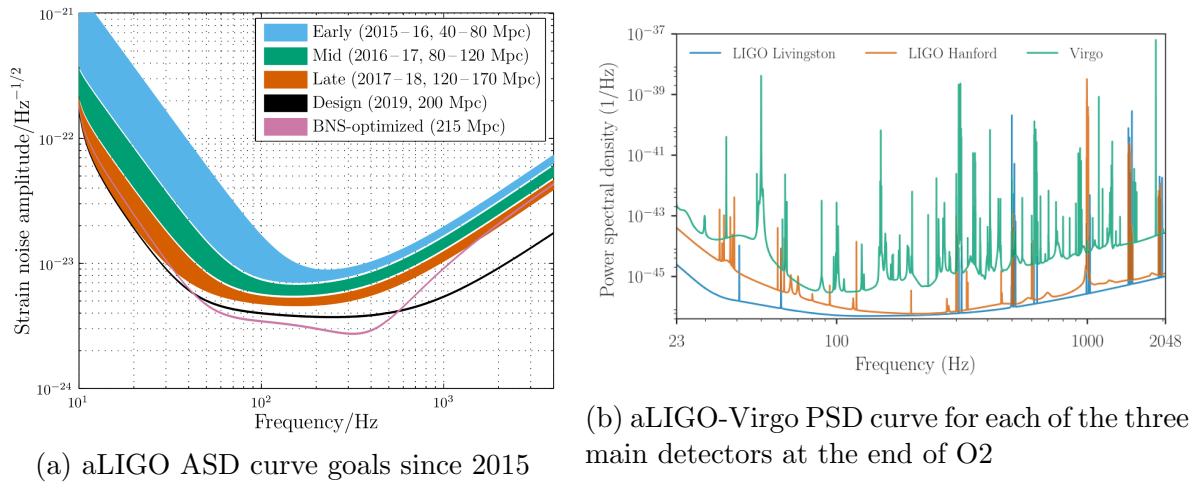


Figure 1.6: Sensitivity of LIGO and Virgo detectors. Credits: [33] [34]

Moreover, comparing the strain of the typical events we aim to detect, we can observe the importance of the improvement of the sensitivity of the detectors -shown in [figure 1.6a](#)-.

Another final topic we will go over in this section is the existence of typical spectral disturbances that we call *lines*. Lines are these peaks one can see in [figure 1.4](#) or [figure 1.6b](#), caused by instrumental artifacts. Many of them have known origin. For example, for the US detectors, at $60n$ Hz, typical lines always show up, as well as the lines that appear at 50 Hz harmonics in the Virgo detector, due to the frequencies of AC transmission in the US and in Europe. There are also what is called *violin lines* and *calibration lines*. Violin lines are caused by the excitation of suspended mirrors due to thermal reasons, and calibration lines are inserted on purpose by moving the mirrors at the end of the detectors arms to calibrate the instrument. Those line are different depending on the detector.

Finally, there are some other lines the origin of which is not yet well understood. For example, looking at [figure 1.4](#) is pretty easy to see how a high number of unknown lines disappeared from O1 run to O2.

Summarizing, gravitational waves are extremely weak and require an enormous precision of the detectors in order to be studied. There are also several issues that lead to noise in the interferometers, so they are in constant update to achieve sufficient precision for our purposes.

In fact, gravitational waves produced by a single spinning neutron star are the weakest, not detected, events so far, more than those caused by a Compact Binary Coalescence. In [figure 1.7](#) a comparison between the typical strain of some classical expected source types and the sensitivity curve of the detectors show how, if we want to detect GWs emitted by a pulsar, we could in principle do it now with any of the LIGO-Virgo-Kagra interferometers, but not with the original LIGO and Virgo ones from the initial run. This shows us the importance of the characterization of the noise, briefly shown in this section.

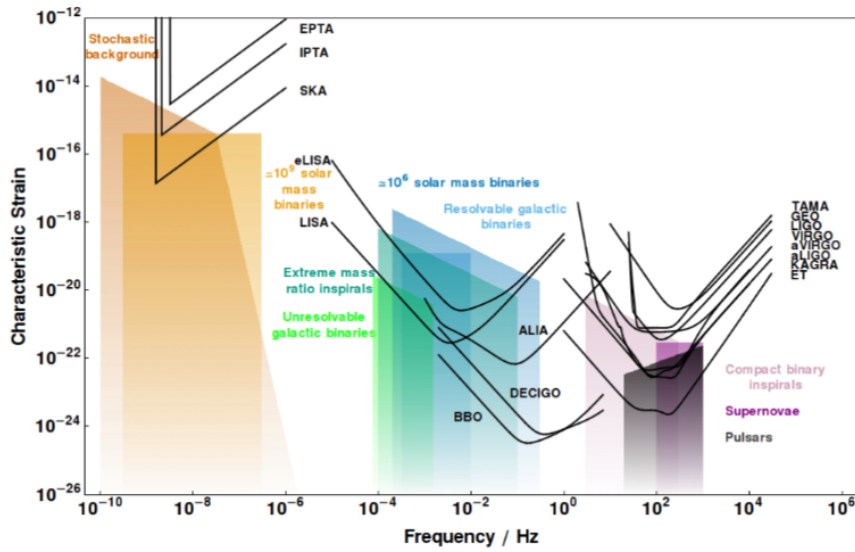


Figure 1.7: Characteristic ASD for different detectors with typical strain of different events. Credit: [35]

In [chapter 2](#) we will go through this particular kind of waves in more detail.

1.3.4 Matched filters

As we will discuss in further sections, the process of detecting any type of signal requires often the ability of differentiating unknown and undesired noise from the clean signal we are looking for. For this purpose, matched filters are commonly used in a huge number of applications, such as the analysis of signals of radars and sonars (for the study of some signal that has been sent and is reflected back), digital communications, image processing and, of course, gravitational waves astronomy. In this section we will discuss the general idea behind these filters following the notation of [36], in order to later apply it to GWs.

Matched filters work by correlating the known signal –or template– with the measured data, in order to detect the presence of that template. It is the same as a convolution process (a operation that produces, from two given functions, a third one that expresses how the shape of one is modified by the other) between the noise and the template. Specifically, a filter matched to a physical waveform $s(t)$, with arbitrary constants k and Δ , is:

$$h(\tau) = ks(\Delta - \tau) \quad (1.16)$$

This is, taking the original signal $s(t)$, reversing it to obtain $s(-\tau)$, then delaying it by

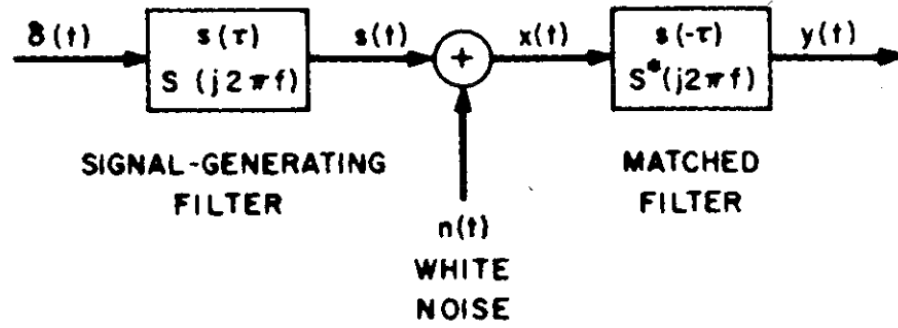


Figure 1.8: Basic idea of a matched-filter process. Credit: [36]

Δ seconds to get $s(\Delta - \tau)$ and finally multiplying its amplitude by a k factor. Then, the transfer function of a matched filter is the Fourier transform of this last impulse response [36]:

$$\begin{aligned}
 H(j2\pi f) &= \int_{-\infty}^{\infty} h(\tau) e^{-j2\pi f\tau} d\tau = k \int_{-\infty}^{\infty} s(\Delta - \tau) e^{-j2\pi f\tau} d\tau = \\
 &= k e^{-j2\pi f\Delta} \int_{-\infty}^{\infty} s(\tau') e^{j2\pi f\tau'} d\tau' \quad (1.17)
 \end{aligned}$$

Defining $\tau' = \Delta - \tau$. Taking into account that

$$S(j2\pi f) = \int_{-\infty}^{\infty} s(t) e^{-2j\pi ft} dt \quad (1.18)$$

Then we find the relation

$$H(j2\pi f) = k S(-j2\pi f) e^{-j2\pi f\Delta} = k S^*(j2\pi f) e^{-j2\pi f\Delta} \quad (1.19)$$

So the transfer function is equivalent to the complex conjugate of the spectrum of the clean signal to which we are matching.

To finish with this introduction on matched filters, we can take a look at how the process is described in [36] and consider the scheme of figure 1.8. We have a signal $x(t)$, constructed from the sum of the clean signal $s(t)$ and a white noise signal $n(t)$. Once this final waveform has passed through the matched filter, we have an output $y(t)$, which may be resolved into two components:

$$y(t) = y_s(t) + y_n(t) \quad (1.20)$$

with the contribution of only $s(t)$ in the first component and only $n(t)$ in the second. The component of this output response function corresponding to $s(t)$ is

$$y_s(t) = \int_{-\infty}^{\infty} h(\tau)s(t - \tau)d\tau = \int_{-\infty}^{\infty} s(-\tau)s(t - \tau)d\tau \quad (1.21)$$

since $h(\tau) = s(-\tau)$, as can be seen in the [figure above](#).

All this process will be revisited and explained in detail for the particular case of CWs in [chapter 3](#), with the corresponding adapted notation.

Chapter 2

Neutron stars and continuous waves

2.1 Characterization of neutron stars

2.1.1 General characteristics

With radius not much greater than 10 km and around 1.4 solar masses, neutron stars are the densest material objects in the universe, only surpassed by black holes. They were first proposed by Walter Baade and Fritz Zwicky in December 1933 [37], only one year and a half after the discovery of neutrons [38]. The other big discovery related to these stellar objects was made by Jocelyn Bell Burnell and Antony Hewish, when they discovered pulsars in 1967 [39]. As it is explained below, pulsars are the result of this kind of stars emitting electromagnetic radiation.

Neutron stars are the remnants of a main-sequence star with more than 8 times the mass of the sun. When that star has exhausted all its nuclear fuel, the core becomes iron-rich and more mass is accumulated there, until the Chandrasekhar limit is exceeded. When this happens, temperatures start increasing enormously and it begins a process of neutron formation via electron capture: that is why they are called neutron stars [40].



Besides the formation of neutrons in the star's core, this process also creates a flood of neutrinos, which oppose to the infalling envelope, resulting in a supernova and leaving the neutron star on its center. Also, this remnant could become a black hole if it had sufficiently high mass (more than approximately 3 solar masses).

At the end, these objects have typically between $1.1 M_\odot$ and $2.16 M_\odot$ [41]. Once they have been formed their temperature reaches its maximum and start to decrease very rapidly during the first years of existence, due to the high amount of energy released by

the neutrinos they emit. Once formed, their typical temperature is about 10^{11} or 10^{12} K, while after a few years it has decreased to “just” 10^6 K. Their densities, as mentioned before, are the most characteristic property of these stellar objects: they can reach orders up to 10^{17} kg/m³ on its center. Another interesting fact is their intense magnetic field, which can also reach incredible values: nearly 10^{11} tesla.

The surface of a neutron star is expected to be made of ordinary atomic nuclei –possibly iron– crushed into a solid lattice with electrons moving between them. But it could be possible that in fact iron and other heavy elements sink beneath the surface, and the nuclei could be basically helium and hydrogen. It is believed that they have a very thin “atmosphere”, of about only some micrometres, highly related to the star’s magnetic field [42].

As one goes deeply inside a NS, an increasing numbers of neutrons can be found in the nuclei, which are stable because they are subjected to enormous pressures which prevent the nuclei decay. But at increasing depths, free neutrons coming from nuclei –due to neutron drip– are more present, so there we could find nuclei, free electrons and free neutrons.

Some aspects of the interior of these objects remain still unknown, like the composition of the superdense matter in their core. One theory describes the core as superfluid neutron-degenerate matter, principally neutrons, with some protons and electrons, but it can be possible that matter takes other forms, like degenerate strange matter, matter containing high-energy pions and kaons in addition to neutrons or ultra-dense quark-degenerate matter [43].

A highly relevant property of these objects is that, while being created, when the mentioned supernova takes place, the resulting neutron star maintains its angular momentum, but now it has significantly less mass than before, so the moment of inertia also decreases and the resulting object spins a lot faster than before. In other words, these are titanic objects spinning at an enormous frequency, inevitably perturbing space-time and, possibly, as we will discuss later, emitting gravitational waves.

2.1.2 Population

About 3,000 known neutron stars have been catalogued in the Milky Way and nearby galaxies so far, but it is believed that there are around the order of 10^8 [44]. The most common way to identify these objects is by detecting pulsar emission, so the majority of these 3000 neutron stars are pulsars. In fact, neutron stars with more than 1 million years of life, approximately, are not longer detectable as pulsars with current technology, so they could only be detected through black body radiation and gravitational effects on other stars.

Besides pulsars, there is another kind of neutron stars: magnetars. These are stars with a very strong magnetic field (commonly between 10^9 and 10^{11} T) and with low frequency

of rotation in comparison with the majority of pulsars. They emit burst of X-rays and gamma rays, and they can be harder to detect than pulsars. Actually, only 24 magnetars have been catalogued so far, with 6 more candidates not yet confirmed. On the other hand, pulsars emit electromagnetic radiation which can be easily detected as long as it points to the Earth, and, in opposition to magnetars, they have usually shorter periods. These periods are sometimes useful in different applications. For example, in 1984, not long after being observed for the first time, some pulsars had a more accurate period than atomic clocks [45], even though this can not be extrapolated to pulsars in general [46]. Also, some stars can be considered both magnetars and pulsars. This happens when the extremely intense magnetic field of a magnetar decays and provides it the electromagnetic power needed to emit radiation. There are only 6 known neutron stars considered magnetars and pulsars.

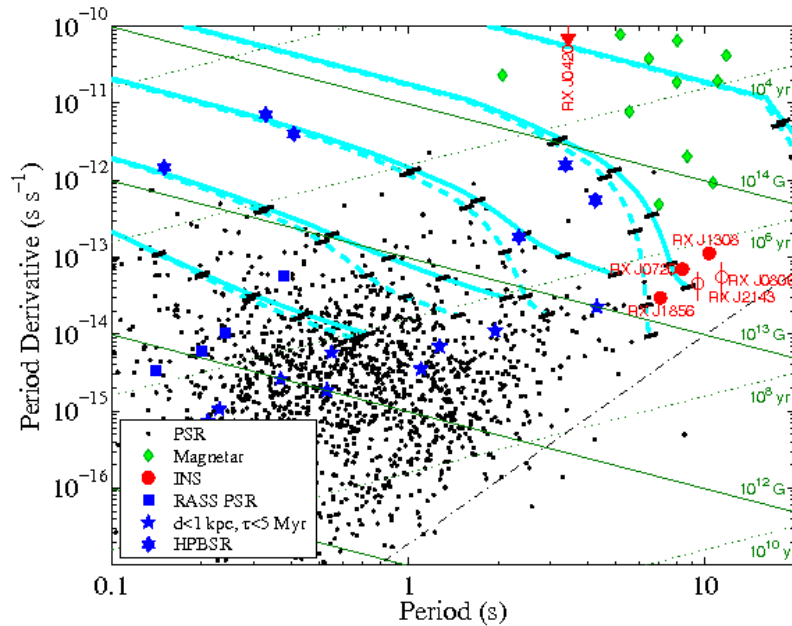


Figure 2.1: Neutron stars population, period derivative vs period. This figure includes all kinds of NS (pulsars –PSR– and Magnetars [47]) as well as lines of constant magnetic field and age. The red circles are targets of interests for the study from where this image is taken, and the nearby/young pulsars are blue five-pointed stars. Credits: [48]

In figure 2.1 we can appreciate the properties of the different kinds of neutron stars mentioned above. Magnetars appear in the top right corner as they have the strongest magnetic fields of the whole set, and they have also high period P and period derivative \dot{P} . Note that not all the catalogued neutron stars appear in this figure, just the ones with $P > 0.1$, i.e, stars that rotate a maximum of 10 times per second. Pulsars with higher frequency are mainly from binary systems –two stars orbiting each other–, and with high probability they are “recycled”: first-born neutron stars that are spun up by accreting matter and angular momentum from the other star of the binary [49].

This particular figure shows the distribution of neutron stars in terms of its period of rotation and its period first derivative, which is a consequence of energy loss through mainly electromagnetic emission. Since pulsars are constantly emitting not only electromagnetic, but possibly also gravitational radiation, they slow down over time. But in order to quantify this phenomenon, from now on we will use the pulsar frequency f and derivative \dot{f} .

But even though we expect pulsars to decrease their rotational frequency, they sometimes suffer a particular and interesting change: a sudden increase of their frequency of rotation, before starting a relaxation phase during which it returns to a value closer to the original frequency. We call these events “glitches”, a process that could also lead to GWs emission.

2.2 Pulsar glitches

In [sections 2.1.1](#) we have gone through some model of the interior of a neutron star. As we can see in [figure 2.2](#) we are still trying to fully characterize the interior of these stars, but we have some notions that help us understanding why pulsars suffer these sudden increases of their rotational frequency we call glitches. Specifically, the outer and inner crust provide us some information for this purpose.

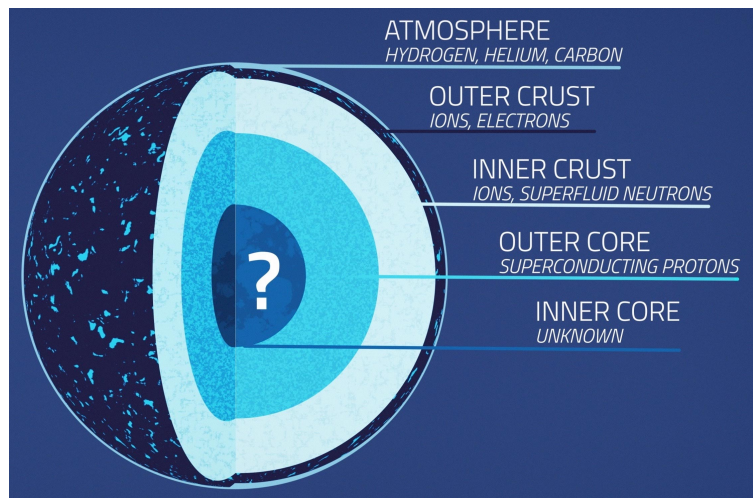


Figure 2.2: Interior of a neutron star. Credits: [\[50\]](#)

The inner crust, as already explained, is made of superfluid neutrons among others, and rotates at an angular velocity Ω_S . On the other hand, the outer layer, with angular velocity Ω , slows down over time. This velocity is proportional to the frequency at which we observe the pulses, associated with the magnetic field of the star. We can then define the difference between the two rotating velocities for the two different layers:

$$\Delta\Omega = \Omega_S - \Omega \quad (2.2)$$

It is believed that when this $\Delta\Omega$ reaches some critical value, an instability takes place and part of the angular velocity of the inner crust is transferred to the outer crust. This way, the angular velocity associated to the frequency of observation of the pulses, Ω increases and we detect a glitch.

When one of these events take place we can always differentiate two parts. First, the secular spin-down (represented by the lower dashed lines in the figure below) and second, the glitch itself. We can quantify the total change in frequency $\Delta f(t_g)$, which is the sum of the transient part Δf_t and the permanent part Δf_P (in the figure below every frequency related parameter is referred to with ν instead of f). Moreover, the changes in the frequency derivative at different orders should be considered as well.

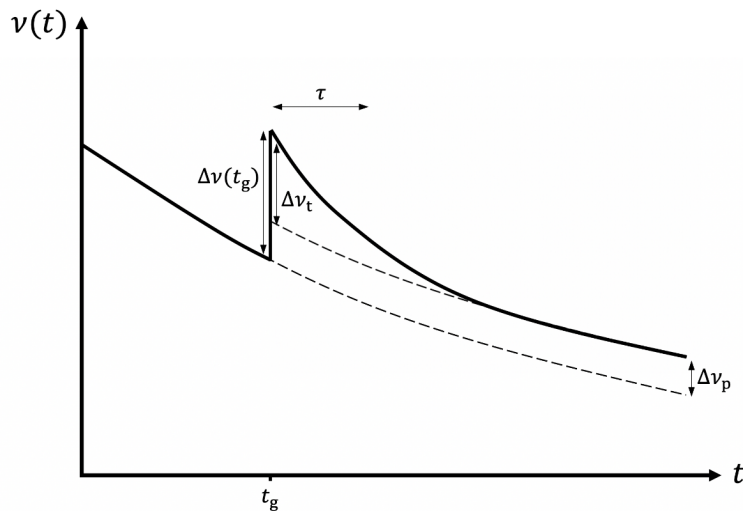


Figure 2.3: Simple representation of the effect of a glitch on the frequency of rotation $\nu(t)$ of a neutron star. Here the change in first time derivative $\Delta\dot{\nu}_P$ has been set to zero. Credit: [51]

Another plausible scenario for the generation of GWs in neutron stars are starquakes. A starquake takes place when the crust of a neutron star undergoes a sudden adjustment caused by huge stresses in the surface of the star. In essence, this event consists of cracking the NS's crust, which alters the stellar axial symmetry by creating a non-null ellipticity. All this process can lead also to gravitational waves emission [52] [53].

These processes can lead commonly to an abrupt change in quadrupole moment of the star, which is expected if gravitational waves are emitted. These GWs would be from a particular kind: long duration transient continuous waves. But before digging into that, we will go first through some more general introduction of continuous waves.

2.3 Continuous waves

Those gravitational waves which are emitted constantly and present an approximately fixed frequency are called “continuous waves”. Logically, they can be differentiated from transient gravitational waves, which are produced during a limited time, typically from two compact objects colliding. Moreover, this last type of waves are more catastrophic and easier to detect: when two objects with the characteristic gigantic masses and densities of a black hole or a neutron star collide, the amplitude of the generated gravitational waves is much greater.

The case of a single rotating pulsar is pretty different. When it presents some irregularity on its surface –this is, when it does not have perfect spherical or axisymmetric shape, but has some deformity on a particular place, like a mountain– it suffers a variation of the mass quadrupole. In fact this could also be due to an inconsistency between the pulsar’s magnetic field and its rotation axis. Consequently, gravitational waves are generated: as mentioned, we expect a weaker wave, constant in time, instead of a short, more intense signal.

Another system causing continuous waves is one with two compact objects in orbital motion but at sufficiently large distance, so long before the merge. This would lead to GWs at a particular frequency range that we can not cover nowadays with our current detectors, but we expect to be able to do it in the future, with the new generation detectors, like the Laser Interferometer Space Antenna (LISA) [54].

A relevant characteristic of these waves is that they actually will not be detected as a constant frequency wave over time, and this is consequence of two facts. First of all, the neutron star is losing energy as it is emitting electromagnetic radiation and, possibly, gravitational waves (we have gone through this at the [beginning](#) of the chapter). This loss of energy directly causes the star itself to slow down. The second reason is related to the detectors on Earth. As the Earth is moving with respect to the neutron star (rotating around its own axis and also orbiting the Sun), the frequency of the observed signal in the detector varies significantly due to the Doppler effect.

In [figure 2.4](#) one can appreciate the way the wave is modulated given these ef-

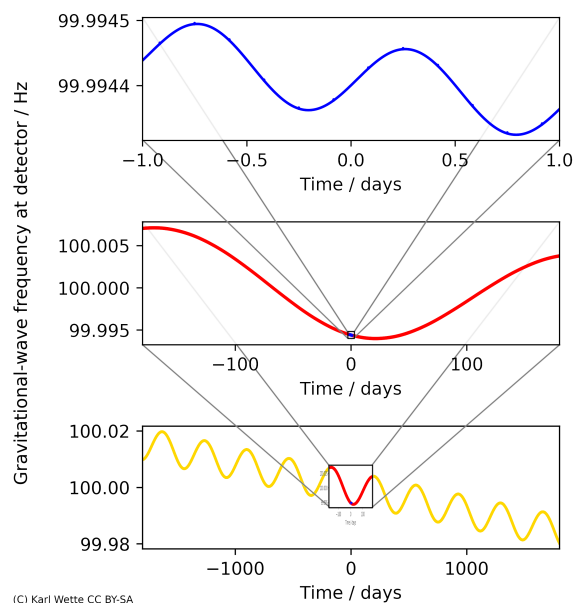


Figure 2.4: Long-term frequency evolution of a continuous wave. Credit: [55]

fects. In the top panel, in blue, the change in frequency of the signal due to the rotation of the Earth can be appreciated; the second panel in red shows the variations during a whole year, consequence of the Earth's motion around the Sun; and in yellow in the bottom panel one can see the slow down of the star, which makes the signal also decrease.

2.3.1 Frequency of a CW

That frequency of a particular continuous wave depending on τ , the proper time, is given by [56]:

$$f_{\text{NS}}(\tau) = \frac{1}{2\pi} \frac{d\Psi_{\text{NS}}(\tau)}{d\tau} = \frac{1}{2\pi} \frac{d}{d\tau} \left(\Phi_0 + 2\pi \sum_{k=0}^s \frac{f_{\text{NS}}^{(k)}}{(k+1)!} \tau^{k+1} \right) = \sum_{k=0}^s \frac{f_{\text{NS}}^{(k)}}{k!} \tau^k \quad (2.3)$$

Here, f_{NS}^k is the derivative of the frequency at order k evaluated at $\tau = 0$. To find the frequency we expect to detect at the interferometer, we should go first from the frame of the source to the Solar System Baricenter (SSB) and finally from there to the detector's frame. Now, if the star is moving linearly and uniformly with respect to the SSB, this is:

$$r_{\text{NS}}(t) = r_0 \mathbf{n}_0 + v_{\text{NS}} \mathbf{n}_v \left(t + \frac{r_0}{c} \right) \quad (2.4)$$

Here, $\mathbf{n}_v = \mathbf{v}_{\text{NS}}/v_{\text{NS}}$ and $v_{\text{NS}} = |\mathbf{v}_{\text{NS}}|$, where \mathbf{v}_{NS} is the velocity vector of the neutron star. Also, with $r_0 = |\mathbf{r}_{\text{NS}}(t = -r_0/c)|$ and $\mathbf{n}_0 = \mathbf{r}_{\text{NS}}(t = -r_0/c)/r_0$, one can show that there is the following relation between the coordinate time t' at the moment of emission, the time when the phase was observed at the SSB t and the proper time τ :

$$\tau = \sqrt{1 - \beta_{\text{NS}}^2} \left(t' + \frac{r_0}{c} \right), \quad t = t' + \frac{|\mathbf{r}_{\text{NS}}(t')|}{c} \quad (2.5)$$

with $\beta_{\text{NS}} = v_{\text{NS}}/c$.

So the phase from both SSB frame and NS frame are linked as:

$$\Psi_{\text{SSB}}(t) = \Psi_{\text{NS}}(\tau(t)) \quad (2.6)$$

Now we can derive the frequency observed at the SSB from the corresponding phase Ψ_{SSB} analogously to equation 2.3:

$$f_{\text{SSB}}(t_{\text{SSB}}) = \frac{1}{2\pi} \frac{d\Psi_{\text{SSB}}(t_{\text{SSB}})}{dt_{\text{SSB}}} = \frac{1}{2\pi} \frac{d}{dt_{\text{SSB}}} \left(\Phi_0 + 2\pi \sum_{k=0}^s \frac{f^{(k)}}{(k+1)!} t_{\text{SSB}}^{k+1} \right) = \sum_{k=0}^s \frac{f^{(k)}}{k!} t_{\text{SSB}}^k \quad (2.7)$$

Finally, the frequency at the detector frame is:

$$f(t) = f_{\text{SSB}}(t) \left(1 + \frac{\vec{v}(t) \cdot \vec{n}(t)}{c} \right) \quad (2.8)$$

With \vec{v} the velocity of the detector relative to the SSB, \vec{n} the sky position of the star relative to the detector, and introducing the relation between the time of the detector, t and t_{SSB} depending on $\Delta\vec{r} = \vec{r} - \vec{r}_0$, the displacement of the detector from the initial position:

$$t_{\text{SSB}} = t - t_0 + \frac{\Delta r(t) \cdot \vec{n}(t)}{c} \quad (2.9)$$

2.3.2 Amplitude of a CW

We have already talked about the strain of a gravitational wave in the [first chapter](#); it can be easily described as:

$$h_+(\tau) = A_+(\tau) \cos \Phi(\tau) \quad (2.10)$$

$$h_\times(\tau) = A_\times(\tau) \sin \Phi(\tau) \quad (2.11)$$

And for the case of continuous waves, these two amplitudes are:

$$A_+ = \frac{1}{2} h_0 (1 + \cos^2 \iota) \quad (2.12)$$

$$A_\times = h_0 \cos \iota \quad (2.13)$$

As we can see, the amplitude is proportional to an overall constant factor h_0 , the physical meaning of which will be introduced later, but it also depends on the angle between the axis of rotation of the star and the vector of its direction towards the detector, ι .

2.4 Long duration transient GWs

Some gravitational waves, and in particular, the ones we try to study in this project, have properties that lie somewhere between transient waves and truly continuous waves. These waves are not continuous for infinite time, but they are surely not transient waves –much

more brief, from the order of milliseconds–. This is the reason why we talk about long duration transient continuous waves.

Transient continuous waves can be produced by different kinds of sources. For example, from newborn, rapidly evolving NSs produced in supernova explosions or binary neutron star (BNS) mergers [57] [58], or from the already stated glitches, on a mature NS.

The model we use for the general frequency evolution of a (possibly glitching) pulsar is

$$f(t) = f_{\text{Taylor}}(t) + f_{\text{glitch}}(t) \quad (2.14)$$

If no glitch is observed for a particular pulsar, then only the first term for the long-time spindown evolution is relevant:

$$f_{\text{Taylor}}(t) = \sum_{k=0}^N \frac{f^{(k)}(t - T_{\text{ref}})^k}{k!} \quad (2.15)$$

with a reference time T_{ref} and up to N frequency derivatives $f^{(k)}$ (also denoted in this work with \dot{f} , \ddot{f} and \dddot{f} etc. for the successive derivatives). Each GW search method can typically address up to a different maximum of frequency orders N . For example, the code used in the present work can analyse up until \ddot{f} .

For glitching pulsars, the additional term is

$$f_{\text{glitch}}(t) = \Theta(t - T_{\text{gl}}) \left[\sum_{k=0}^M \frac{\Delta f_{\text{gl}}^{(k)}(t - T_{\text{gl}})^k}{k!} + \delta f_{\text{R}} e^{-(t - T_{\text{gl}})/\tau_{\text{R}}} \right] \quad (2.16)$$

with multiple such terms for repeating glitches. In this expression, $\Theta(x)$ is the Heaviside step function, T_{gl} is the glitch time, $\Delta f_{\text{gl}}^{(k)}$ with $M \leq N$ are the permanent jumps in the frequency and its derivatives at order k , δf_{R} is the part of the frequency jump that relaxes back, and τ_{R} is the relaxation time, which is not necessarily observed for all glitches. The glitch term is typically a small correction on top of $f_{\text{Taylor}}(t)$.

In previous sections we have seen the mathematical description of the strain of a continuous wave, in equations 2.10 and 2.11. These are the two polarizations of the incoming signal, but the GW signal received by the detector is not the same:

$$h(t) = F_{+}(t; \hat{n}, \psi) h_{+}(t) + F_{\times}(t; \hat{n}, \psi) h_{\times}(t), \quad (2.17)$$

where $F_{+, \times}(t; \hat{n}, \psi)$ is the detector response at time t to $+$ and \times polarized gravitational waves from direction \hat{n} with polarization angle ψ [56].

The amplitude has already been stated in a [section 2.3.2](#). However, as equation 2.14 is written in the source frame, there is a timing correction for the signal received at the detector. One first thing to take into account is proper motion of the star. Proper motion is the observed change in position in the sky of an astronomical object seen from the center of mass of the Solar System. It is characterized with right ascension and declination parameters, and it has dimensions of angle per time (arcseconds per year). But in this case, proper motions between the pulsar and the solar system can usually be ignored [60], and in this analysis we do not cover sources in binary orbits as in [22], for example, but the correction between solar system barycenter and detector frame, already discussed, is a crucial part of the analysis methods described in the following sections.

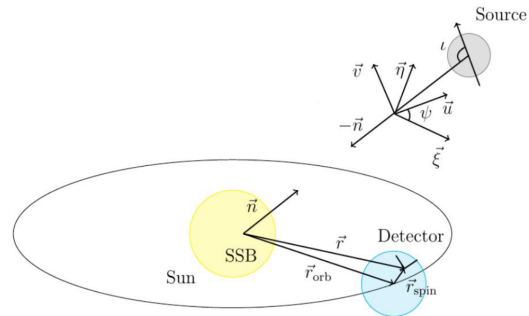


Figure 2.5: Scheme of different frames, including ψ angle between the source frame and the detector frame. Credit: [59]

Chapter 3

Search method

To perform the search, we need to start from some known parameters for the different targets. This is the reason why we use electromagnetic ephemerides, because they provide us a good estimation of the gravitational wave signal we aim to detect. In other words, if we know how fast are pulsars rotating (by detecting from the Earth the electromagnetic beam they emit), then we expect GWs to present a frequency related to that rotational frequency we can estimate. In particular, considering a rigid rotation of the star –the standard model– we expect the gravitational signal to present a frequency twice the rotation frequency, but sometimes it can also be expected at the same frequency, for example when the star is precessing, or even at other ratios, for some fluid modes, like the r-mode.

In this work we perform a “narrow-band” search, which means that we fix the phase-evolution parameters of the signal: the sky position and the frequency, as well as its derivatives, or spindowns; but, instead of using a particular values from an electromagnetic ephemerides, like in “targeted searches”, we allow some uncertainty in those frequency and spindown values, around the electromagnetically determined ones. We are considering that the electromagnetic ephemerides might not be perfectly accurate and also, a frequency mismatch could exist due to physical reasons. Moreover, it is quite possible that a particular GW signal is coming from deeper inside the neutron star than the electromagnetic emission, so this would be another reason for the EM and GW frequencies not being perfectly related. For a nominal emission frequency f_{GW}^0 this mismatch can be parameterized defining

$$\Delta f_{GW} = \delta f_{GW}^0 \tag{3.1}$$

and thus we will search in the following range:

$$f_{\text{GW}} \in \left[f_{\text{GW}}^0 - \frac{1}{2}\Delta f_{\text{GW}}, f_{\text{GW}}^0 + \frac{1}{2}\Delta f_{\text{GW}} \right] \quad (3.2)$$

If the neutron star is freely-precessing, Δ will be proportional to the angle between the symmetry axis and the star rotation axis. The order of magnitude of delta should be around 10^{-4} in order to accommodate the different astrophysical models [61].

In this context, different pipelines can be used to perform the searches. The LVK paper that this work is part of [62] uses three different pipelines: the narrow-band 5n-vector search –a mature pipeline used in both O1 and O2 data–, a new narrow-band search pipeline using the \mathcal{F} -statistic, both for continuous waves, and a transient version of the last one, again using the \mathcal{F} -statistic but also the \mathcal{B} -statistic. Even though, in the present work we will use exclusively this last method.

3.1 CW model and search methods

In the current section we will explain the two previously mentioned processes to detect continuous waves –the 5n-vector search and the \mathcal{F} -statistic–, different from many others also used in CW searches, like the targeted and the all-sky searches. After that, we will focus on the particular model for transient continuous waves, where the \mathcal{B} -statistic will be also discussed.

Our CW signal model depends on two sets of parameters, the frequency-evolution parameters $\lambda = \{f^{(k)}, \alpha, \delta\}$ and the amplitude parameters $\mathcal{A} = \{h_0, \cos \iota, \psi, \phi_0\}$. The search method for the long-duration transient CWs, explained below in the [next section](#), is quite similar to the standard CW model, but with a window function in time and some additions and differences.

But before going with that, we will briefly introduce the fully coherent 5n-vector and \mathcal{F} -statistic pipelines, which is necessary to understand the transient \mathcal{F} -statistic and \mathcal{B} -statistic methods that we use here. These two first methods are used in the project of which this work is part, based on a search over a narrow range of gravitational wave frequencies and spindowns centered on the central estimated values from the source ephemerides.

3.1.1 5n-vector narrow-band pipeline

The *5n-vector narrowband pipeline* is a method explained in detail in [63]. It is based on the 5n-vector method, described in [64][65] in order to search for CWs in a narrow frequency and spindown range around the source ephemerides.

The method uses correlated data from the detectors to first build a collection of 1024s long Fast Fourier Transforms (FFTs). Then the first cleaning step is performed: in the time domain the undesired short-duration disturbances that can affect these FFTs are suppressed [66]. Then, a narrow frequency band around the expected GW frequency and first order spindown $-f$ and \dot{f} is extracted for each target. For this purpose one has to take into account the CW modulations that will be later applied in the search, so this narrow band has to be sufficiently large.

Afterwards, and again for each particular target, the Doppler modulation in the time domain due to the relative movement between frames has to be corrected. The procedure requires using a non-uniform downsampling to just 1 Hz. With this time-series, two matched filters, one for each polarization of the wave can be used and construct this way a complete detection statistic S , combining coherently the matched filter results from all detectors [63] for each template in the f and \dot{f} space. This mentioned detection statistic is defined as

$$S = |H_+|^2 |A_+|^4 + |H_\times|^2 |A_\times|^4, \quad (3.3)$$

where $A_{+/\times}$ are the the Fourier components of $F_{+/\times}(t; \hat{n}, \psi = 0)$ and $H_{+/\times}$ are GW amplitude estimators built from the data Fourier components and $A_{+/\times}$. For the size of the template bank bins, only the time-series duration has to be taken into account: on the one hand, its size in frequency is just the inverse of the time-series duration and on the other, the spindown bin size is given by the square inverse of that duration. At the end, among all the values of the spindown that have been considered, the local maximum of a detection statistic in every 10^{-4} Hz band has to be selected.

3.1.2 \mathcal{F} -statistic method

A commonly used method in continuous waves detection is what is known as \mathcal{F} -statistic, first derived in [56]. Following the steps of [67] and [68], with the observed data x , we want to decide between two hypotheses: \mathcal{H}_G is the hypothesis that the observed data consists only of Gaussian stationary noise (we split the data into SFT bands, as will be explained later, and we assume in each band the noise is stationary), while \mathcal{H}_{tS} suppose that the data contains also a transient CW signal $h(t, \theta)$. We can define the likelihood for the data x in the Gaussian noise case $P(x|\mathcal{H}_G)$ and the likelihood of having a signal, $P(x|\mathcal{H}_{tS})$:

$$\mathcal{H}_G : x(t) = n(t) \longrightarrow P(x|\mathcal{H}_G) = \kappa e^{-\frac{1}{2}\langle x|x \rangle} \quad (3.4)$$

$$\begin{aligned} \mathcal{H}_{tS} : x(t) = n(t) + h(t; \mathcal{A}, \lambda) &\longrightarrow P(x|\mathcal{H}_{tS}) = \\ &= \kappa e^{-\frac{1}{2}\langle x-h(\mathcal{A})|x-h(\mathcal{A}) \rangle} = P(x|\mathcal{H}_G) e^{\mathcal{A}^\mu \langle x|h_\mu \rangle - \frac{1}{2} \mathcal{A}^\mu \langle h_\mu|h_\nu \rangle \mathcal{A}^\nu} \end{aligned} \quad (3.5)$$

With the scalar product defined as:

$$\langle x|y \rangle = \sum_x \frac{1}{S_n^X} \int_0^T x^X(t)y^X(t)dt \quad (3.6)$$

Once we know these quantities we can then compute the likelihood ratio $\Lambda(x, \theta)$ and the log likelihood ratio –this is analogous to the matched-filter formulation we have seen in [section 1.3.4](#) for extracting a signal $s = h(t, \theta)$ from data x :

$$\Lambda(x, \theta) = \frac{P(x|\mathcal{H}_G)}{P(x|\mathcal{H}_{tS}, \theta)} \quad (3.7)$$

$$\log \Lambda(x, \theta) = \langle x|s \rangle - \frac{1}{2} \langle s|s \rangle = \mathcal{A}^\mu x_\mu(\lambda) - \frac{1}{2} \mathcal{A}^\mu \mathcal{M}_{\mu\nu}(\lambda) \mathcal{A}^\nu \quad (3.8)$$

with

$$x_\mu(\lambda) = \sum_{X=1}^{N_{\text{det}}} \langle x^X | h_\mu^X \rangle, \quad \mathcal{M}_{\mu\nu} = \left\langle \frac{\partial h}{\partial \mathcal{A}^\mu} \middle| \frac{\partial h}{\partial \mathcal{A}^\nu} \right\rangle \quad (3.9)$$

and proceed with the maximum-likelihood approach for the amplitude, which consists on finding a point (\mathcal{A}_{ML}^μ) for which the derivative on amplitude vanishes:

$$\frac{\partial \log \Lambda(x, \mathcal{A}, \lambda)}{\partial \mathcal{A}^\mu} = x_\mu(\lambda) - \mathcal{M}_{\mu\nu}(\lambda) \mathcal{A}^\nu = 0 \longrightarrow \mathcal{A}_{ML}^\mu(x, \lambda) = \mathcal{M}^{\mu\nu}(\lambda) x_\nu(\lambda) \quad (3.10)$$

And the so-called \mathcal{F} -statistic is the result of introducing this maximum likelihood point into the log likelihood test statistic:

$$2\mathcal{F}(x, \lambda) = x_\mu \mathcal{M}^{\mu\nu}(\lambda) x_\nu \quad (3.11)$$

An important consideration is that we can always define an offset as the difference between the template parameters and the Doppler parameters of the actual signal contained in the data ($\Delta\lambda = \lambda - \lambda_S$). Then, due to this offset, we have a relative loss in the expected \mathcal{F} -statistic, so conveniently we use a dimensionless mismatch, depending on the mismatched $(\text{SNR})^2$, ρ^2 , to quantify this loss:

$$m_{\mathcal{F}}(\mathcal{A}, \lambda_S; \Delta\lambda) = \frac{\rho^2(0) - \rho^2(\Delta\lambda)}{\rho^2(0)} = g_{ij}^{\mathcal{F}}(\mathcal{A}, \lambda) \Delta\lambda^i \Delta\lambda^j + \mathcal{O}(\Delta\lambda^3) \quad (3.12)$$

Where the second equality is based on the deduction that the mismatched $(\text{SNR})^2$ is $\rho^2(\Delta\lambda) = \rho^2(0) - \mathcal{A}^\mu \mathcal{G}_{\mu\nu ij} \mathcal{A}^\nu \Delta\lambda^i \Delta\lambda^j + \mathcal{O}(\Delta\lambda^3)$, and the \mathcal{F} -statistic metric $g_{ij}^{\mathcal{F}}$ is:

$$g_{ij}^{\mathcal{F}}(\mathcal{A}, \lambda) = \frac{\mathcal{A} \cdot \mathcal{G}_{ij}(\lambda) \cdot \mathcal{A}}{\mathcal{A} \cdot \mathcal{M}(\lambda) \cdot \mathcal{A}} \quad (3.13)$$

3.1.3 Frequency-domain \mathcal{F} -statistic pipeline for CWs

This method is based on the frequency-domain \mathcal{F} -statistic pipeline [69] [70]. This pipeline is used in a number of coherent and semi-coherent search strategies, including the project that this work is contributing to [62], in which a fully coherent search over the full dataset is performed.

As we have just seen, the \mathcal{F} -statistic is a matched filter which is maximized over the amplitude parameters \mathcal{A} of the quasi-monochromatic signals. For each target the search is done over the range of GW frequency f and spindowns \dot{f} , \ddot{f} ... with matched-filter templates chosen using the multi-detector \mathcal{F} -statistic metric [70], which is called through the LALSuite program [71] `lalapps_Weave` [72]. The analysis uses a set of 1800 s Tukey-windowed short Fourier transforms (SFTs) over the full data span for all three detectors, and produces a detection statistic for each matched-filter template.

Finally, in both this and the *5n-vector narrowband* pipelines, the 95% confidence level upper limits $h_0^{95\%}$ on the CW amplitude can be computed. To do that one has to inject several simulated gravitational wave signals in each 10^{-4} Hz sub-band. This process will be explained in detail later.

3.2 Transient \mathcal{F} -statistic and \mathcal{B} -statistic

The model we use for transient CWs is not quite the same as the one for continuous waves. In fact, when we work with general continuous waves, we use a special case of the transient CWs model. The model, first proposed by [67] is intended for transient CWs and takes the characteristics of a standard CW, namely a quasi-sinusoidal emission with a well-defined, slowly varying frequency described by parameters $\lambda = \{f^{(k)}, \alpha, \delta\}$, and amplitude parameters $\mathcal{A} = \{h_0, \cos \iota, \psi, \phi_0\}$. The difference resides on the addition of a set of transient parameters: $\mathcal{T} = \{t_0, \tau\}$, with t_0 the start time and τ a duration parameter, of the order of typically hours to months.

We can then think of a transient CW $h(t, \theta)$ as a standard continuous wave, modulated by a window function:

$$h(t, \theta) = h(t, \lambda, \mathcal{A}, \mathcal{T}) = \omega(t, \mathcal{T})h(t, \lambda, \mathcal{A}) \quad (3.14)$$

In other words, $h(t, \lambda, \mathcal{A})$ is the standard CW signal. The window function is ω and it

limits the signal in time: it turns the wave on at time t_0 , and it turns it off after its lifetime, determined by the τ parameter.

We can use different kinds of window functions ω . Of course, the simplest and less costly is a rectangular window. This has basically the effect of assuming the CW to exist between times t_0 and $t_0 + \tau$, without modifying it in any sense: before and after this time interval there is no signal. But there are lots of other possible windows we could use; for example the exponential window makes great physical sense. In our case, we are considering a window that starts at time t_0 just like the rectangular one and decreases exponentially until the end of the window. Since exponential functions never reach null values, it is common to cut the signal at time 3τ .

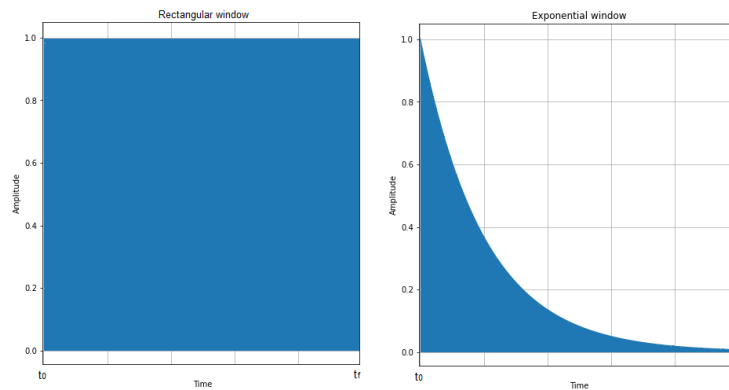


Figure 3.1: Rectangular and exponential windows. Credit: [73]

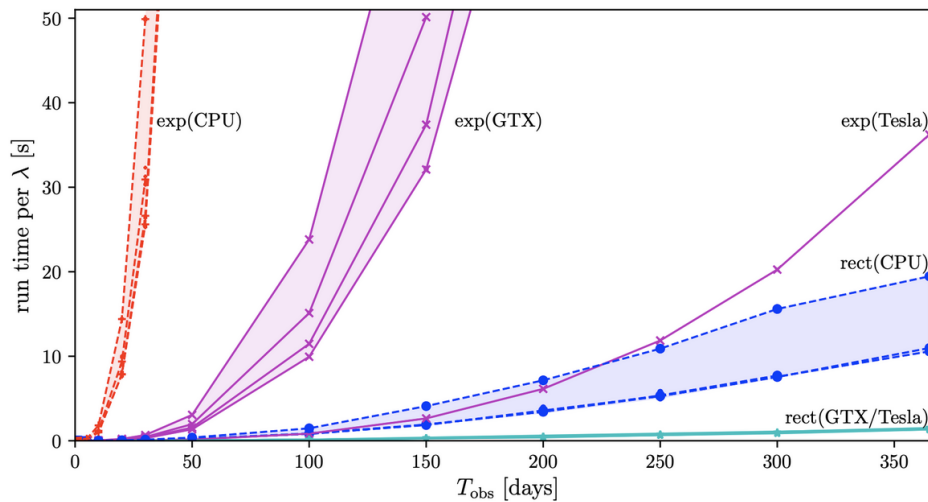


Figure 3.2: Timing results for both rectangular and exponential transient windows, from CPU and GPU implementations on various devices. Credit: [74]

With this exponential window, one can achieve a higher signal to noise ratio (SNR) if the true signal is also exponential [51], but is much more computationally expensive in

comparison to the rectangular one. In fact, the maximum loss of the rectangular window compared to the more realistic exponential-decay window has already been estimated as acceptable [67] [75], so the rectangular is the one used in this project.

We have already gone through the derivation of the CW \mathcal{F} -statistic procedure, which consists of maximizing over the amplitude parameters [56], so we are left with a statistic only dependent on the frequency λ and transient \mathcal{T} parameters. Now, working with transient CWs, two paths can be followed in order to find relevant points in the parameter space.

On the one hand, we can search the maximum over the transient parameters (the transient \mathcal{F} -statistic), and on the other we can marginalize over those parameters (the \mathcal{B} -statistic). The first one has already been introduced, and corresponds to the example of the image on the right: at fixed λ , from all the points in our τ , t_0 space we find the one with a maximum value.

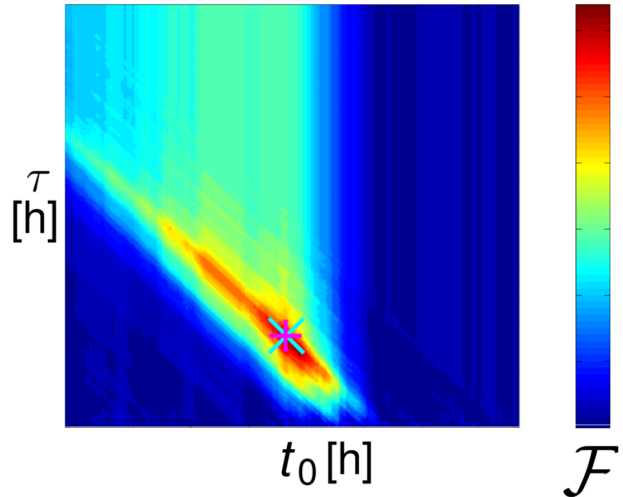


Figure 3.3: Example of maximum approach procedure for the \mathcal{F} -statistic. Credit: D. Keitel

In order to understand the second one, we need to begin with introducing the Bayes factor $\mathcal{B}_{tSG}(x)$, which will be used to compare the hypothesis that our data contains a transient signal \mathcal{H}_{tS} with the hypothesis that it consists only of Gaussian noise \mathcal{H}_G :

$$\mathcal{B}_{tSG}(x) = \frac{P(x|\mathcal{H}_{tS})}{P(x|\mathcal{H}_G)} = \int_{\mathbb{P}} \Lambda(x; \theta) P(\theta|\mathcal{H}_{tS}) d\theta \quad (3.15)$$

with $\Lambda(x; \theta)$ the likelihood ratio introduced in section 3.1.3. But to define properly this factor we have to introduce the prior probabilities on the parameters we marginalise over (amplitude and transient). After some calculations one can deduce the definitive transient Bayes factor. This is for the usual \mathcal{F} -statistic amplitude priors and uniform priors on the transient parameters t_0 and τ , with λ constant.

$$\mathcal{B}_{tSG}(x; \lambda) = \frac{70}{\hat{\rho}_{\max}^4 \Delta t^0 \Delta \tau} \int e^{\mathcal{F}(x; \lambda, \tau)} dt^0 d\tau \quad (3.16)$$

Basically we calculate this factor, dependent on λ , to be evaluated at each grid point and find the highest values, using the standard statistic.

Regardless of the method that we use, we then have to decide on a threshold, above which we consider that there can be a candidate. This calculation is made using the Gumbel distribution, and will be explained in the [corresponding section](#) in next chapter.

To sum up all this statistic procedure, we chose our pulsar target, of which we know its sky coordinates: right ascension and declination are fixed parameters. Then we use a grid of templates covering a subset of the parameter space in frequency and its derivatives (f , \dot{f} , $\ddot{f} \dots$). The number of derivatives depends on if they are available in the ephemerides of every target, and is also limited by our code (`lalapps_ComputeFStatistic_v2` contained in `LALSuite` [71], which can take up until \ddot{f} , as has been already stated. For each point of this parameter space we then compute the transient \mathcal{F} -statistic map by calculating partial sums, corresponding to all the t_0 , τ combinations, of the Short Fourier Transform ingredients of the statistic. After doing so, we will pick relevant points of the parameter space using one of the two statistics explained before. Finding clear outliers would mean that we would have a detection candidate for these particular parameters values.

3.3 General search procedure

Here we present a summary of the general procedure, and in the next chapter we will go through it in detail. First of all, we have to perform some data preparation steps: we split the data into 1800s long Short-Fourier-Transforms and proceed with quality studies and some cleaning steps. Then we set up the grid, the template bank, for which, as mentioned, we use combinations of different frequency orders. Again, the grid dimensions depend on the number of spindown orders we have available.

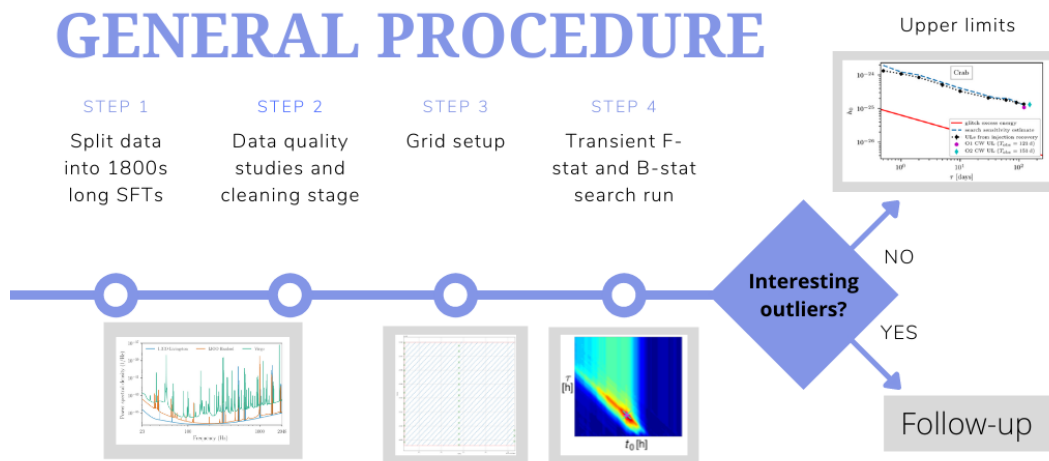


Figure 3.4: Schematic summary of search procedure.

After that we can start running the search for each target, always being aware of the computing costs, following the methods already stated in this chapter. Depending on

whether there are significant outliers we can then take one of two separate paths. If there is any detection candidate, we follow them up. In the absence of significant candidates, we set upper limits $h_0^{95\%}$ at 95% confidence for each target using the software-injection scheme that will be explained in the next chapter. Just as an example, here an upper limits result from a previous paper on LIGO O2 data has been included:

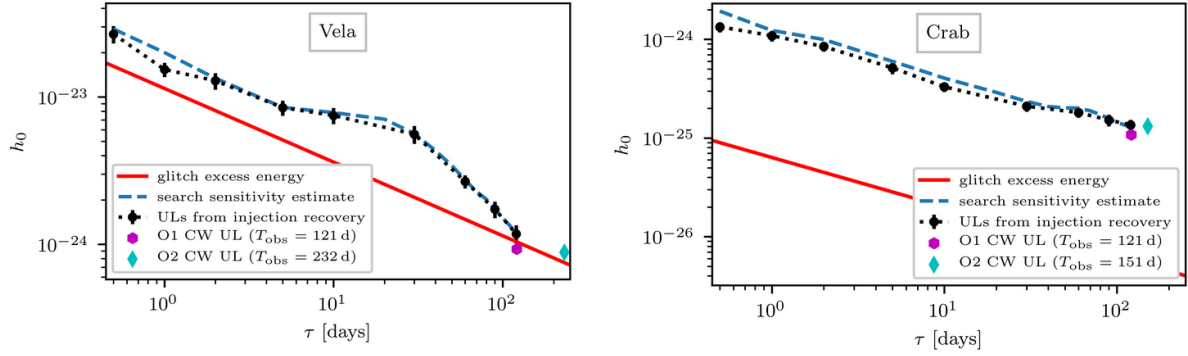


Figure 3.5: Example plot of upper limits of Vela and Crab pulsars found by [75] using LIGO O2 data as a function of τ

Chapter 4

Search on LIGO-Virgo O3 data

In this chapter we present the procedure we follow for our work, as well as some of the final results we obtain. This procedure is structured in four steps.

The [first step](#) is to select suitable targets to analyse. This requires reading different pulsar catalogues, analysing all the glitches we found during the O3 period to see how many of them present good characteristics for our study, and –mostly to anticipate results– doing some tests on expected indirect upper limits for all of the selected targets. At the end, as we show below, we end up with 6 targets of interest.

In parallel, we need to prepare a good set of Short Fourier Transforms for the Hanford, Livingston and Virgo detectors. [This process](#) consists in generating narrow-banded merged SFTs and then cleaning these SFTs.

After these preparation steps we can start the search: with some *python* scripts that will be explained in the [corresponding section](#), defining the ranges of transient parameters t_0 and τ , as well as the signal frequency model and its errors, we proceed by evaluating a template bank. The Gumbel distribution will be used to find a threshold as a reference to find significant candidates, after performing the search process, the one already stated in [chapter 3](#), which is based on the \mathcal{F} -statistic and \mathcal{B} -statistic.

Finally, for the targets that do not present a detection we use simulated signal injections to calculate [upper limits](#), to see the chances we actually have of detecting some signal from each target.

4.1 Target selection

4.1.1 Processing of catalogs

We start by reading one pulsar catalog, ATNF [76], and two glitch catalogs, ATNF [77] and Jodrell [78], but before trying to analyse them, we clean their structure. After downloading the raw tables from the web, we pre-process the data with *python* scripts to clean up columns and change their format, for consistency. We end up with two complete catalogues with summarized information for a high number of targets: general information of the pulsar and also particular values for the glitches. As a starting point, we perform a first cross-matching of the pulsars between the general catalogue and the two glitch catalogs, by name, to make sure all of them are included in both tables.

We identify each target by its PNAME and JNAME –in particular we always use the JNAME–. Some of the most recently discovered pulsars have only this J nomenclature, indicating 2000.0 coordinates, with a declination including minutes (for example PSR J1813-1749). All pulsars regardless of the moment when they were seen for the first time have a J name that provides more precise coordinates of its location in the sky.

Regarding the glitches information, we know the glitch number (in case the same pulsar suffered multiple glitches) and the date when each glitch took place in Modified Julian Days (MJD) format, with its error. The MJD format is the number of days since January 1st, 4713 B.C. at exactly midnight (00:00:00). By definition, MJD includes a time component expressed as a decimal, which represents some fraction of 24 hours.

We also know the relative change in frequency and first order spindown (in Hz), again with errors. These two quantities are the result of calculating the difference in frequency or spindown before and after the glitch and dividing by the original corresponding ones ($\frac{\delta f}{f}$ and $\frac{\delta \dot{f}}{\dot{f}}$, respectively). These catalogues also include some other variables which are not relevant here.

However, there are glitches from three targets that were not included in neither of these two public catalogs, even though the pulsars themselves are of course part of the ATNF pulsar catalog. Instead, we use directly the ephemerides provided by the NICER [79] and UTMOST [80] [81] [82] observatories. At the end we will work with ephemerides for all the targets, so the only difference resides on the fact that for some glitches we use them from the start, and for others we collect information from public catalogues for the initial target selection steps and then use complete ephemerides for the analysis. In particular, we have two targets from the NICER observatory, J0537-6910 (further discussed in [83] and [84]) and J1813-1749 [85], and one target from the UTMOST observatory, J1105-6107, discussed in [86].

4.1.2 Analysis of promising glitches

Now we perform the actual target selection: we go through a series of analyses to decide which targets are suitable for our study. First, we want to focus on pulsars that suffered a glitch during the O3 period (between April 2019 and March 2020). Secondly, from these glitches we just want to cover the ones that come from pulsars with a spin frequency over 5 Hz. That would lead to a gravitational wave frequency of 10 Hz, which we consider as the minimum detectable (see [aLIGO sensitivity curve](#)). In the following table, all the pulsars with glitches during the mentioned period have been included, along with their characteristics (relative frequency change, date when they glitched and EM frequency) and the data base from where they have been taken. Then we decide if they are apt for our purposes:

CATALOGUE	JNAME	dF/F	DATE (MJD)	$f(Hz)$	APT?
Jodrell	J0534+2200	$3.60 \cdot 10^{-8}$	58687.59	29.95	✓
Jodrell	J1737-3137	$1.53 \cdot 10^{-9}$	58858.80	2.22	✗
Jodrell	J1826-1334	$2.49 \cdot 10^{-6}$	58915.00	9.85	✓
Jodrell	J1838-0453	$7.10 \cdot 10^{-8}$	58692.00	2.63	✗
ATNF	J0908-4913	$2.17 \cdot 10^{-8}$	58765.06	9.37	✓
ATNF	J1257-1027	$3.20 \cdot 10^{-9}$	58649.30	1.62	✗
Others (NICER)	J0537-6910	$4.36 \cdot 10^{-7}$	58637.00	61.92	✓
Others (NICER)	J0537-6910	$1.22 \cdot 10^{-7}$	58807.00	61.92	✓
Others (NICER)	J0537-6910	$3.88 \cdot 10^{-7}$	58868.00	61.92	✓
Others (UTMOST)	J1105-6107	$1.17 \cdot 10^{-6}$	58582.24	15.83	✓
Others (NICER)	J1813-1749	$1.34 \cdot 10^{-7}$	58698.00	22.37	✓

From the table one can easily differentiate between the targets of interest and the ones that will not be taken into account, just by looking at the $f(Hz)$ column. Moreover, the relative frequency change (dF/F) gives us an idea of the glitch intensity.

At the end, 2 of the 5 glitches from the Jodrell catalogue that occurred during the O3 period will be included in this study: J0534+2200 –the famous Crab pulsar–, with a relatively high frequency, and J1826-1334, which presents lower frequency but a considerably greater relative frequency change. From the ATNF glitch catalogue, only two glitches took place during the time of interest, and one of them, J0908-4913, had a high enough frequency to be considered for this work. The “extra” glitches, the mentioned J0537-6910, J1105-6107 and J1813-1749 presented all great characteristics for the study. The case of J0537-6910 is of special interest, not only because it presents a huge glitch activity (it suffered three glitches during the O3 period) [87] [84], but we also have found another glitch which happened a couple of days before the start of O3 and will be taken into account as

well. This will be important since it will make us stake out some of the process we will explain in the present chapter.

Figure 4.1 shows visually the process we have just explained. The intensity of every glitch as well as the moment when they happened can be appreciated.

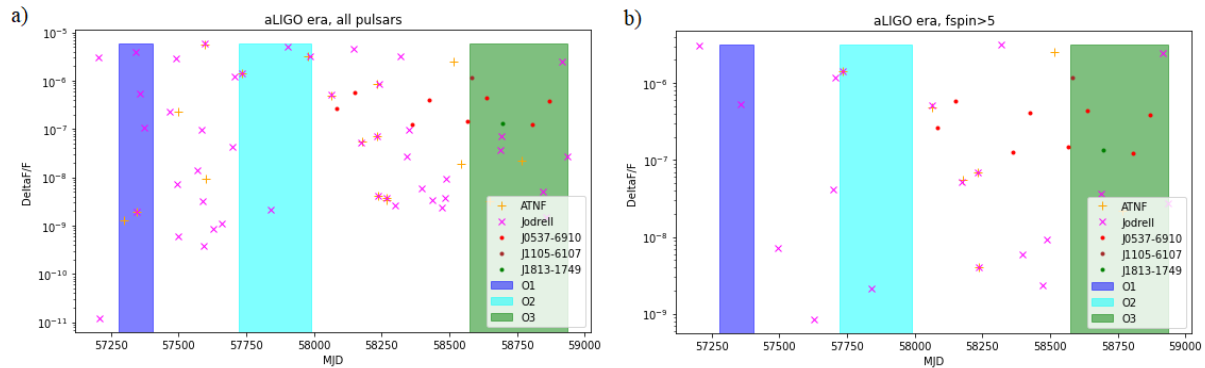


Figure 4.1: Relative spindown frequency against time for all the glitches detected during the aLIGO era.

We can observe, going from *a)* to *b)*, how some targets have been eliminated and will not be taken into account because of low spin frequency. As we have shown, there are 8 glitches from 6 different pulsars that seem suitable for our purposes: 1 unique glitch from J1813-1749, J1105-6107, J0534+2200, J0908-4913 and J1826-1334, and 3 glitches –but in the end, they will be 4, including the one that took place some days before O3– from pulsar J0537-6910.

4.1.3 Glitches reanalysis

The process just stated was done at the very beginning of this work, so, being aware of the constant updates of the catalogues, we decide to revisit all this process more than half a year later, to see if some pulsars suffered interesting glitches. The Jodrell catalog is the only one that present relevant changes, all listed in the following table:

JNAME	dF/F	DATE (MJD)	$f(\text{Hz})$	APT?
J0534+2200	$3.17 \cdot 10^{-8}$	58687.57	29.95	✓
J1737-3137	$1.53 \cdot 10^{-9}$	58858.80	2.22	✗
J1801-2304	$5.00 \cdot 10^{-9}$	58846.00	2.40	✗
J1826-1334	$2.49 \cdot 10^{-6}$	58915.00	9.85	✓
J1838-0453	$7.10 \cdot 10^{-8}$	58692.00	2.63	✗
J0726-2612 (N)	$5.10 \cdot 10^{-7}$	58791.00	0.29	✗
J1821-1419 (N)	$2.22 \cdot 10^{-7}$	58860.00	0.60	✗
J1841-0524 (N)	$5.53 \cdot 10^{-7}$	58724.00	2.24	✗
J1845-0316 (N)	$8.19 \cdot 10^{-7}$	58617.00	4.82	✗
J1847-0130 (N)	$5.67 \cdot 10^{-7}$	58857.79	0.15	✗
J2021+3651 (N)	$1.19 \cdot 10^{-6}$	58668.00	9.64	✓

From the 6 new O3 glitches in the catalog –marked with (N) after the name– only 1 came from a pulsar with sufficiently high spin frequency: J2021+3651, with a frequency of 9.64 Hz. If we redo the same plot as before, we obtain:

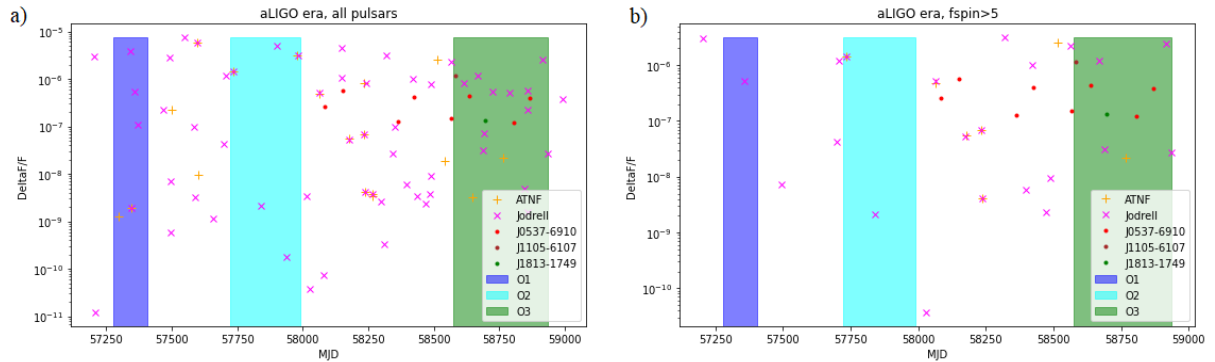


Figure 4.2: Relative spindown frequency against time for all the glitches detected during the aLIGO era, updated version

As mentioned beforehand, the only change with respect to the first analysis in the *b)* plot –the definitive one–, is the inclusion of J2021+3651 as a new candidate, even though several new glitches appear in *a)*. Jodrell provided an ephemeris for this target, but the timing uncertainty of the glitch is greater than 100 days, so our conclusion is to not consider this target for analysis anymore.

Even so, one can appreciate another glitch from the Jodrell catalogue just before the period of interest (marked with a pink cross). This pulsar is J1801-2451, with a rotation frequency of 8 Hz and a huge relative frequency change: $8.19 \cdot 10^{-7}$. As well as we do with the J0537-6910 glitch that happened in a similar moment, we first consider analysing it, but at the end we will, again, discard this glitch, for reasons explained in the [following section](#).

In conclusion, for this initial part of selecting the targets, we will study 1 glitch from J1813-1749, J1105-6107, J0534+2200, J0908-4913, J1826-1334 and 4 glitches from pulsar J0537-6910. At the end of the next subsection a [table](#) with all these glitches is included.

A recent Arecibo PALFA paper, [88], reported the discovery of 5 glitching pulsars not yet included in the ATNF catalog, with some glitches during O3, but they are all at far too low frequencies ($\mathcal{O}(1\text{-}2\text{Hz})$) to be of interest for this search.

4.1.4 Indirect upper limits

Upper limits calculation is the most common way to proceed when no significant candidates are found in this kind of searches. But before running the search and actually knowing if we should calculate upper limits, we can simply compare all the energy lost during each glitch, or indirect energy upper limits, with the sensitivity in our detectors.

We can compute easily this last variable, S_n –dependent on frequency–, using `lalapps_ComputePSD` from the “LALSuite” package, averaging over the full run. In order to know how likely we are to detect signals from the targets we have selected, we can analyse and compare the different indirect energy upper limits for each target with the sensitivity of our detectors. With upper limits above the sensitivity curve at the corresponding frequency we could be optimistic and think that the signal emitted by that particular pulsar could be detected. If not, then we know that even if all the energy released by some glitch went to the emitted gravitational waves we would not be sensitive enough to detect them.

Later on, direct upper limits are fully calculated, after running the searches and seeing that we have not found any interesting candidates –see [section 4.4](#)–.

The indirect upper limits on the total GW energy is equivalent to a maximum strain dependent on τ , which can be computed following [67]:

$$h_0 \leq \frac{1}{d} \sqrt{\frac{5G \mathcal{I} |\dot{f}|}{2c^3 \tau f}} \quad (4.1)$$

As just mentioned, we have already explained the sensitivity of our detectors, but the two curves in [figure 1.4](#) do not take the sensitivity depth into account. This is in fact the most natural way to characterize the sensitivity of a search [89]:

$$\mathcal{D} = \frac{\sqrt{S_n}}{h_0} \quad (4.2)$$

This parameter \mathcal{D} tells us how deep below the detector noise curve we can expect to detect signals, and depends on each pulsar, the setup of the template bank, and the average duty

factor of the detectors (the fraction of time that they are taking data). \mathcal{D} is proportional to the square root of the duration of the signal, $\sqrt{\tau}$ and varies with the frequency.

Although a per-target \mathcal{D} will be used for the final upper limits calculation, now we are interested in a preliminary target evaluation for which we can use simply a single depth value for all the targets, so we consider the mean of the different depth values for a set of targets and a given τ –we have used 10 days–. Then we modify the original sensitivity curve dividing by this number, following the equation above. The mean of the depths \mathcal{D} with $\tau = 10$ days is $31.2646 \text{ Hz}^{-1/2}$. To calculate this number we have used a particular *python* wrapper that calls the `Octapps` library [90]. All this general process is the standard way to calculate sensitivity estimations in \mathcal{F} -statistic searches, following [89].

The following commandline is used to calculate the mentioned duty factors for pulsar J1813-1749:

```
scripts/detchar/get_dutyfactors.py --target J1813-1749 --Tobs-days 1,2,5,
10,20,40,80,120
```

With the variable `Tobs-days` being the different values of τ we are interested in. These values will be different for the final upper limits procedure, but in the example below we have used only $\tau = 10$. After that, we generate a file with the depth values, depending on the mismatch we allow (`mm`) –defined previously in equation 3.12–, the false dismissal (`pFD`) –1 minus the upper limits confidence level– and a preliminary threshold `twoFthr` (this parameter will be correctly calculated and applied during the actual search, but for now we just need an approximate value):

```
/estimates/sensitivity_estimation_wrapper.py --target J1813-1749 --Nglitch
1 --mm 0.2 --pFD 0.05 --twoFthr 48
```

The output file is a table like this one:

T_{obs} (s)	N_{det}	df (Hz)	mismatch	pFD	2Fthr (Hz)	\mathcal{D} ($\text{Hz}^{-1/2}$)
86400	2	0.750	0.2	0.1	48	10.389
172800	2	0.635	0.2	0.1	48	13.524
432000	2	0.663	0.2	0.1	48	21.841
864000	2	0.712	0.2	0.1	48	32.021
1728000	2	0.682	0.2	0.1	48	44.298
3456000	2	0.700	0.2	0.1	48	63.503
6912000	2	0.524	0.2	0.1	48	77.680
10368000	2	0.518	0.2	0.1	48	94.574

Here we only take two detectors into account ($N_{\text{det}} = 2$) because the Virgo one, with slightly lower sensitivity, does not affect relevantly the depth factors. Also, we have chosen a preliminary threshold for all the targets ($2F_{\text{thr}} = 48 \text{ Hz}$) which will be properly

calculated when performing the full search. Finally, the false dismissal factor has been set to 0.1 even though at the end it has been changed to a more rigorous 0.05.

In figure 4.3 all of the targets are below the sensitivity limit at their corresponding frequency. Even so, it is interesting to take a look at the ratio between their UL and the sensitivity of the detectors at their frequency, and on the way, summarizing the targets that we have considered during this section for our study.

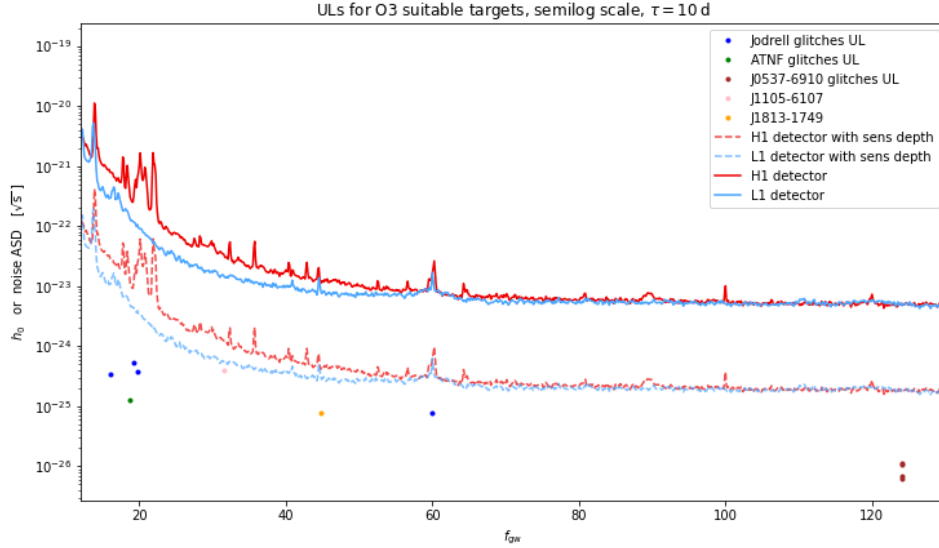


Figure 4.3: Upper limits and sensitivity curve, for searches of duration $\tau = 10$ days

Here the uncertainty of all the glitch times has also been included, because it will be relevant afterwards:

JNAME	Date (MJD)	$f_{GW}(Hz)$	dF/F	UL/Sens
J0534+2200 (J)	58687.500 ± 0.003	59.89	$3.6 \cdot 10^{-8}$	0.1837
J1801-2451* (J)	$58564.76 \pm ?$	16.01	$2.25 \cdot 10^{-6}$	0.0303
J1826-1334 (J)	58915 ± 21	19.71	$2.49 \cdot 10^{-6}$	0.0926
J2021+3651* (J)	58668 ± 114	19.28	$1.19 \cdot 10^{-6}$	0.1166
J0908-4913 (A)	58765 ± 4	18.73	$2.17 \cdot 10^{-8}$	0.0252
J0537-6910 (N)	58566 ± 5	124.05	$1.49 \cdot 10^{-7}$	0.0333
J0537-6910 (N)	58637 ± 8	124.05	$4.36 \cdot 10^{-7}$	0.0570
J0537-6910 (N)	58807 ± 3	124.05	$1.22 \cdot 10^{-7}$	0.0302
J0537-6910 (N)	58868 ± 5	124.05	$3.88 \cdot 10^{-7}$	0.0538
J1105-6107 (U)	58582 ± 2	31.64	$1.17 \cdot 10^{-6}$	0.7279
J1813-1749 (N)	58698 ± 1	44.74	$1.34 \cdot 10^{-7}$	0.1453

The ratio between the upper limits and the sensitivity curve is below 0.2 for all the targets except for J1105-6107, which is quite high. This means that in general we do not expect

to detect any signal for these targets we have, but this process will be redone with the final search setup in [section 4.4](#).

Note that the table includes the two new targets found during the glitches reanalyses ([section 4.3.1](#)) which are finally not taken into account. J1801-2451 happened before the start of the period of interest, so we would only search for signals of this pulsar if it presented promising characteristics, but instead it has one of the lowest UL/sens ratios. The case of J2021+3651 has already been discussed: we discard this pulsar because the uncertainty on the glitch time is 114 days, nearly the maximum signal time τ that we are considering in the process.

4.2 Data selection

Before we dig into the data manipulation steps, we generate a plot for the availability of the detectors during the O3 period:

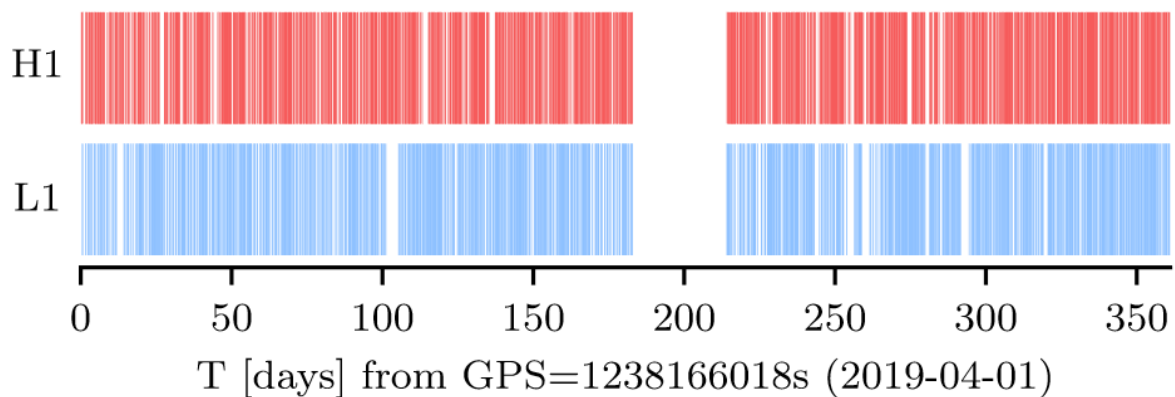


Figure 4.4: Full O3 run availability of Hanford and Livingston detectors. The blank period between days 180 and 210 approximately is due to a maintenance break

Afterwards, for each candidate we will generate a single particular plot like this one in order to see if the detectors –including Virgo for most of the targets– have been collecting data during the days of interest for that particular target.

We use “gated” data to remove loud transient artifacts [\[91\]](#) [\[92\]](#) and the 1800s Tukey-windowed Short Fourier Transforms (SFTs) for all three detectors.

To have a consistent set of SFTs for all 3 detectors, they were regenerated from the original gated frame files for the narrow band CW \mathcal{F} -statistic search that forms part of [\[62\]](#), but using the “lalapps_Makefakedata.v5” executable instead of the tool usually used for this task, “lalapps_MakeSFTs” [\[71\]](#). The reason is that the latter had trouble processing Virgo frames.

We have initially a set of SFTs consisting of a single file per timestamp over the full

frequency band. For our purposes we are interested in minimizing the computational costs when reading these files, so we generate a set of narrow-banded merged SFTs with one file per detector from per-timestamps inputs for each target. We use a script to which we give the path to the original SFTs, the length of each of these SFTs in seconds –as mentioned, 1800 by default–, and of course the target and IFO we are working on.

The frequency range will be automatically decided based on the specified target and a “band” option. This is the frequency band width, to be centred on expected gravitational wave frequency of the pulsar f_{GW} at time $t_0 = T_{gl} - T_{glerr}$, using an approximation to the standard search setup and a simplified pulsar spin evolution for the central frequency. The default band is 1 Hz, which is big enough for all the frequency bands for the searches of order 10^{-2} Hz.

Once this is done, the SFTs are cleaned from known instrumental lines. Those lines we want to erase are provided by [93] for LIGO and by [94] for Virgo. For the LIGO lines, we use initially version 1.5 of the published lists for all targets. Since a new version 1.6 was released later (and even a newer one, 1.7, in September, 2021), we repeat the cleaning procedure to find out if we could see an improvement with the updated version on all the targets. At the end we could only find relevant differences changing from version 1.5 to version 1.6 with pulsar J1813-1749 (it had one additional line for each detector) so we only reprocessed this step for this target. This will be further discussed in [section 4.5.1](#).

The procedure of SFT cleaning is done by executing the “lalapps_SFT_clean” command, which removes the bins –at resolution $1/T_{SFT}$ – corresponding to known instrumental lines from the SFTs, and replaces them with gaussian noise, where the ASD corresponds to the median of the surrounding bins. We use a script to which we give the path to the original SFTs, generated in a previous step (one file per detector), and, after translating the lines file format to the old format that “lalapps” can read with a parsing module previously used in [23], it then removes the undesired lines.

The process is visually very intuitive. We have initial ASDs for both Hanford and Livingston detectors, which can present very huge jumps –high vertical line in the plots–. In the case of PSR J0908-4913, as can be appreciated in [figure 4.5](#), there are lines to clean only in the Hanford interferometer (top left plot), while in the Livingston one there is nothing to do: as a consequence, top right and bottom right plots are identical. After the process, all the lines from the first detector, which are marked with orange vertical bars, have disappeared, and in the bottom left plot we can see a much more smooth curve.

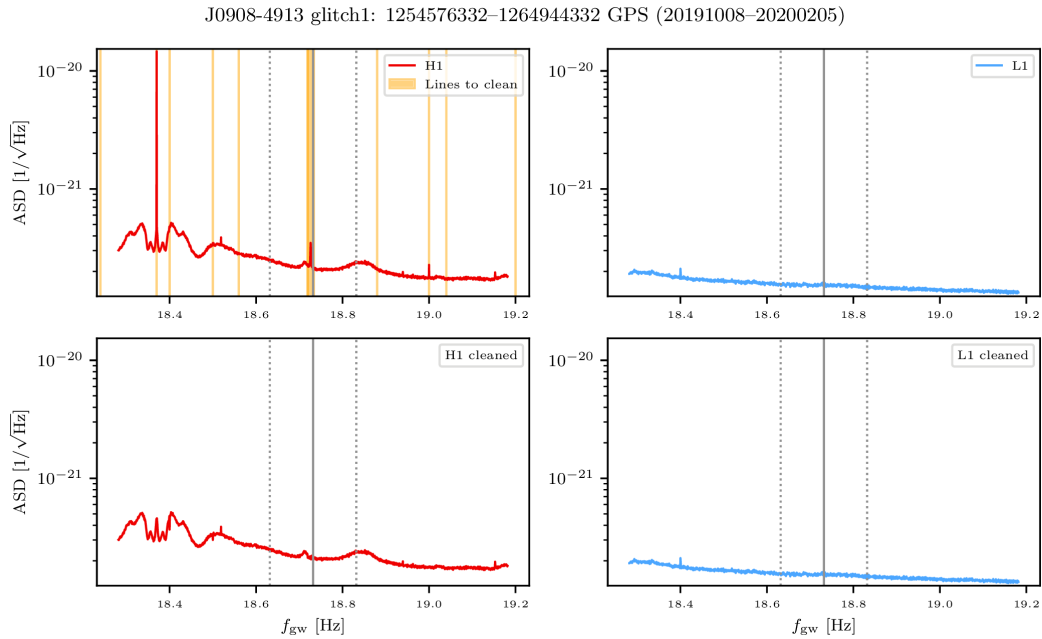


Figure 4.5: ASD plots for J0908-4913 before and after the cleaning lines procedure

To see it more clearly one can plot the difference between the ASD set before and after the cleaning process, [figure 4.6](#). While the Livingston difference curve is set to 0 for the whole range of frequencies, the Hanford curve has an enormous peak right before 18.4 Hz and some extra –minor– peaks at different places along the frequency domain.

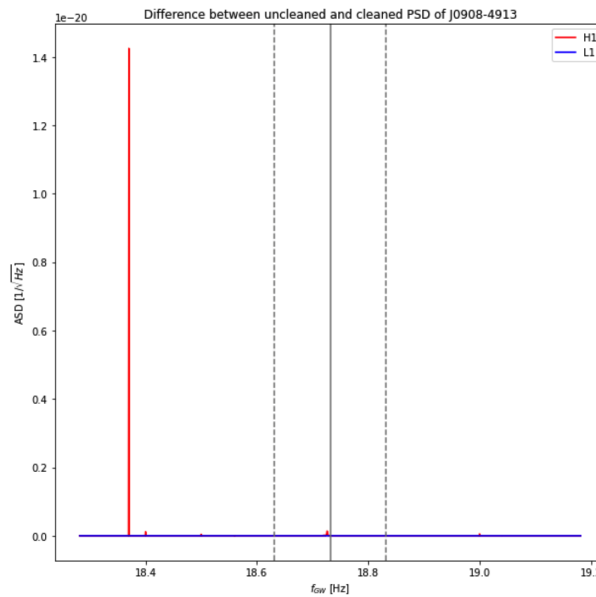


Figure 4.6: Difference between PSDs before and after the cleaning lines procedure for both detectors

4.3 Search setup

After selecting our targets, we collect relevant information of each of them and create a file to store it. The general parameters we have for any target are name, ephemeris, distance, LIGO computing cluster where the SFTs are stored, path to SFTs and path to cleaned SFTs. Each target will also have entries with information about their glitches, mainly when they occurred and the glitch intensity.

We create a “single source of truth” *.ini* file with the information about all targets that we need, and all the scripts to process the setup procedure read the targets information from this file. An example would be:

J0537+2200	
ephem	J0534+2200_no_fitwaves_fewer_spindowns.par
dist	2000
cluster	ldas-grid.ligo.caltech.edu
sfts	.../J0534+2200/sfts_narrowband
sfts-cleaned	.../J0534+2200/sfts_narrowband_cleaned
J0537+2200_glitch1	
MJD	58687.644
MJDerr	0.003
dFbyF	$1.2 \cdot 10^{-8}$
dFbyFerr	$1 \cdot 10^{-9}$
ref	http://www.astronomerstelegam.org/?read=12957

Now, the main search procedure, stated in [chapter 3](#), is based on the execution of a script that extracts parameters of a particular target and glitch from the mentioned file and the corresponding SFT files and pulsar ephemeris to create condor submit files (explained in [section 4.3.5](#)) for post-glitch searches.

One example of a commandline for running this script is:

```
python make_search_jobs.py --outdir /scratch/joan.moragues/
J1813-1749_rerun_oct --scriptpath /home/joan.moragues/o3glitches/scripts/
search/ --target J1813-1749 --gridType 8 --IF0s H1,L1,V1 --lalpath
/home/david.keitel/cw/03/lalsuite-strictSpindownBounds/bin/ --jobs 50
--dtau 3600 --dt0 3600 --plotSpindowns --metricMismatch 0.2
```

Besides the trivial parameters, such as target, glitch (only needed in cases of pulsars with multiple glitches), user etc. the other parameters we use in this process are the following ones. First, the detectors with which we want to perform the search (at least one of the three H1,L1,V1). The “jobs” option is also relevant, but will be discussed in [section 4.3.5](#). Then there is the “gridType” option, which can be set to 0 or 8. If it is

set to zero, we manually have to choose the steps in frequency and spindowns, and the generated template bank is a hypercubic grid –with dimensions depending on the number of spindowns we have– uniformly distributed along each dimension. But in general we fix this variable to 8. This means that the steps on frequency and spindowns are calculated with a template placement algorithm [95] which minimizes the mismatch introduced in section 3.1.2 –chosen as 0.2 in this search–. As shown in figure 4.7, the algorithm takes into account the ellipses corresponding to this mismatch surrounding each template in order to fill all the area of the parameter space.

One option when performing this part of the search worth to mention is `StrictSpindown-Bounds`. If we ask the script to create a grid with this option it will use only the solid-drawn templates instead of also including the white ellipsis at the edges of the bank. The reason why we sometimes use this option is to reduce the computational cost, especially for those targets with \dot{f} and higher spindown terms, to avoid placing too many points outside the intended range.

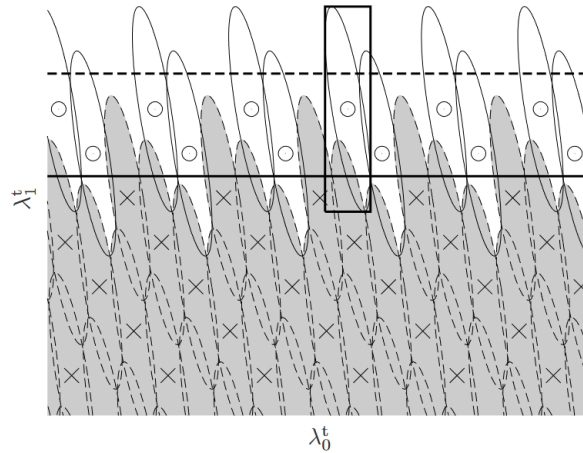


Figure 4.7: 2D parameter space with templates. Extra templates lying outside the parameter space are required in order to cover all the area. Credit: [95]

For the frequency and spindown bands we want to choose essentially the maximum between $f^{(k)}$ uncertainty and what we call the glitch step, if they are greater than a thousandth part of $f^{(k)}$ (if not, then the band should be precisely that, $f^{(k)}/1000$). $f^{(k)}$ is twice the spin frequency or derivatives at order k extrapolated from the ephemeris epoch to the search reference time, so the $f^{(k)}$ uncertainty is the error on $f^{(k)}$, including the propagation of the glitch uncertainties. The glitch step is the difference between $f^{(k)}$ before and after the glitch, including the uncertainties.

Finally we can also ask for a specific number of jobs if necessary, due to computer cost, or leave the default 1 job per file. The frequency band will be split up if we ask for more than 1 job to loop over those sub-bands, and each job will loop also internally over the full $f^{(k)}$ and transient parameter ranges.

4.3.1 Signal start times: t_0

Our general rule is to search over a range of different start times in the interval: $[T_{\text{gl}} - \max(T_{\text{gl, err}}, 1 \text{ day}), T_{\text{gl}} + \max(T_{\text{gl, err}}, 1 \text{ day})]$, so to account for the uncertainty on the time of the glitch. Both T_{gl} and $T_{\text{gl, err}}$ come from the *.ini* file and not from the ephemerides –this is because in some cases, the EM observers gave us directly bigger uncertainties for a particular target than the initially included in the ephemerides files–. However, depending on the available SFTs, there can be exceptions to this rule.

For instance, in the case of glitch 5 of J0537-6910, as can be seen in [figure 4.8](#) the interval of start times does not overlap with the available SFTs as the glitch happened before the start of the O3 run.

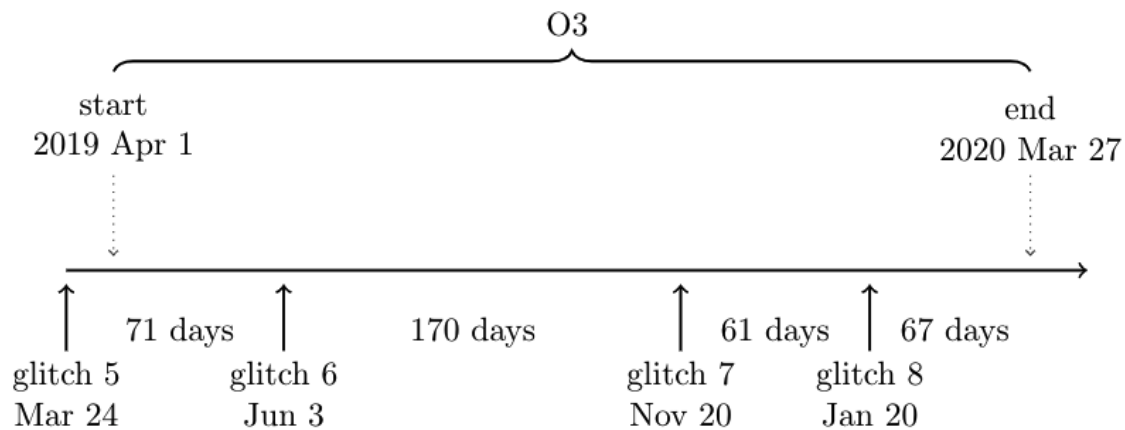


Figure 4.8: Timeline plot for J0537-6910. Credit: [\[62\]](#)

When this occurs, since we do not have data in the t_0 interval, we shift the start time to the first available SFT timestamp and set the interval band to 0: according to our choice above, the t_0 band should be centered on the T_{gl} , so now that this condition is not satisfied anymore, we are not interested in searching around the initial time t_0 . This means that we will miss the early part of any signal starting at the glitch, but could still have a chance to see its later part.

4.3.2 Signal duration: τ

We decide to search for transients with duration in the interval $[3600 \text{ s}, 120 \text{ days}]$. The minimum is given by $2T_{\text{SFT}}$, and our code can not cover any shorter duration; and the maximum is set by computational cost reasons, but also because typically it takes not more than a few months for pulsars to recover after a glitch [\[51\]](#) [\[96\]](#).

However, as before, there can be exceptions. Again, taking as example the fifth glitch of J0537-6910, as can be seen in the plot above, there are only 71 days between glitch 5 and

glitch 6, so the maximum value of the duration of the search is limited; and the same happens for glitch 7, with only 61 days between this glitch and the next one. Finally, for glitch 8 we can see that O3 stops before the 120 days from the glitch, so even if the reason of the cut of the duration is for the unavailability of data, we treat this glitch's τ parameter similarly to glitch 5 and 7.

In these cases we simply cut the duration interval above to either $[3600s, \text{last_SFT}]$ or $[3600s, T_{\text{next_glitch}}]$.

4.3.3 Frequency and spindown bands

At the beginning of the present section we have already stated how we choose our frequency and spindown bands, but we can use an example plot to see it more clearly:

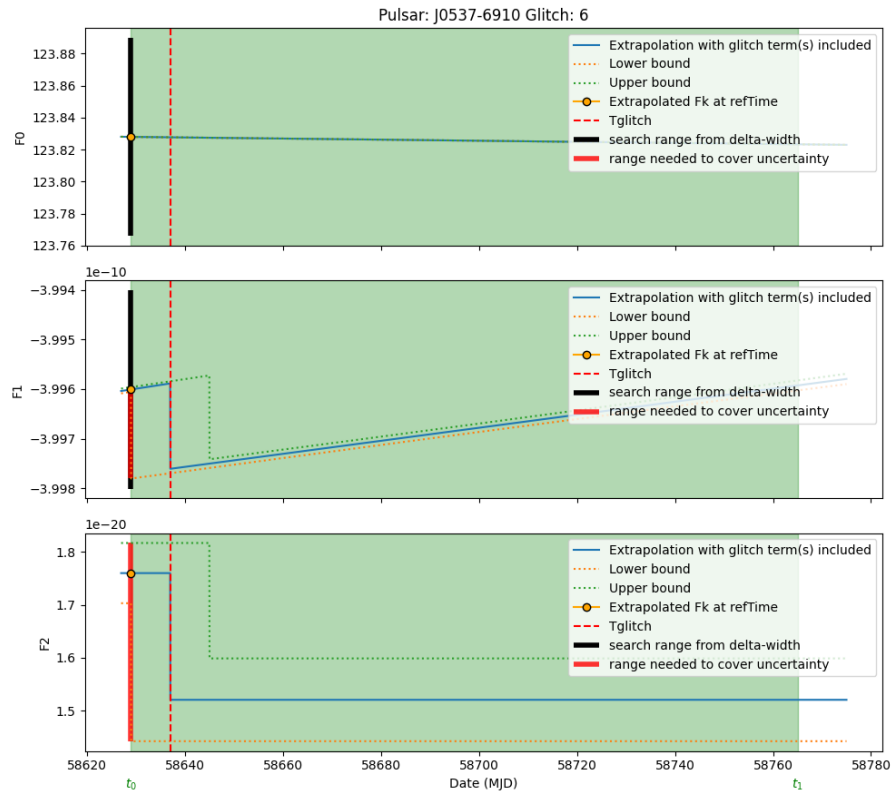


Figure 4.9: Evolution of frequencies at different orders together with the candidate search ranges of J0537-6910 sixth glitch

Focusing on the second subplot, the blue line is the evolution of the spindown –first derivative of the frequency–, and the green and orange dotted lines outline the upper and lower uncertainties on that spindown. The black thick vertical line is the thousandth part of the $f^{(k)}$ range, and the red thick vertical line is the glitch step.

As an example we can go through the three orders of frequency shown in this plot and determine which bands we choose as search ranges:

- F_0 band (1st subplot): We have to choose $f^{(k)}/1000$, which is the black range, because the other ranges are so small, they are not even visible in the plot.
- F_1 band (2nd subplot): Again we choose $f^{(k)}/1000$. Here the red range (glitch step) is visible, but the black one is bigger
- F_2 band (3rd subplot): Now we choose glitch step. In this case the red range is the biggest one.

Regarding the calculation of the error propagation, we perform the standard Gaussian propagation on all the frequency and spindown terms inside the spindown expression:

$$f(t) = f_0 + \dot{f}_0(t - \text{PEPOCH}) + \frac{\ddot{f}_0}{2}(t - \text{PEPOCH})^2 + \dots \\ + \Theta(t - T_{gl}) \left[\text{GLF0} + \text{GLF1}(t - T_{gl}) + \frac{\text{GLF2}}{2}(t - T_{gl})^2 + \text{F0D} \exp\left(\frac{t - T_{gl}}{\text{TD}}\right) \right] \quad (4.3)$$

One can understand more easily these terms by looking at [figure 2.3](#). The GLF k terms stand for the glitch steps at order k (GLF0 is the total change in frequency, so the same as $\Delta\nu(t_g)$ in the mentioned figure); PEPOCH is the time when the period of the pulsar was determined, F0D is the equivalent of $\Delta\nu_t$, the transient part, and TD is the time that this transient part lasts. The permanent part stands for the difference between the original frequency and the “stable” frequency after the glitch.

As for the glitch terms, the ones multiplied by the Heaviside function, we also have to consider the errors on T_{gl} , GLF0, GLF1, etc. But since T_{gl} is inside the Heaviside function, we cannot propagate in the proper standard Gaussian way. They are instead added to the main extrapolation curve at the nominal T_{gl} and to the envelopes at $T_{gl} \pm T_{gl, \text{err}}$ depending on their sign –we account for earliest and latest expected occurrence in a conservative way–.

With this management of the glitch term we are taking into account the uncertainties on the T_{gl} parameter and therefore making sure that we are searching for transients in the most conservative interval.

J0537-6910 glitch 5 is a special case, because the glitch occurred before the first available SFT and therefore our reference time. Another example is the case of J0908-4913, because its glitch step is before the start of the period where we have data. In these cases we can not consider the red range as the whole glitch step as we do in the other cases (for example, one can see it clearly in the F1 spindown [plot above](#)), but rather just the uncertainty on the spindowns.

4.3.4 Evaluation of template bank and runtime estimation

All our setups use the option “gridType = 8” which corresponds to the metric from [70] and a template placement algorithm from [95]. The search main script, already explained, has 2 optional parameters to generate the template bank as a separate file more quickly (`--countTemplates` and `--outputGrid`), before running the more expensive actual search.

Then we can visualize it with another script, which plots a “corner” of the template bank (plotting it whole would take too long and be unnecessary). This process consists basically of reading the “grid file” generated with the main script, and we ask it how many rows we want to read from the template bank, and which spindowns we want to focus on, and plot on the horizontal and vertical axes. Depending on how many spindowns we search over, these options can be (F0,F1), (F1,F2), (F2,F3), always with order k in the x axis and $k+1$ in the y axis. It plots a red box which encompasses the spindown bands that we search over, blue points all along the domain (the templates) and green crosses corresponding to F1 values at a few fixed F0 points, as one can appreciate in the following figure.

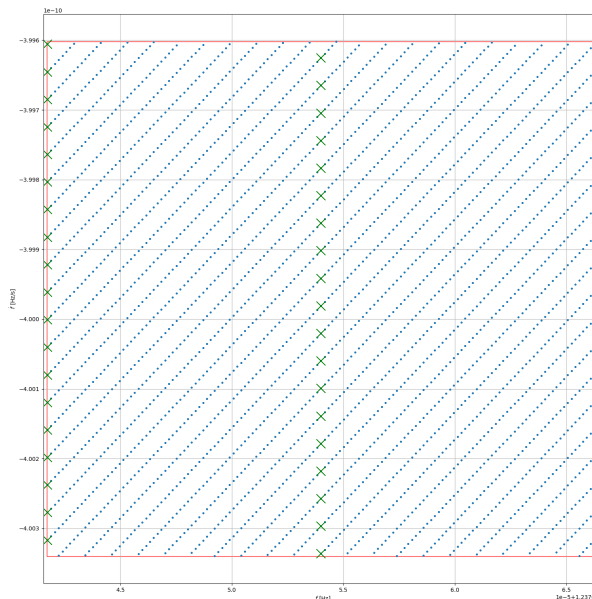


Figure 4.10: Example of generated grid with “gridType = 8”

Then, knowing the total number of templates as well as the width of the bands for the transient parameters t_0 and τ , we can make a rough estimate of the runtime in hours of the search:

$$\frac{t_{0_Band}}{\delta t_0} \cdot \frac{\tau_{Band}}{\delta \tau} \cdot N_{temp} \cdot A \quad (4.4)$$

With N_{temp} the number of templates (this is, the product of the number of templates for

every frequency order) and A the atomic cost. Since we do not know this last variable, what we do in practice is running a narrow subband and get the cost of this subrun. Then multiplying that by the total bank size to get the actual estimated cost of the full search.

4.3.5 Running jobs via condor

Even though the transient-CW narrow-band search can be relatively cheap, we reach sometimes millions of templates per target, which significantly increases the time it takes for a computer to run the search.

In order to run highly expensive searches, we are interested in tools that allow us to minimize the run time as much as possible. LIGO provides clusters for any of its projects with thousands of cores. There, any LIGO worker can run several jobs in parallel, allowing them to run processes of high computational costs reducing significantly the run time, meaning the time that we have to wait to obtain the results. In particular for this project we have used HTCondor [97], which is a scheduling system –meaning that the submitted jobs are sent to the cluster in order of submission– to manage those jobs. At the end we performed very cheap setups, of less than a thousand core hours each; even though during the development of this project, for preliminary setups with lower mismatches, some of them could have reached tens of thousands of core hours. Moreover, without the `StrictSpindownBounds` option, that cost would have been multiplied by a factor of ten or more. The final run times for the different targets will be mentioned in a summary table at the end of the present chapter.

But managing Condor has also its difficulty. We want to avoid submitting a single, very long job; so for each target, depending on the estimated run time, we could split the search into different `.sub` condor files, each one searching over a small piece of the frequency band.

In fact, what we do is not quite this, but we follow another strategy: implement a feature in the main script for which each condor file can contain more than one process, or jobs. This can be done using the condor “Queue” setting. We want every individual job to take between 1 and 2 hours maximum (they could be much longer, but due to the clusters instability sometimes, short jobs allows us to be less worried in case they fail). For that purpose we have to first calculate the estimated run time, and divide this number by the time we want each job to last. For example, with 20 hours of estimated run time, if we want jobs of only 2 hours, we need to run 10 jobs.

Before running the full search it is often convenient to perform a test with a single-job version file. Submitting this file and testing if the job takes approximately 2 hours to finish we can make sure that the total search will take the expected time to finish. If it does, we run the rest of the jobs and the search is done.

4.3.6 Determining a threshold for detection candidates

Once the search has been performed we need a way to fix a threshold on the detection statistic over all the evaluated templates. This means that we want to estimate the distribution of a set containing the maximum values of the whole space in order to take into account only interesting outliers. Those are points above the expected loudest value from pure noise. Since we do not know this distribution analytically for any template banks, we estimate it from the distribution of the actual search results [98]. The basic idea is to fit the distribution of the highest values from subsets (“batches”) of the search results with the Gumbel distribution and then propagate this fit to the total template bank size, using for this purpose a new method based on extreme value theory [99].

Named after Emil Julius Gumbel (1891–1966), based on his original papers describing it [100], the Gumbel distribution is a useful tool to model the distribution of the maximum of a number of samples of various distributions.

It is a particular case of the generalized extreme value distribution (also known as the Fisher-Tippett distribution [101]), and it corresponds to this equation:

$$\text{Gumbel}(x; \mu, \sigma) = \frac{1}{\sigma} \exp \left[-\frac{x - \mu}{\sigma} - \exp \left(-\frac{x - \mu}{\sigma} \right) \right] \quad (4.5)$$

With μ the location parameter and σ the scale (both real numbers, with $\sigma > 0$). The former gives us the maximum value of the distribution and the latter is directly related with its width (the standard deviation is $\frac{\pi\sigma}{\sqrt{6}}$).

The process is very simple: we split the N results into a number B of equal batches, take the maximum value of every batch and fit a Gumbel distribution to the histogram of these highest values. But this Gumbel fit corresponds to the distribution of the loudest candidate over n templates (being n the number of values per batch, N/B), and we want the distribution for the loudest candidate over the total N samples, which is the same as over B independent batches. The final distribution will be another Gumbel distribution with parameters:

$$\mu_* = \mu + \sigma \ln B, \quad \sigma_* = \sigma \quad (4.6)$$

One final consideration we have to do is to think of outliers from noise disturbances that do not belong to the estimated background distribution; in other words, higher values make the distribution appear shifted up (the threshold will be set at greater values and we could miss a signal). To avoid this we can optionally perform a notching procedure: we eliminate frequency bands that contain samples above a certain threshold. This process often underestimates thresholds, so it has to be used with care, and we end up not using it for the targets covered here, for which the distributions are sufficiently clean.

For targets with low number of samples N we can perform an extra test: off-sourcing [102].

This consists of doing several searches with random sky locations, different from the fixed locations of that particular target but with identical settings and on the same data, and doing then the histogram and fit of the highest values of each run. This is equivalent to performing the search with different data, what we expect is that the maximum value of each random sky location runs will be similar to a set of draws from different noise realisations. This way we can fit a Gumbel distribution to this histogram and expect to find a similar threshold than in the other procedure.

4.4 Upper limits

4.4.1 General Procedure

The indirect upper limits calculation has been introduced in [section 4.1.4](#), and allows us to compare the maximum strain of a gravitational wave from a certain pulsar with the sensitivity of the detectors. But while performing actual upper limits what we want to do is look for what maximum strain h_0 could have arrived at the detectors during our observation without us seeing a candidate instead. In other words, we want to know the lowest strain that we cannot exclude at a given % confidence, commonly 90% or even, as we will do in this project, 95%. In order to estimate that, we perform injections with given h_0 , τ and some other needed parameters and see what we obtain. Then we can compare these values with both the glitch excess energy and the estimated sensitivity of the detectors.

The general procedure mainly follows the steps of [\[75\]](#). We perform software injections of simulated signals into the same data sets as the ones used for the original searches. For a certain set of duration times (the usual τ parameter) which will typically span from half a day to 120 days, we perform several injections, with varying strain h_0 . In particular, we want to test different strains over the search ranges of the different frequency orders, signal start times t_0 and over the other amplitude parameters, both distributed uniformly and randomly.

We then perform the search in a small box in parameter space around these injected signals; for each τ we can compute the probability of detection P_{det} , which is the probability of the maximum values of the detection statistic from the injections is higher than the threshold already determined. The result is an efficiency curve of the probability of detection P_{det} against injected h_0 . The points at the different h_0 can be fit with a sigmoid function. This function takes the form

$$S_f = \frac{1}{1 + e^{-a(x-b)}} \quad (4.7)$$

with a and b parameters determined with the *python* “curve.fit” function included in

the “`scipy.optimize`” package. Then we solve the curve at $P_{\text{det}} = 95\%$. This $h_0^{95\%}$ is the estimate of the required scale of the strain at which 95% of the signals are recovered above the threshold on the detection statistic.

As a final plot we gather all the points of $h_0^{95\%}$ and plot them as a function of the duration τ . An example has been already included in section 3.2, [figure 3.6](#)

4.4.2 Setup

We split up the procedure above into 3 different python scripts with 1 additional script for the final plotting of the upper limits as a function of τ .

The first script’s purpose is to make a condor submission file, and as arguments, besides the typical, always necessary, ones (target and glitch, detector, paths...) it needs some other new important parameters.

To begin with, “freqband” is the frequency band (in Hz) to cover around each injection, in principle 0.0001 Hz; and “injtau” is the fixed duration τ we focus on for this particular set of injections. Also, we have to think of what strain interval we want to cover for each case. A first estimation (EST) of where this interval should be centered at can be computed as follows:

$$\text{EST} = \frac{h_{\text{mean}}}{\text{depth}} \quad (4.8)$$

Where h_{mean} is the harmonic mean of the median ASD values in each detector for the target frequency band, and the estimated depths are known values. This process is analogous to the [\[89\]](#) method, taking into account the detector duty cycles for each target, as mentioned in [section 4.1.4](#). The difference resides on the fact that now the depth values are explicitly calculated for each target, because it depends on the threshold obtained from the search results, previously stated.

Once we have our estimate for a particular target, we then can make a first guess of where the h_0 range interval of the injections should be centered. With that first approximate estimate, we can then specify “h0min”, the starting strain value h_0 for injection; “numh0s”, how many points in h_0 we want to cover; “h0step”, step between each h_0 point; and “numinj”, how many injections for each h_0 . We inject multiple times for better statistics, and the bigger this number, the smaller the counting error in the sigmoid plot.

So, in summary, for this first part of the process, we determine an interval of h_0 all along which we will calculate the sigmoid plot, by specifying the start point of that interval, how many points in h_0 we want to cover, and the step between each point.

With a script called “`make_ul.jobs.py`” we generate the condor `.sub` with the right parameters to loop over, in order to then execute the upper limits. This script performs both

the injection with “lalapps_Makefakedata_v5” and the search with “lalapps_ComputeFstatistic_v2”. Therefore, two parameter set-ups have to be made: one for the injection and one for the search.

Injection setup

As stated above, at a fixed h_0 amplitude value, we inject “numinj” signals, uniformly distributed in frequency and spindowns, and randomized over the amplitude parameters.

We will inject signals into uncleaned data, and then perform cleaning with the procedure used in [section 4.2](#). This ensures we are treating the software injections the same as if they had been present in the original data, and do not overestimate our detection probability by falsely counting injections in the cleaned bands as detectable.

Search setup

For consistency, we use the same setup as the original one. However, in order to speed things up, we decide to:

- Search over only a small frequency band (as stated above, 0.0001 Hz). The search frequency is not centered at the injected frequency, but rather we want to use the same grid of the template bank we used for the original search. But since we use the “-gridType=8” option of *CFSv2*, we cannot reproduce the grid ourselves manually, since the construction algorithm is internal to *CFSv2*, nor re-compute the grid with the “-gridType=8” option, because this would give a different grid.

The workaround we use here is to take the “gridfile” generated as we have explained in [section 4.3.4](#) and then cut out the region of interest.

- As for the higher spindowns, we fix these to a single value, i.e. we do not perform a narrow-band search on the higher spindowns for the upper limits. The fixed value will be the closest point at each frequency point.

A third script is in charge of reading the generated injection search results. We give manually the the column of “CFSv2” from which we want to read the results of the detection statistic (can be “maxTwoF”, “logBstat” ...). It also counts the injection whose detection statistic is above the threshold (which we can again provide manually) and computes the probability of detection together with its counting error for a fixed value of h_0 , then loops over the different h_0 s we have specified and repeat these steps, to finally obtain a sigmoid plot and fit data points with a sigmoid function. Once it has generated the plot it solves the sigmoid function at 0.95 to obtain the desired $h_0^{95\%}$ at that particular τ with error propagation.

After this steps we can run the same command for the different duration τ of every target and obtain the $h_0^{95\%}$ for each τ .

Finally, the last script simply plots the results of the $h_0^{95\%}$ at each tau, for each target, together with the astrophysical spindown limit associated to the glitch energy.

4.5 Results

The results of this particular project are part, as mentioned several times, of a bigger work, [62]. Specifically, some of the outcomes presented in this section will be main contributions to that paper.

First, our target selection procedure (in section 4.1) will be directly included in the main article. Regarding the search setup, some versions of the spindown extrapolation has also been performed here and included in the principal work, even though the final version of this part is done in collaboration with other analysts. Finally, full runs for 3 of the pulsars (J1813-1749, J1105-6107 and J0908-4913) have also been performed, but for time availability issues, only for one of them (J1813-1749, the version included here) it will be the definitive run.

For that reason, in this section we are going to go through the results of this particular target of interest. Then we are going to take a look at some particular special cases which need some different treatment, and finally we will summarize all the results in general.

4.5.1 J1813-1749 full results

This pulsar, with a frequency of rotation of 22.37 Hz (so an expected $f_{\text{GW}} = 44.74$ Hz) –data provided from the NICER telescope– suffered a glitch at date 58698.00 MJD, with a relative change in frequency of $1.34 \cdot 10^{-7}$. It is located at 4700 pc away from the Earth, at $\alpha = 4.7717$ rad and $\delta = -0.3112$ rad. We only know its first order spindown, which is $-1.2863 \cdot 10^{-10}$, and the absolute change on this spindown due to the glitch was $1.32 \cdot 10^{-13}$.

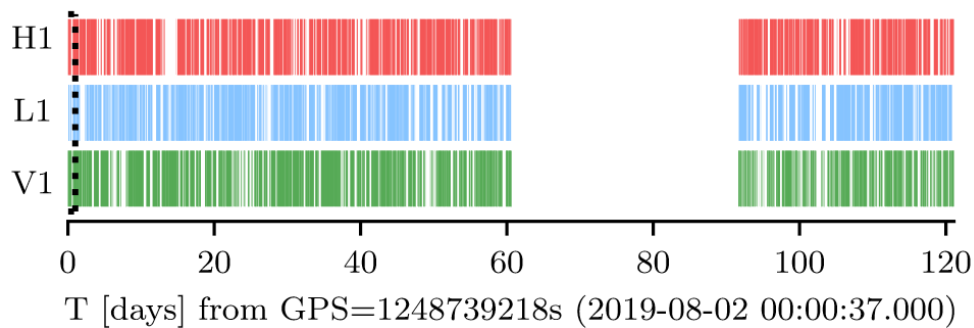


Figure 4.11: Availability of the three detectors for the times of interest for J1813-1749 (120 days after the glitch). One can see how the maintenance break took place during the period of interest of this target.

Following the process described before in this chapter, the steps of cleaning the SFTs on the ASD curves will be first shown, before going into the analysis of the frequency plots, and the main search, consisting of the generation of the frequency grid and the evaluation

of the detection statistics. Finally, given that no detection was achieved, we will take a look at the upper limits.

The generation of the ASD plots for this particular target is shown in [figure 4.12](#).

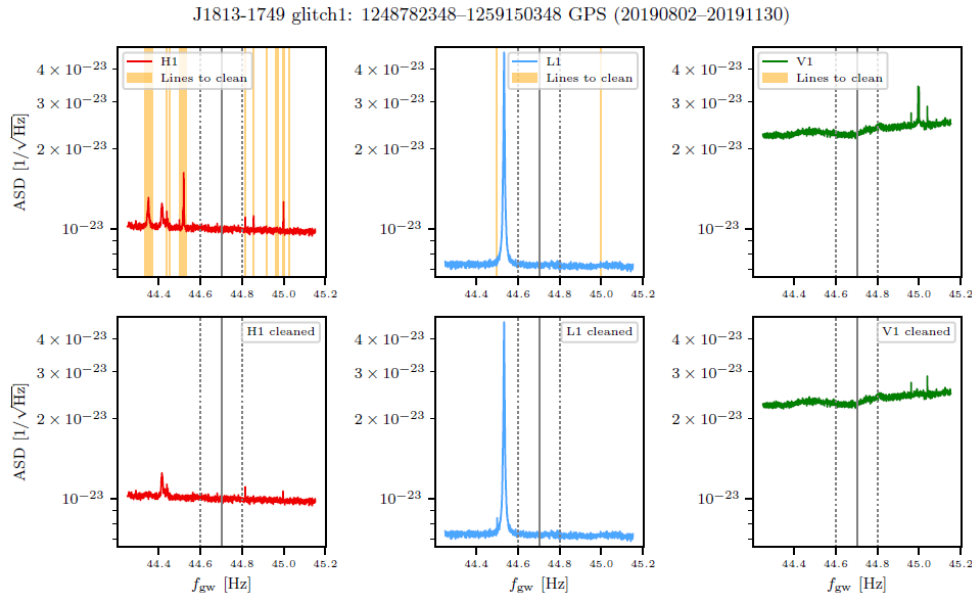


Figure 4.12: J1813-1749 ASD plots before and after cleaning for the 3 detectors

We can easily see a huge number of lines suppressed in the Hanford detector, while only two lines are included in the list of lines with known instrumental origin [93], and hence considered safe to be cleaned in the Livingston detector. Finally, the Virgo PSD does not need to be modified since no relevant lines have been detected.

Analysing this process we have found an issue, related to the different versions of the line files. As we have gone through in [section 4.2](#), different versions of the line files have been tested, choosing version 1.6 for (only) this particular target. As can be appreciated in the image, there is one line at slightly more than 44.8 Hz, marked to be cleaned, but looking at the plot after the procedure (in the bottom left), this line is still there. What happened is that the cleaning step was at the end performed with version 1.5, which did not contain this particular line to clean. Seeing that this is a line considerably far away from our frequency of interest, we decide to keep going with this set of SFTs.

Once we have cleaned the SFTs we can keep going into the frequency/spindown evolution plots. For J1813-1749 we have only one order of spindown included in the ephemeris, so we can generate two plots.

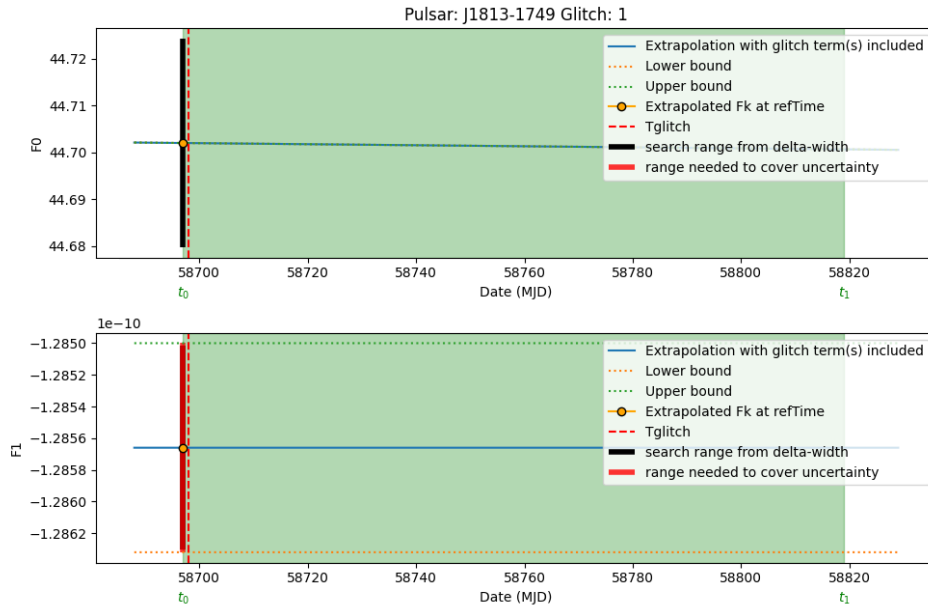


Figure 4.13: J1813-1749 spindown plots (frequency derivatives at order 0 and 1)

The frequency plot (first subplot) shows a slowly decreasing frequency over time –even though it seems constant at first glance–. The black band is bigger than the red one for the uncertainty from ephemeris errors, which mean we will take $f^{(k)}/1000$ as a search band. On the other hand, in the second subplot the red band is greater so for the first order spindown we will use the propagated uncertainty for the total width of the band. Also, the glitch step can not be seen due to the scale: the search band is much bigger than the glitch step.

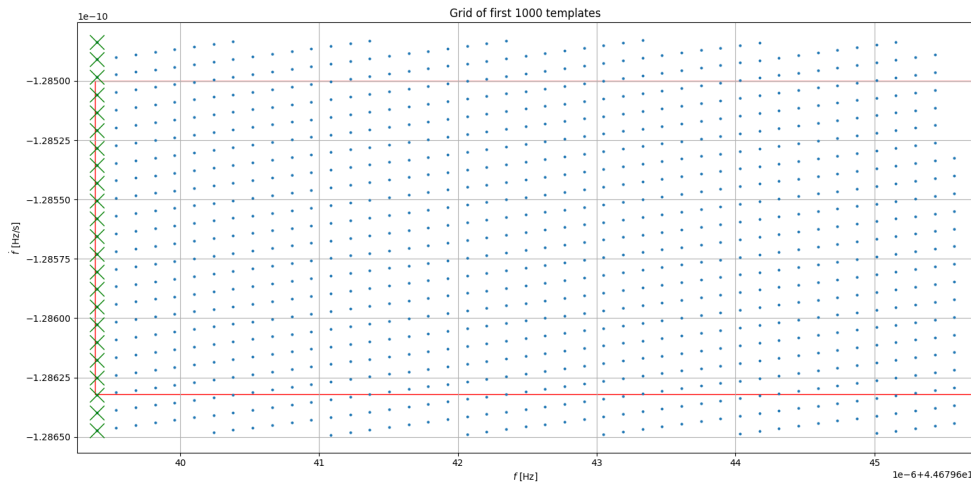


Figure 4.14: Grid of first order spindown vs frequency, region of interest

Regarding the grid generation, given that we only have frequency and first order spindown

available for this target, we can only create a pair of grid plots. Figure 4.14 shows the first 1000 points of the grid. There are around 1, 2 or even 3 points outside of the box per column, which is expected from the “gridType=8” metric, in order to cover the whole area; since we only have one order of spindown for this target we have not used the `StricSpindownBounds` option, but we are comfortable with these few extra points.

In figure 4.15 one can see, for comparison, the total search range, which contains the whole grid with 7120630 templates, so this box has height and width the input bands (the green box’s height is “f1dotBand” and its width is “f0Band”). At this scale, the red box from the top is so tiny one cannot appreciate it, even though it is there.

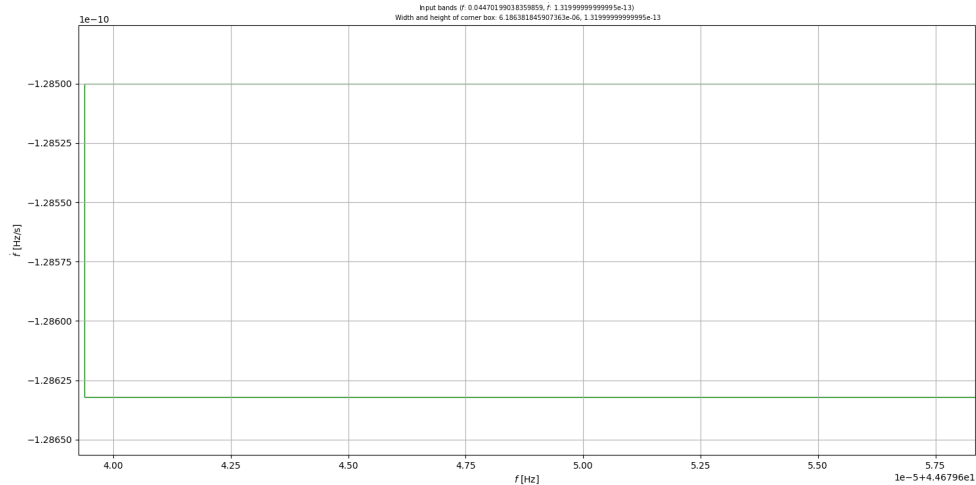
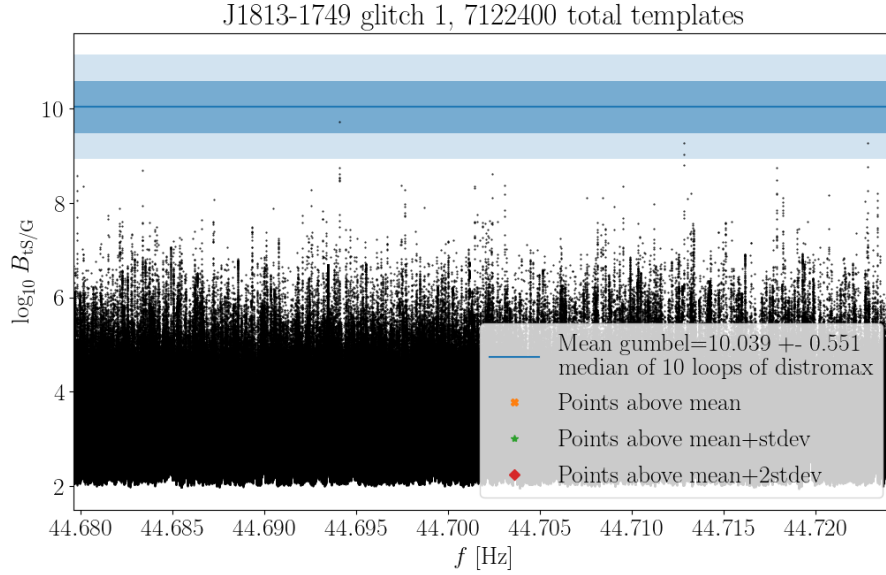


Figure 4.15: Grid of first order spindown vs frequency, whole search range

The last step before obtaining the results is to estimate the run time. We run a single job which takes approximately 25 minutes. Given that we will run 50 jobs, we expect a total run time of approximately 20 hours.

Now, the main results plots are the following ones. This pair of plots is one example of the several ones we obtain in this step. As stated before, we are working with both \mathcal{F} -statistic and \mathcal{B} -statistic, and for each method we obtain a scatter plot together with the corresponding Gumbel fit to the histogram of maximum values per batch, so the procedure is analogous in every case.

Figure 4.16: J1813-1749 $\log B_{ts/G}$ vs frequency

Here we can see the different points in the $\log_{10} B_{ts/G}$ against the corresponding frequency. We have used 1000 values per batch and no notching procedure has been performed (we do not use this tool unless we obtain a bad final distribution). Not a single value is above the threshold, which means we have not found any interesting outliers.

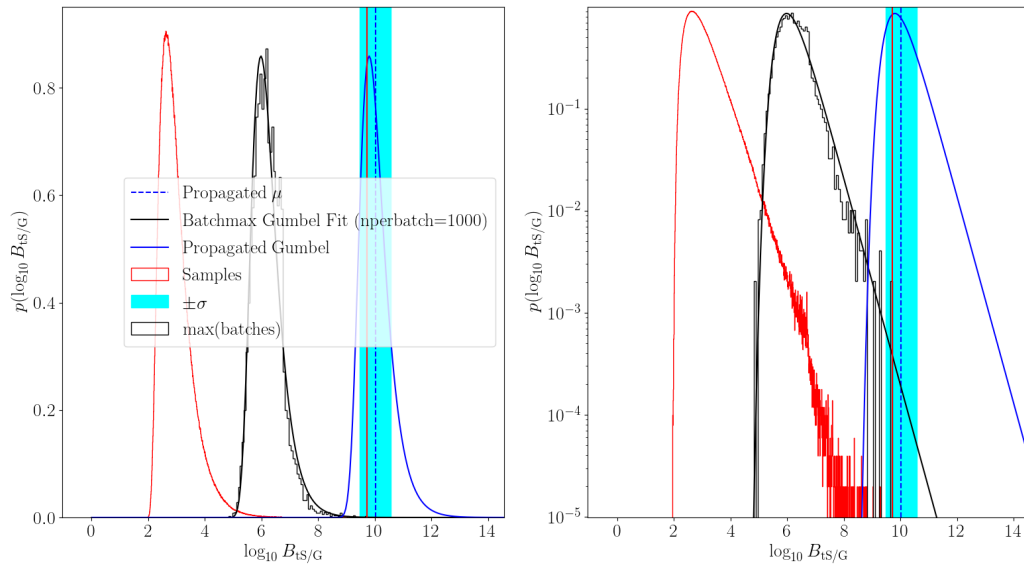
Figure 4.17: Sample, Gumbel fit to maximum values and propagated fit for J1813-1749, with \mathcal{B} -statistic. Linear and log scale.

Figure 4.17 shows the histogram of the maximum values of the statistic over batches of 1000 templates each, together with the corresponding Gumbel fit. As already discussed, the propagated fit –here in blue– is used in order to obtain the threshold and the standard deviation. In this case, 10.039 ± 0.551 .

For this present example, the Gumbel distribution fits well the histogram. The red vertical line, for context, is located at the maximum value of all the set. To be more confident, we decide that we can perform this process several times and obtain the definitive Gumbel mean and standard deviation as the median values of these processes. In our case, 10 performances have been done. The threshold with standard deviation in the scatter plot –figure 4.16– is already the median of all the processes, but this last figure is just one example, which can be compared with 9 other plots, very similar.

We can take a look at the other results, using the \mathcal{F} -statistic, in figures 4.18 and 4.19

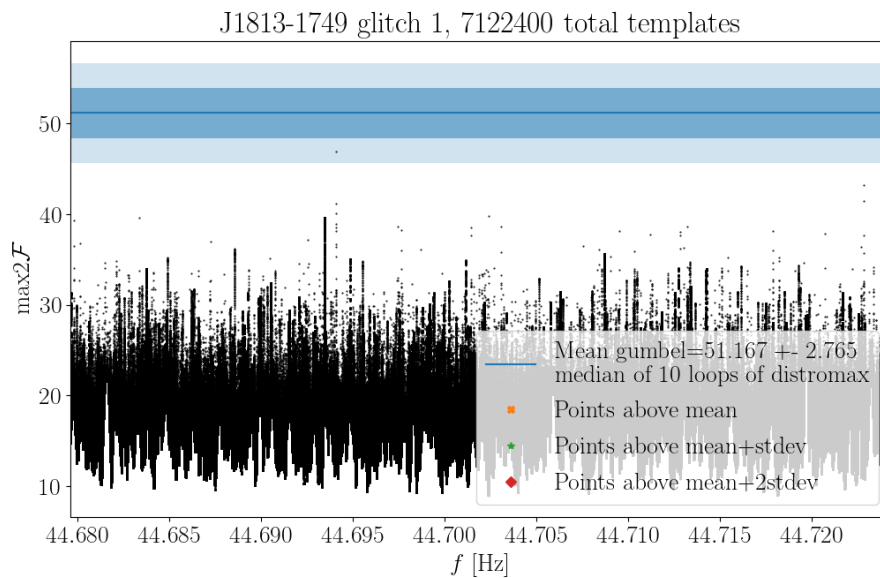


Figure 4.18: J1813-1749 2F vs frequency

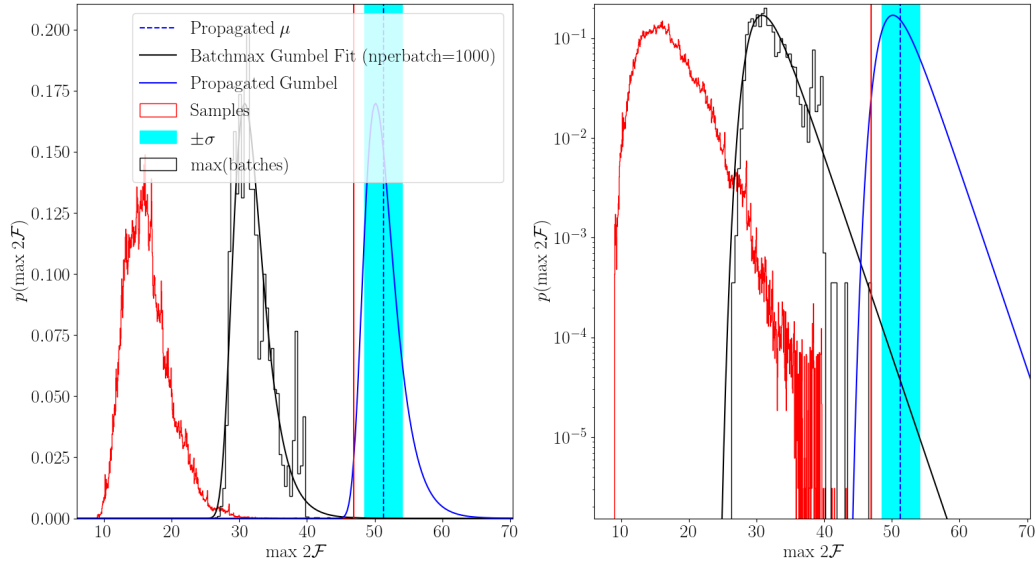
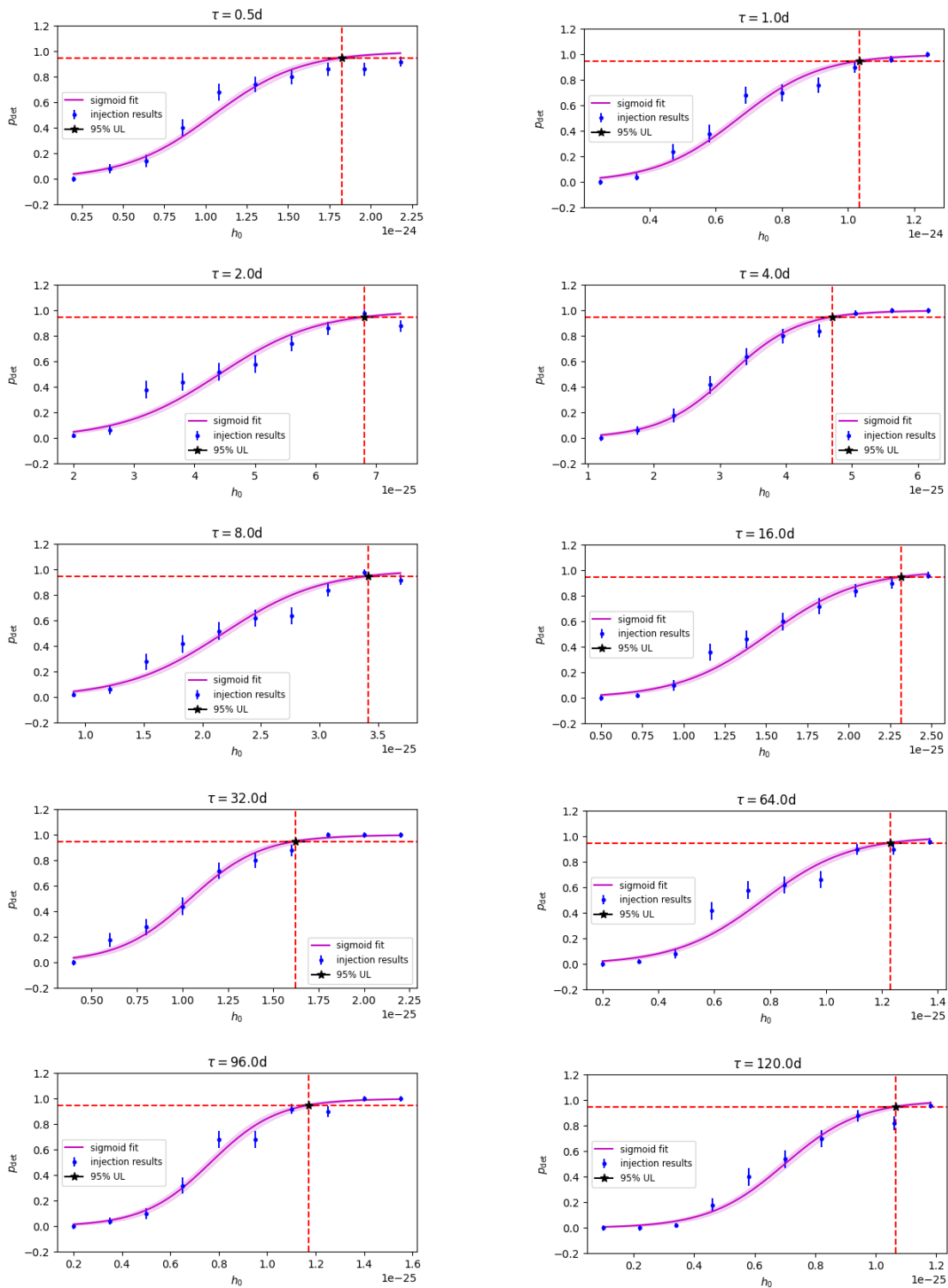


Figure 4.19: Sample, Gumbel fit to maximum values and propagated fit for J1813-1749, with \mathcal{F} -statistic. Linear and log scale.

The Gumbel fits to the histograms are less well behaved because the \mathcal{F} -statistic is more sensitive to short noise fluctuations, while the marginalised \mathcal{B} -statistic averages out better, and hence we decide to use \mathcal{B} -statistic as our final statistic.

Since we have not found any detection for this target, we proceed by calculating and plotting its upper limits. We generate an individual plot for each τ with the different probabilities of detection depending on the strain h_0 of the gravitational wave. We have chosen times from half a day up to 120 days, and, in this calculations, we are doing 50 injections at each τ and each h_0 step, with a total computing cost of 31 hours. Then, the sigmoid fit is computed and we can appreciate it fits well the behaviour of the probabilities along the strains h_0 . All the plots are included in the next page.

Figure 4.20: Probability of detection vs strain h_0 for all considered τ

Fitting the curve and calculating $h_0^{95\%}$, like any of the cases of [figure 4.20](#) allows us to properly plot the relation between the duration of the signal and the probability of detection at 95% confidence. This is [figure 4.21](#).

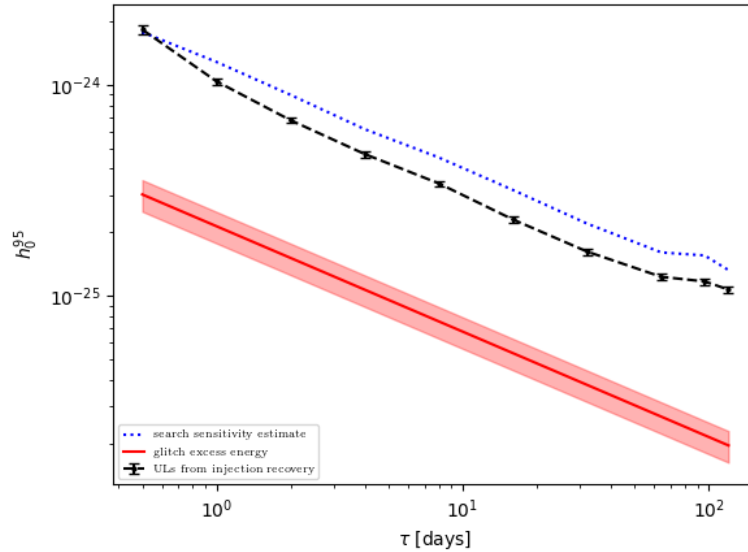


Figure 4.21: 95% probability of detection vs τ with estimated sensitivity and glitch excess energy indirect upper limit for comparison

The ULs curve is quite similar to the estimated one –in blue–. But both curves are far above the indirect UL from glitch excess energy in red. This means that it is physically impossible that we could detect a signal with our current sensitivity. In the final chapter an extra study of the upper limits for all the targets has been included, analysing a third generation detector for comparison.

4.5.2 Preliminary J1105-6107 results

One target that needs an extra treatment is J1105-6107. This pulsar has a rotational frequency of 15.83 Hz, which leads to a gravitational wave frequency of 31.64 Hz. The interesting glitch that this pulsar suffered took place on 58582.24 MJD and its intensity –in other words, the relative frequency change– was $1.17 \cdot 10^{-6}$. This is also an interesting target because through the indirect upper limits that have been done in [past sections](#) we have found a ratio between its indirect energy limits and the sensitivity curve at its particular frequency of 0.7279, the maximum value among all the targets.

What happened with this target is that we find something strange while doing a preliminary process to determine the Gumbel mean, [figure 4.20, a](#)). There is one big line at the

center of the frequency range which seems to be consequence of some line that was not cleaned in the Virgo detector. The problematic line can be identified in [figure 4.21](#), at approximately 36.643 Hz. Even though it is not the biggest line of the PSD it seems to be the only relevant one here.

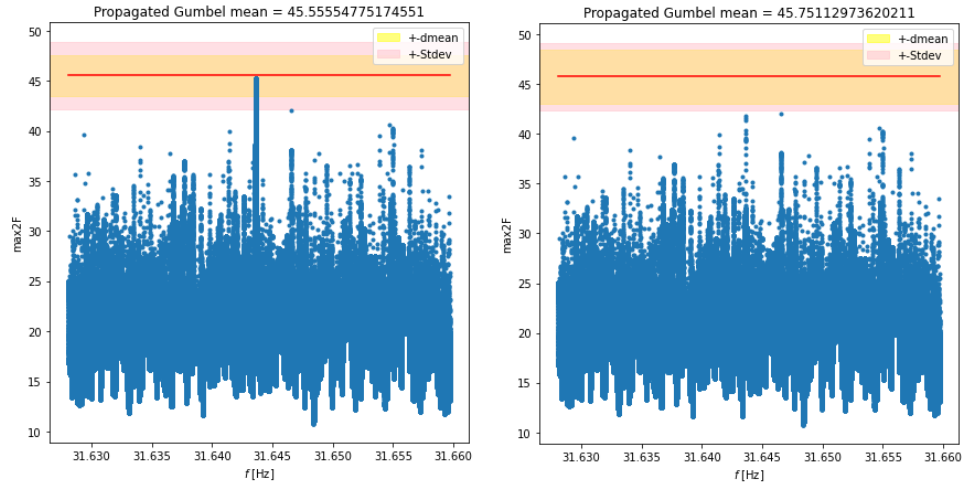


Figure 4.22: $\max(2F)$ along the range of frequencies of the J1105-6107 search, before and after rerunning job

For this target we performed several jobs with different frequency ranges for each one, so we decide to rerun only the particular job that contained the frequency at which we have found the peak just excluding the Virgo detector. If we do that, as expected, that line disappears, [figure 4.20, b](#)).

J1105-6107 glitch1: 1238780740–1249148740 GPS (20190408–20190806)

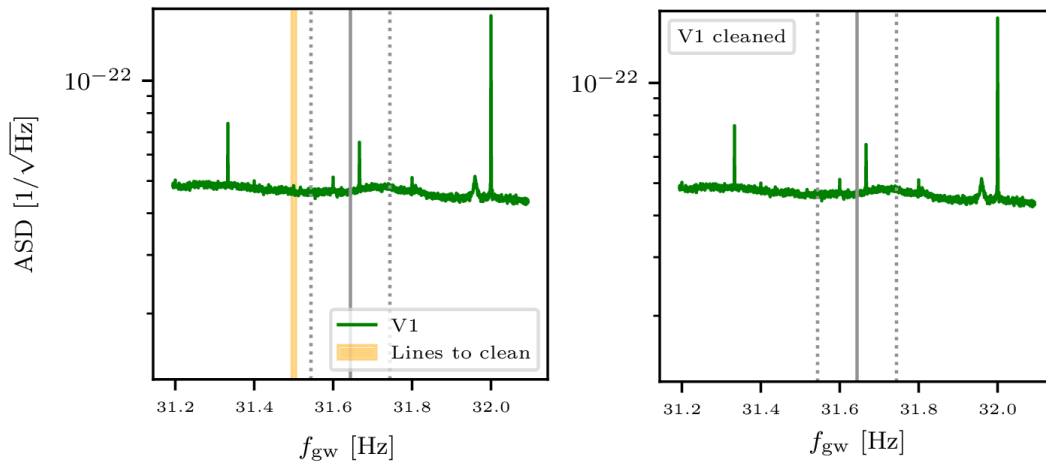


Figure 4.23: J1105-6107 Virgo detector PSD before and after cleaning

Now, going through the main procedure we find in the plots how the Virgo line is still showing up, but now is quite more irrelevant, below threshold –figure 4.22–:

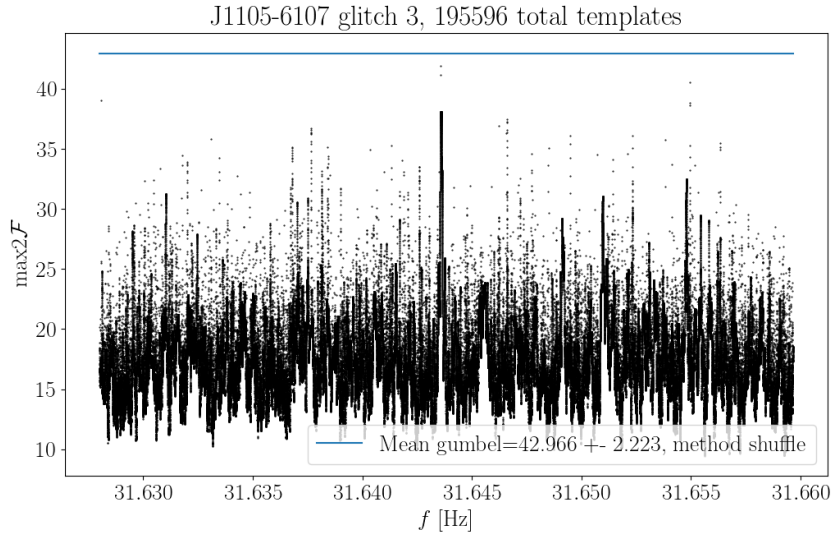


Figure 4.24: $\max(2F)$ along the frequency range for J1105-6107

First we try to change some of the options for the plot (like ignoring notching, changing the size of batches –since we have very few templates, it seems a good option to reduce its number per batch–, among others), but we do not reach a solid conclusion. We decide to do some diagnosis plots to see how the notching is killing some values of that Virgo peak, figure 4.23

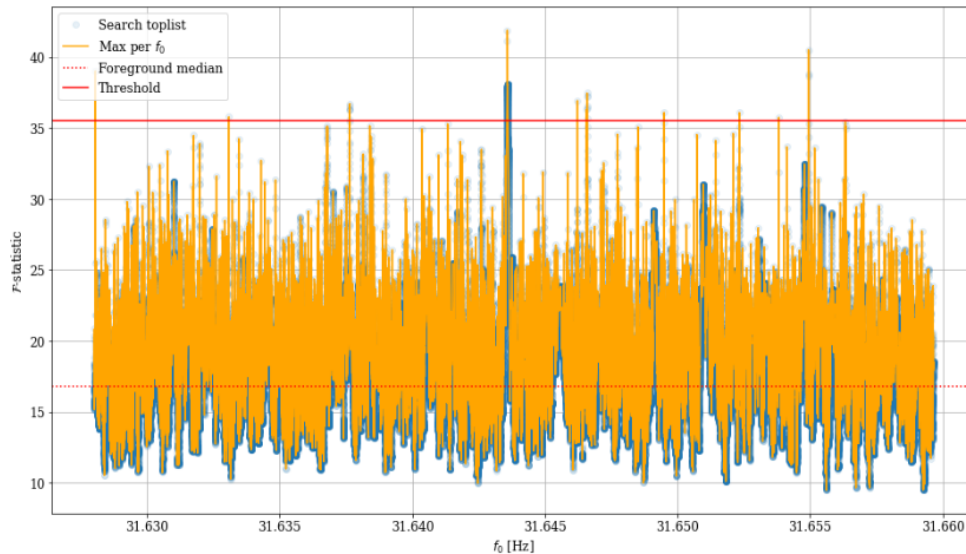


Figure 4.25: Diagnosis with \mathcal{F} -statistic. $\text{Max}(2F)$ vs frequency

Seeing that probably we are notching too much, the next step is to try what changes if we manually place the threshold. After doing some tests with different threshold values and different sizes of every batch, we conclude that the best we can do is what we obtain, for example, in figure 4.24. In that figure, after realizing that with different values of batch sizes and thresholds we obtain different reasonable values of the propagated mean and standard deviation, we decide to do a last test: we run 600 independent searches with 600 random new sky locations. This way we will not see any real signal from that pulsar but we would see the same data projected onto different templates. Taking the highest value of each run and, again, plotting the histogram and the corresponding Gumbel fit gives us the green histogram and fit.

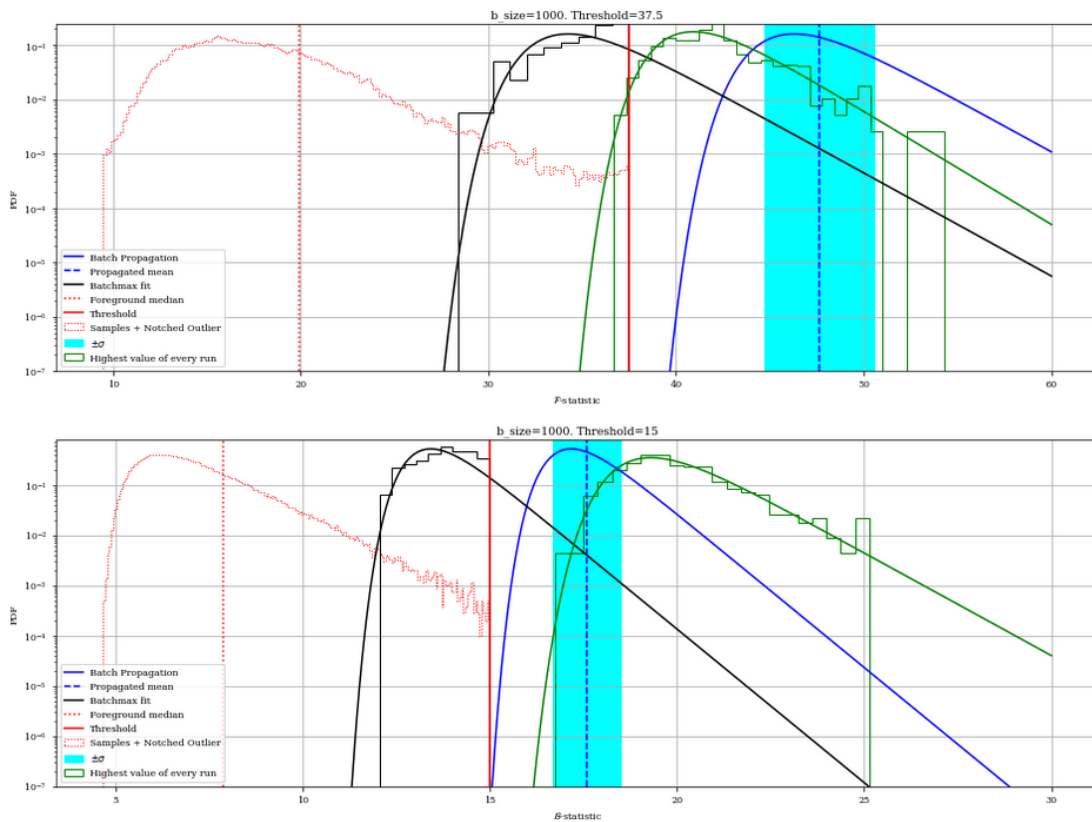


Figure 4.26: Final histograms and fits, including results from 600 random sky locations

In conclusion, given the low number of templates we have with J1105-6107, the Gumbel fit looked a bit strange, so doing a set of off-source runs gives us more robust results.

At the end, this case –in opposition to J1813-1749– will not be included in the main paper exactly as it is presented here, since a rerun has to be performed.

4.5.3 Overview of the full search

In this project we have analysed 6 glitching pulsars, one of them with 4 glitches and the rest with only 1 each. The following table summarizes the state of the search for all these targets as of the submission of this thesis, including the number of templates and run time (estimated –EST RT– and actual –RT– if the full search or upper limits calculation has been performed):

Target	Search	ULs	Templates	Est RT (h)	RT (h)	ULs RT (h)
J0534+2200	✓	✓	3917139	17	15	30.6
J0537-6910 5	✓	✓	593911	0.03	0.18	23
J0537-6910 6	✓	✓	11474334	40.5	287	102
J0537-6910 7	✓	✗	15837589	106.5	83	-
J0537-6910 8	✓	✗	21543992	296	190	-
J0908-4913	✓	✓	507911	< 1	0.13	9.7
J1105-6107	✓	✓	61497*	0.5	0.3	36.8
J1813-1749	✓	✓	7120630	20	25	31
J1826-1334	✓	✓	22753*	1.3	0.8	44

The run times for all the targets are, at the end, very low. The most expensive target to run is the 6th glitch of J0537-6910 with less than 300 core hours. Two of the pulsars, J1105-6107 and J1826-1334, have a considerably small number of templates which indicates that it is advisable to do the off-sourcing procedure already explained in the [previous section](#).

At the current date, 7 of the 9 total candidates taken into account have been fully analysed and no outliers have been found for any of them.

Chapter 5

Conclusion and future work

Continuous waves are a particular kind of gravitational waves characterized by being emitted continuously at a nearly fixed frequency and having typically much less amplitude than the so-called, already detected, transient gravitational waves.

The astrophysical community has searched for continuous gravitational waves during decades. Although their detection has been impossible for years, it seems that finally it is getting closer, thanks to the numerous improvements in detection tools.

In this work we have shown the procedure of searching for gravitational waves produced in events called pulsar glitches. Those are sudden increases of a pulsar's rotation frequency that can possibly lead to the emission of wavelike perturbations of space-time. Since these perturbations have similar characteristics to CWs, but they last commonly less than three months, we call these waves transient continuous waves.

We have found 6 targets of interest. These are all pulsars that suffered at least one glitch during the O3 period of Advanced LIGO and Virgo and that present more than 5 Hz of rotation frequency, which in our case is equivalent to 10 Hz of GW frequency, what we consider the minimum detectable.

The search, performed with the transient \mathcal{F} -statistic and \mathcal{B} -statistic, has not reported interesting outliers to follow up, but even so upper limits have been executed in order to compare the maximum possible strain of the events with the sensitivity of the current detectors. In some sense, we have checked how far we are to detect signals from this events.

At the end, the results for a specific target, J1813-1749, fully described here, show how we need more sensitivity if we want to finally measure a GW emission from a pulsar like this one. The process performed for the rest of the targets is not included here in detail because it has not been done exclusively by the author, and it is covered in the main paper, to which this present project contributes.

Summarizing, we have seen how we need an improvement in sensibility in order to finally

detect this kind of waves. This is a problem constantly in mind of the community, and the state of the question is based on a strong bet for two new generation detectors: the Einstein Telescope (ET) and LISA –already mentioned in this work–.

The ET [103], based on the morphology of the second generation interferometers currently working, is a new generation observatory that will increase the size of the arms up to 10 km. It will also present some others improvements, like being constructed underground, a cryogenic system, new quantum technologies to reduce the fluctuations of the light, and a set of noise-mitigation measures to reduce perturbations from the environment, achieving this way the most sensitive instrument for gravitational wave detection ever created. This project is planned to start during the next decade, even though the site where the telescope will be located is still uncertain.

On the other hand, LISA [54] will be a space based observatory, and it will consists of three spacecrafts orbiting the Sun in a triangular configuration. The three satellites, separated by 2.5 million km, will form a high precision interferometer that will sense gravitational waves by analysing changes in distance between free falling test masses inside those spacecrafts. The idea behind this project is to surpass the frequency limits of ground based observatories, with which we are not capable of detecting signals at lower frequencies. With LISA we will be able to take a look at bands of frequencies not observed before, from about 0.1 mHz to 100 mHz, where the Universe is richly populated by strong sources of gravitational waves.

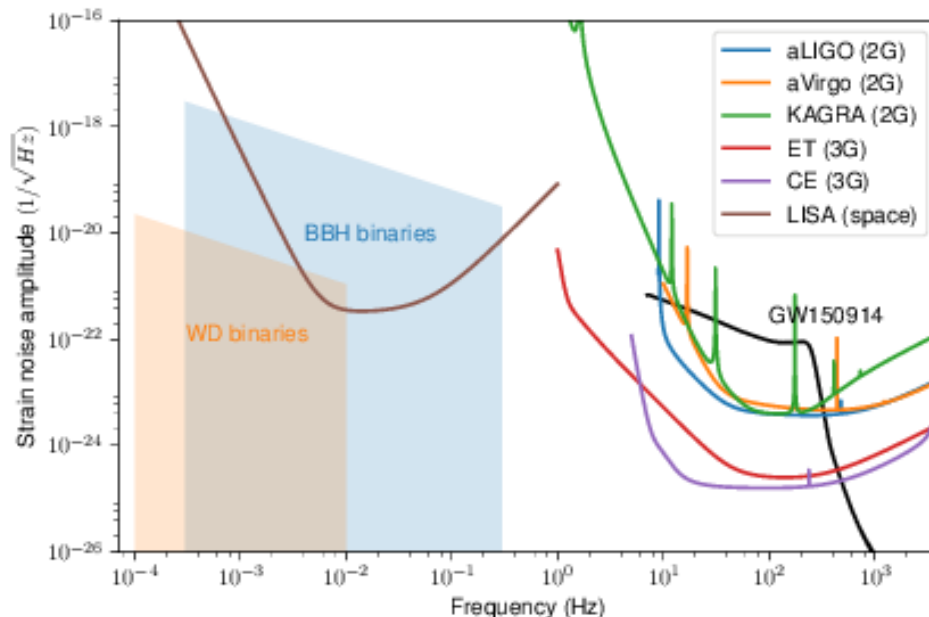


Figure 5.1: Sensitivity curve comparison between current detectors, ET, LISA and CE (another third-generation gravitational wave observatory). Credit: [104]

If we take a look at the expected sensitivity curve for the ET [105] [106] and we compare

it with the indirect energy upper limits we have calculated in [section 4.1.4](#) we can see how we would likely detect signals from the pulsars we have studied, if they glitch again with similar parameters in the 2030s. Here we have calculated the maximum strain of each targets with the definitive threshold for every one of them, unlike in the previous figure we have done in that section, so the results can be slightly different.

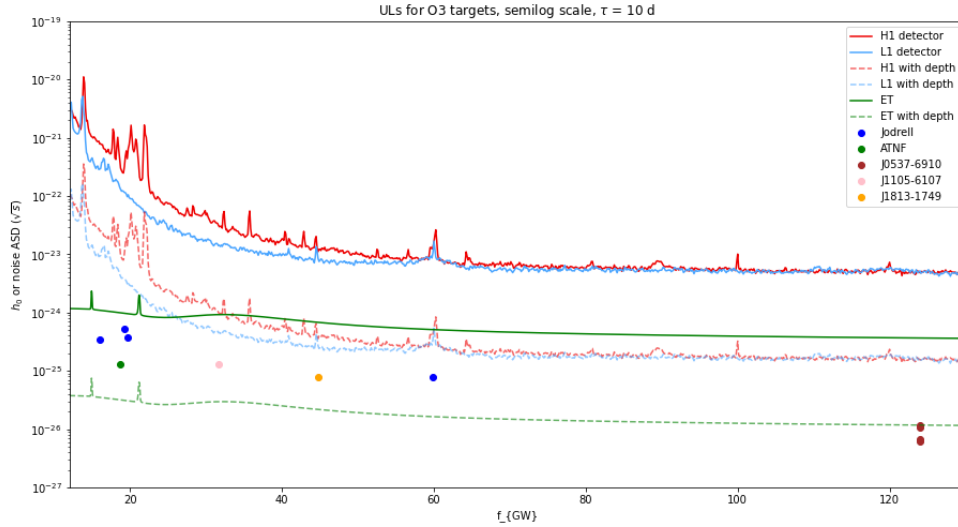


Figure 5.2: Sensitivity curve of LIGO detectors and future ET with indirect upper limits.

In particular, all the targets we have analysed are above the ET sensitivity curve –with the depth factor– except J0537-6910. Here we have used the same depth factor \mathcal{D} as we used in the preliminary test with the Hanford and Livingston detectors. Although this is not perfectly accurate, because the \mathcal{D} depends on the duty factors of each detector, in principle it should not vary too much to be relevant in this test.

With these enormous projects, some fundamental physics and cosmology questions may be answered finally, or at least will bring us closer to that answer. The physics near black-hole horizons, the dark matter and the dark energy are just some examples of the questions that they will help on. More related to this work’s topic, the huge sensitivity of both observatories could let us observe neutron-star merger and post-merger phases, providing an unprecedented insight into the interior structure of these stellar objects.

Bibliography

- [1] A. Einstein. “Die Grundlage der allgemeinen Relativitätstheorie”. In: *Annalen der Physik* 354.7 (Jan. 1916), pp. 769–822. DOI: [10.1002/andp.19163540702](https://doi.org/10.1002/andp.19163540702).
- [2] A. Einstein. “Näherungsweise Integration der Feldgleichungen der Gravitation”. In: *Sitzungsberichte der Königlich Preussischen Akademie der Wissenschaften (Berlin)* (Jan. 1916), pp. 688–696.
- [3] A. Einstein. “Über Gravitationswellen”. In: *Sitzungsberichte der Königlich Preussischen Akademie der Wissenschaften (Berlin)* (Jan. 1918), pp. 154–167.
- [4] H. Poincaré. *Sur la dynamique de l'électron*. Circolo Matematico di Palermo, 1906.
- [5] B. P. Abbott et al. “Observation of Gravitational Waves from a Binary Black Hole Merger”. In: *Physical Review Letter* 116.6 (Feb. 2016). DOI: [10.1103/PhysRevLett.116.061102](https://doi.org/10.1103/PhysRevLett.116.061102).
- [6] A Królak and M Patil. “The First Detection of Gravitational Waves”. In: *Universe* 3.3 (2017). ISSN: 2218-1997. DOI: [10.3390/universe3030059](https://doi.org/10.3390/universe3030059).
- [7] R. Prix and B. Krishnan. “Targeted search for continuous gravitational waves: Bayesian versus maximum-likelihood statistics”. In: *Classical and Quantum Gravity* 26.20 (Oct. 2009), p. 204013. DOI: [10.1088/0264-9381/26/20/204013](https://doi.org/10.1088/0264-9381/26/20/204013).
- [8] R. Hulse and H. Taylor. “Discovery of a Pulsar in a Close Binary System.” In: *The Astrophysical Journal* 6 (Aug. 1974), p. 453. DOI: [10.1111/j.1749-6632.1975.tb31467.x](https://doi.org/10.1111/j.1749-6632.1975.tb31467.x).
- [9] A. A. Michelson and E. W. Morley. “On the relative motion of the Earth and the luminiferous ether”. In: *American Journal of Science* 34.203 (Nov. 1887), pp. 333–345. DOI: [10.2475/ajs.s3-34.203.333](https://doi.org/10.2475/ajs.s3-34.203.333).
- [10] J. Aasi et al. “Gravitational waves from known pulsars: results from the initial detector era”. In: *The Astrophysical Journal* 785.2 (2014), p. 119.
- [11] *Wikipedia, GW observatory*. https://en.wikipedia.org/wiki/Gravitational-wave_observatory. Accessed: 2021-09-30.
- [12] F. Acernese et al. “Advanced Virgo: a second-generation interferometric gravitational wave detector”. In: *Classical and Quantum Gravity* 32.2 (2015), p. 024001. DOI: [10.1088/0264-9381/32/2/024001](https://doi.org/10.1088/0264-9381/32/2/024001). arXiv: [1408.3978](https://arxiv.org/abs/1408.3978) [gr-qc].

- [13] *LVK interferometers*. <https://www.ligo.caltech.edu/news/ligo20191004>. Accessed: 2021-09-30.
- [14] R. Weiss. “Electromagnetically coupled broadband gravitational antenna”. In: *Quarterly Progress Report, Research Laboratory of Electronics (MIT)* 105 (1972), pp. 54–76.
- [15] B. P. Abbott et al. “Binary Black Hole Mergers in the First Advanced LIGO Observing Run”. In: *Physical Review X* 6.4 (Oct. 2016). ISSN: 2160-3308. DOI: [10.1103/physrevx.6.041015](https://doi.org/10.1103/physrevx.6.041015).
- [16] B. P. Abbott et al. “GWTC-1: A Gravitational-Wave Transient Catalog of Compact Binary Mergers Observed by LIGO and Virgo during the First and Second Observing Runs”. In: *Physical Review X* 9.3 (Sept. 2019). ISSN: 2160-3308. DOI: [10.1103/physrevx.9.031040](https://doi.org/10.1103/physrevx.9.031040).
- [17] B. P. Abbott et al. “GW170817: Observation of Gravitational Waves from a Binary Neutron Star Inspiral”. In: *Physical Review Letter* 119 (16 Oct. 2017), p. 161101. DOI: [10.1103/PhysRevLett.119.161101](https://doi.org/10.1103/PhysRevLett.119.161101).
- [18] R. Abbott et al. “GWTC-2: Compact Binary Coalescences Observed by LIGO and Virgo during the First Half of the Third Observing Run”. In: *Physical Review X* 11.2 (June 2021). ISSN: 2160-3308. DOI: [10.1103/physrevx.11.021053](https://doi.org/10.1103/physrevx.11.021053).
- [19] R. Abbott et al. “Gravitational-wave Constraints on the Equatorial Ellipticity of Millisecond Pulsars”. In: *The Astrophysical Journal Letters* 902.1 (Oct. 2020), p. L21. ISSN: 2041-8213. DOI: [10.3847/2041-8213/abb655](https://doi.org/10.3847/2041-8213/abb655).
- [20] B. Krishnan et al. “The Hough transform search for continuous gravitational waves”. In: *Physical Review D* 70 (2004), p. 082001. DOI: [10.1103/PhysRevD.70.082001](https://doi.org/10.1103/PhysRevD.70.082001). arXiv: [gr-qc/0407001](https://arxiv.org/abs/gr-qc/0407001).
- [21] P. B. Covas and A. M. Sintes. “New method to search for continuous gravitational waves from unknown neutron stars in binary systems”. In: *Physical Review D* 99.12 (2019), p. 124019. DOI: [10.1103/PhysRevD.99.124019](https://doi.org/10.1103/PhysRevD.99.124019). arXiv: [1904.04873](https://arxiv.org/abs/1904.04873) [[astro-ph.IM](https://arxiv.org/abs/1904.04873)].
- [22] R. Abbott et al. “All-sky search in early O3 LIGO data for continuous gravitational-wave signals from unknown neutron stars in binary systems”. In: *Physical Review D* 103.6 (Mar. 2021). ISSN: 2470-0029. DOI: [10.1103/physrevd.103.064017](https://doi.org/10.1103/physrevd.103.064017).
- [23] R. Tenorio, LIGO Scientific Collaboration, and Virgo Collaboration. *An all-sky search in early O3 LIGO data for continuous gravitational-wave signals from unknown neutron stars in binary systems*. 2021. arXiv: [2105.07455](https://arxiv.org/abs/2105.07455) [[gr-qc](https://arxiv.org/abs/2105.07455)].
- [24] R. Abbott et al. “Diving below the Spin-down Limit: Constraints on Gravitational Waves from the Energetic Young Pulsar PSR J0537-6910”. In: *The Astrophysical Journal Letters* 913.2 (May 2021), p. L27. ISSN: 2041-8213. DOI: [10.3847/2041-8213/abffcd](https://doi.org/10.3847/2041-8213/abffcd).

- [25] The LIGO Scientific Collaboration et al. *Constraints from LIGO O3 data on gravitational wave emission due to r-modes in the glitching pulsar PSR J0537-6910*. 2021. arXiv: [2104.14417 \[astro-ph.HE\]](#).
- [26] The LIGO Scientific Collaboration et al. *Searches for continuous gravitational waves from young supernova remnants in the early third observing run of Advanced LIGO and Virgo*. 2021. arXiv: [2105.11641 \[astro-ph.HE\]](#).
- [27] The LIGO Scientific Collaboration et al. *Constraints on dark photon dark matter using data from LIGO's and Virgo's third observing run*. 2021. arXiv: [2105.13085 \[astro-ph.CO\]](#).
- [28] The LIGO Scientific Collaboration et al. *All-sky Search for Continuous Gravitational Waves from Isolated Neutron Stars in the Early O3 LIGO Data*. 2021. arXiv: [2107.00600 \[gr-qc\]](#).
- [29] The LIGO Scientific Collaboration et al. *Search for continuous gravitational waves from 20 accreting millisecond X-ray pulsars in O3 LIGO data*. 2021. arXiv: [2109.09255 \[astro-ph.HE\]](#).
- [30] T. Akutsu et al. “KAGRA: 2.5 Generation Interferometric Gravitational Wave Detector”. In: *Nature Astronomy* 3.1 (2019), pp. 35–40. DOI: [10.1038/s41550-018-0658-y](#). arXiv: [1811.08079 \[gr-qc\]](#).
- [31] P. B. Covas et al. “Identification and mitigation of narrow spectral artifacts that degrade searches for persistent gravitational waves in the first two observing runs of Advanced LIGO”. In: *Physical Review D* 97.8 (Apr. 2018). ISSN: 2470-0029. DOI: [10.1103/physrevd.97.082002](#).
- [32] Ting Hong. “Brownian Thermal Noise in Interferometric Gravitational Wave Detectors and Single Photon Optomechanics”. PhD thesis. California Institute of Technology, Jan. 2013.
- [33] *UIB plan for future GW astronomy*. <http://iac3.uib.es/2015/12/23/planning-for-a-bright-tomorrow-prospects-for-gravitational-wave-astronomy-with-advanced-ligo-and-advanced-virgo/>. Accessed: 2021-09-30.
- [34] B. P. Abbott et al. “Properties of the Binary Neutron Star Merger GW170817”. In: *Physical Review X* 9.1 (Jan. 2019). ISSN: 2160-3308. DOI: [10.1103/physrevx.9.011001](#).
- [35] C. J. Moore, R. H. Cole, and C. P. L. Berry. “Gravitational-wave sensitivity curves”. In: *Classical and Quantum Gravity* 32.1 (Dec. 2014), p. 015014. ISSN: 1361-6382. DOI: [10.1088/0264-9381/32/1/015014](#).
- [36] G. Turin. “An introduction to matched filters”. In: *IRE Transactions on Information Theory* 6.3 (1960), pp. 311–329. DOI: [10.1109/TIT.1960.1057571](#).
- [37] W. Baade and F. Zwicky. “Remarks on Super-Novae and Cosmic Rays”. In: *Physical Review* 46 (1 July 1934), pp. 76–77. DOI: [10.1103/PhysRev.46.76.2](#).

- [38] James C. “The existence of a neutron”. In: *Proceedings of the Royal Society of London A* 136 (1 June 1932), pp. 692–708. DOI: [10.1098/rspa.1932.0112](https://doi.org/10.1098/rspa.1932.0112).
- [39] A. Hewish et al. “Observation of a Rapidly Pulsating Radio Source”. In: 217.5130 (Feb. 1968), pp. 709–713. DOI: [10.1038/217709a0](https://doi.org/10.1038/217709a0).
- [40] P. Cerda and N. Elias. “Neutron Stars Formation and Core Collapse Supernovae”. In: *Astrophysics and Space Science Library* (2018), pp. 1–56. ISSN: 2214-7985. DOI: [10.1007/978-3-319-97616-7_1](https://doi.org/10.1007/978-3-319-97616-7_1).
- [41] F. Özel and P. Freire. “Masses, Radii, and the Equation of State of Neutron Stars”. In: *Annual Review of Astronomy and Astrophysics* 54.1 (2016), pp. 401–440. DOI: [10.1146/annurev-astro-081915-023322](https://doi.org/10.1146/annurev-astro-081915-023322).
- [42] V. S. Beskin. “Radio pulsars”. In: *Physics-Uspekhi* 42.11 (Nov. 1999), pp. 1071–1098. DOI: [10.1070/pu1999v042n11abeh000665](https://doi.org/10.1070/pu1999v042n11abeh000665).
- [43] P. Haensel, A. Y. Potekhin, and D. G. Yakovlev. *Neutron Stars*. Springer, 2007.
- [44] D. R. Lorimer. “Binary and Millisecond Pulsars”. In: *Living Reviews in Relativity* 11.1 (Nov. 2008). ISSN: 1433-8351. DOI: [10.12942/lrr-2008-8](https://doi.org/10.12942/lrr-2008-8).
- [45] D. C. Backer. “The 1.5-millisecond pulsar.” In: *Annals of the New York Academy of Sciences* 422.1 (Jan. 1984), pp. 180–181. DOI: [10.1111/j.1749-6632.1984.tb23351.x](https://doi.org/10.1111/j.1749-6632.1984.tb23351.x).
- [46] J. G. Hartnett and A. N. Luiten. “Colloquium: Comparison of astrophysical and terrestrial frequency standards”. In: *Reviews of Modern Physics* 83.1 (Jan. 2011), pp. 1–9. DOI: [10.1103/RevModPhys.83.1](https://doi.org/10.1103/RevModPhys.83.1). arXiv: [1004.0115 \[astro-ph.IM\]](https://arxiv.org/abs/1004.0115).
- [47] P. M. Woods and C. Thompson. *Compact Stellar X-ray Sources*. Cambridge Astrophysics. Cambridge University Press, 2006. DOI: [10.1017/CB09780511536281](https://doi.org/10.1017/CB09780511536281).
- [48] D. L. Kaplan and M. H. van Kerkwijk. “Constraining the spin-down of the nearby isolated neutron star RX J0806.4-4123, and implications for the population of nearby stars”. In: *The Astrophysical Journal* 705 (2009), pp. 798–808.
- [49] G. Srinivasan. “Recycled pulsars”. In: *New Astronomy Reviews* 54.3 (2010). Proceedings: A Life With Stars, pp. 93–100. ISSN: 1387-6473. DOI: <https://doi.org/10.1016/j.newar.2010.09.026>.
- [50] *NASA’s Goddard Space Flight Center/Conceptual Image Lab*. <https://svs.gsfc.nasa.gov/20267>. Accessed: 2021-09-30.
- [51] G. Yim and D. I. Jones. “Transient gravitational waves from pulsar post-glitch recoveries”. In: *Monthly Notices of the Royal Astronomical Society* 498.3 (Aug. 2020), pp. 3138–3152. ISSN: 1365-2966. DOI: [10.1093/mnras/staa2534](https://doi.org/10.1093/mnras/staa2534).
- [52] J. Middleditch et al. “Predicting the Starquakes in PSR J0537-6910”. In: *Astrophys. J.* 652 (2006), pp. 1531–1546. DOI: [10.1086/508736](https://doi.org/10.1086/508736). arXiv: [astro-ph/0605007](https://arxiv.org/abs/astro-ph/0605007).

- [53] E. Giliberti and G. Cambiotti. *Starquakes in millisecond pulsars and gravitational waves emission*. 2021. arXiv: [2102.02540](https://arxiv.org/abs/2102.02540) [astro-ph.HE].
- [54] *Laser Interferometer Space Antenna*. <https://www.elisascience.org/>. Accessed: 2021-10-04.
- [55] *LIGO Continuous Waves*. <https://www.ligo.org/science/GW-Continuous.php>. Accessed: 2021-09-30.
- [56] P. Jaranowski, A. Królak, and B. F. Schutz. “Data analysis of gravitational wave signals from spinning neutron stars: The signal and its detection”. In: *Physical Review D* 58.6 (Aug. 1998). ISSN: 1089-4918. DOI: [10.1103/PhysRevD.58.063001](https://doi.org/10.1103/PhysRevD.58.063001).
- [57] B. P. Abbott et al. “Search for Gravitational Waves from a Long-lived Remnant of the Binary Neutron Star Merger GW170817”. In: *The Astrophysical Journal* 875.2 (Apr. 2019), p. 160. DOI: [10.3847/1538-4357/ab0f3d](https://doi.org/10.3847/1538-4357/ab0f3d).
- [58] N. Sarin and P. D. Lasky. “The evolution of binary neutron star post-merger remnants: a review”. In: *General Relativity and Gravitation* 53.6 (June 2021). ISSN: 1572-9532. DOI: [10.1007/s10714-021-02831-1](https://doi.org/10.1007/s10714-021-02831-1).
- [59] Miroslav Shaltev. “Optimization and follow-up of semicoherent searches for continuous gravitational waves”. PhD thesis. Fakultät für Mathematik und Physik, Gottfried Wilhelm Leibniz Universität Hannover, 2013. URL: <http://opac.tib.uni-hannover.de/DB=1/XMLPRS=N/PPN?PPN=755483928>.
- [60] P. B. Covas. “Effects of proper motion of neutron stars on continuous gravitational-wave searches”. In: *Monthly Notices of the Royal Astronomical Society* 500.4 (Nov. 2020), pp. 5167–5176. ISSN: 0035-8711. DOI: [10.1093/mnras/staa3624](https://doi.org/10.1093/mnras/staa3624).
- [61] J. Aasi et al. “Narrow-band search of continuous gravitational-wave signals from Crab and Vela pulsars in Virgo VSR4 data”. In: *Physical Review D* 91 (2 Jan. 2015), p. 022004. DOI: [10.1103/PhysRevD.91.022004](https://doi.org/10.1103/PhysRevD.91.022004).
- [62] R. Abbott. *Narrow-band searches for continuous and long-duration transient gravitational waves from known pulsars in the LIGO-Virgo third observing run*. Tech. rep. LIGO-P2100267. LIGO Scientific Collaboration, 2021. URL: <https://dcc.ligo.org/P2100267/>.
- [63] S. Mastrogiovanni et al. “An improved algorithm for narrow-band searches of continuous gravitational waves”. In: *Classical and Quantum Gravity* 34.13 (June 2017), p. 135007. DOI: [10.1088/1361-6382/aa744f](https://doi.org/10.1088/1361-6382/aa744f).
- [64] P. Astone et al. “A method for detection of known sources of continuous gravitational wave signals in non-stationary data”. In: *Classical and Quantum Gravity* 27.19 (Sept. 2010), p. 194016. DOI: [10.1088/0264-9381/27/19/194016](https://doi.org/10.1088/0264-9381/27/19/194016).
- [65] P. Astone et al. “Coherent search of continuous gravitational wave signals: extension of the 5-vectors method to a network of detectors”. In: *Journal of Physics: Conference Series* 363 (June 2012), p. 012038. DOI: [10.1088/1742-6596/363/1/012038](https://doi.org/10.1088/1742-6596/363/1/012038).

- [66] P. Astone, S. Frasca, and C. Palomba. “The short FFT database and the peak map for the hierarchical search of periodic sources”. In: *Classical and Quantum Gravity* 22.18 (Sept. 2005), S1197–S1210. DOI: [10.1088/0264-9381/22/18/s34](https://doi.org/10.1088/0264-9381/22/18/s34).
- [67] R. Prix, S. Giampanis, and C. Messenger. “Search method for long-duration gravitational wave transients from neutron stars”. In: *Physical Review D* 84 (2 July 2011), p. 023007. DOI: [10.1103/PhysRevD.84.023007](https://doi.org/10.1103/PhysRevD.84.023007).
- [68] David Keitel et al. “Search for continuous gravitational waves: Improving robustness versus instrumental artifacts”. In: *Physical Review D* 89 (6 Mar. 2014), p. 064023. DOI: [10.1103/PhysRevD.89.064023](https://doi.org/10.1103/PhysRevD.89.064023).
- [69] R. Prix. *The F-statistic and its implementation in ComputeFStatistic_v2*. Tech. rep. LIGO-T0900149-v6. LIGO Scientific Collaboration, 2021. URL: <https://dcc.ligo.org/LIGO-T0900149/public>.
- [70] R. Prix. “Search for continuous gravitational waves: Metric of the multi-detector F-statistic”. In: *Physical Review D* 75 (2007), p. 023004. DOI: [10.1103/PhysRevD.75.023004](https://doi.org/10.1103/PhysRevD.75.023004). arXiv: [gr-qc/0606088](https://arxiv.org/abs/gr-qc/0606088).
- [71] LIGO Scientific Collaboration. *LIGO Algorithm Library*. 2018. DOI: [10.7935/GT1W-FZ16](https://doi.org/10.7935/GT1W-FZ16).
- [72] K. Wette et al. “Implementing a semicoherent search for continuous gravitational waves using optimally-constructed template banks”. In: *Physical Review D* 97.12 (2018), p. 123016. DOI: [10.1103/PhysRevD.97.123016](https://doi.org/10.1103/PhysRevD.97.123016). arXiv: [1804.03392 \[astro-ph.IM\]](https://arxiv.org/abs/1804.03392).
- [73] *Wikipedia window functions*. https://en.wikipedia.org/wiki/Window_function. Accessed: 2021-10-01.
- [74] D. Keitel and G. Ashton. “Faster search for long gravitational-wave transients: GPU implementation of the transient \mathcal{F} -statistic”. In: *Classical and Quantum Gravity* 35.20 (Sept. 2018), p. 205003. DOI: [10.1088/1361-6382/aade34](https://doi.org/10.1088/1361-6382/aade34).
- [75] D. Keitel et al. “First search for long-duration transient gravitational waves after glitches in the Vela and Crab pulsars”. In: *Physical Review D* 100 (6 Sept. 2019), p. 064058. DOI: [10.1103/PhysRevD.100.064058](https://doi.org/10.1103/PhysRevD.100.064058).
- [76] *The ATNF Pulsar Catalogue*. <https://www.atnf.csiro.au/people/pulsar/psrcat/>. Accessed: 2021-08-25.
- [77] *The ATNF Pulsar Catalogue — Glitch Database*. <https://www.atnf.csiro.au/people/pulsar/psrcat/glitchTbl.html>. Accessed: 2021-08-25.
- [78] *Pulsar Glitches — Jodrell Bank Centre for Astrophysics*. <http://www.jb.man.ac.uk/pulsar/glitches.html>. Accessed: 2021-08-25.

- [79] K. Gendreau et al. “The Neutron star Interior Composition Explorer (NICER): design and development”. In: *Space Telescopes and Instrumentation 2016: Ultraviolet to Gamma Ray*. Ed. by Jan-Willem A. den Herder, Tadayuki Takahashi, and Marshall Bautz. Vol. 9905. International Society for Optics and Photonics. SPIE, 2016, pp. 420–435. DOI: [10.1117/12.2231304](https://doi.org/10.1117/12.2231304).
- [80] F. Jankowski et al. “The UTMOST pulsar timing programme I: Overview and first results”. In: *Monthly Notices of the Royal Astronomical Society* 484.3 (Dec. 2018), pp. 3691–3712. ISSN: 0035-8711. DOI: [10.1093/mnras/sty3390](https://doi.org/10.1093/mnras/sty3390). eprint: <https://academic.oup.com/mnras/article-pdf/484/3/3691/27723628/sty3390.pdf>.
- [81] Marcus E. Lower et al. “The UTMOST pulsar timing programme – II. Timing noise across the pulsar population”. In: *Mon. Not. Roy. Astron. Soc.* 494.1 (2020), pp. 228–245. DOI: [10.1093/mnras/staa615](https://doi.org/10.1093/mnras/staa615). arXiv: [2002.12481](https://arxiv.org/abs/2002.12481) [[astro-ph.HE](#)].
- [82] M. Bailes et al. “The UTMOST: A Hybrid Digital Signal Processor Transforms the Molonglo Observatory Synthesis Telescope”. In: *Publications of the Astronomical Society of Australia* 34 (2017), e045. DOI: [10.1017/pasa.2017.39](https://doi.org/10.1017/pasa.2017.39).
- [83] R. Abbott et al. “Diving below the spin-down limit: Constraints on gravitational waves from the energetic young pulsar PSR J0537-6910”. In: *Astrophysical Journal Letters* 913 (2021), p. L27. DOI: [10.3847/2041-8213/abffcd](https://doi.org/10.3847/2041-8213/abffcd). arXiv: [2012.12926](https://arxiv.org/abs/2012.12926) [[astro-ph.HE](#)].
- [84] W. Ho et al. “Return of the Big Glitch: NICER timing and glitches of PSR J0537-6910”. In: *Monthly Notices of the Royal Astronomical Society* 498 (Sept. 2020). DOI: [10.1093/mnras/staa2640](https://doi.org/10.1093/mnras/staa2640).
- [85] W. Ho et al. “Proper motion, spectra, and timing of PSR J1813–1749 using Chandra and NICER”. In: *Monthly Notices of the Royal Astronomical Society* 498.3 (2020), pp. 4396–4403. DOI: [10.1093/mnras/staa2653](https://doi.org/10.1093/mnras/staa2653). arXiv: [2009.00031](https://arxiv.org/abs/2009.00031) [[astro-ph.HE](#)].
- [86] M. E. Lower et al. “The UTMOST pulsar timing programme – II. Timing noise across the pulsar population”. In: *Monthly Notices of the Royal Astronomical Society* 494.1 (2020), pp. 228–245. DOI: [10.1093/mnras/staa615](https://doi.org/10.1093/mnras/staa615). arXiv: [2002.12481](https://arxiv.org/abs/2002.12481) [[astro-ph.HE](#)].
- [87] J. Middleditch et al. “Predicting the Starquakes in PSR J0537-6910”. In: *The Astrophysical Journal* 652.2 (Dec. 2006), pp. 1531–1546. ISSN: 1538-4357. DOI: [10.1086/508736](https://doi.org/10.1086/508736).
- [88] E. Parent et al. *Discovery of 72 pulsars in the PALFA survey: Timing analysis, glitch activity, emission variability, and a pulsar in an eccentric binary*. 2021. arXiv: [2108.02320](https://arxiv.org/abs/2108.02320) [[astro-ph.HE](#)].
- [89] C. Dreissigacker, R. Prix, and K. Wette. “Fast and accurate sensitivity estimation for continuous-gravitational-wave searches”. In: *Physical Review D* 98.8 (Oct. 2018). ISSN: 2470-0029. DOI: [10.1103/physrevd.98.084058](https://doi.org/10.1103/physrevd.98.084058).

- [90] K. Wette et al. “OctApps: a library of Octave functions for continuous gravitational-wave data analysis”. In: *Journal of Open Source Software* 3.26 (June 2018), p. 707. ISSN: 2475-9066. DOI: [10.21105/joss.00707](https://doi.org/10.21105/joss.00707).
- [91] J. Zweizig and K. Riles. *Information on self-gating of $h(t)$ used in O3 continuous-wave and stochastic searches*. Tech. rep. [LIGO-T2000384](https://dcc.ligo.org/LIGO-T2000384). LIGO Laboratory, 2021.
- [92] D. Davis et al. “LIGO detector characterization in the second and third observing runs”. In: *Classical and Quantum Gravity* 38.13 (2021), p. 135014. DOI: [10.1088/1361-6382/abfd85](https://doi.org/10.1088/1361-6382/abfd85). arXiv: [2101.11673](https://arxiv.org/abs/2101.11673) [astro-ph.IM].
- [93] E. Goetz et al. *O3a lines and combs found in self-gated C01 data*. Tech. rep. LIGO-T2100200. LIGO Laboratory, 2021. URL: <https://dcc.ligo.org/T2100200/public>.
- [94] O. Piccinni et al. *Virgo O3 List of Lines*. Tech. rep. LIGO-T2100141-v2. LIGO Laboratory, 2021. URL: <https://dcc.ligo.org/T2100141-v2/public>.
- [95] K. Wette. “Lattice template placement for coherent all-sky searches for gravitational wave pulsars”. In: *Physical Review D* 90.12 (Dec. 2014). ISSN: 1550-2368. DOI: [10.1103/physrevd.90.122010](https://doi.org/10.1103/physrevd.90.122010).
- [96] C. M. Espinoza et al. “A study of 315 glitches in the rotation of 102 pulsars”. In: *Monthly Notices of the Royal Astronomical Society* 414 (2011), pp. 1679–1704. DOI: [10.1111/j.1365-2966.2011.18503.x](https://doi.org/10.1111/j.1365-2966.2011.18503.x). arXiv: [1102.1743](https://arxiv.org/abs/1102.1743) [astro-ph.HE].
- [97] D. Thain, T. Tannenbaum, and M. Livny. “Distributed computing in practice: the Condor experience”. In: *Concurrency and Computation: Practice and Experience* 17.2-4 (2005), pp. 323–356. DOI: <https://doi.org/10.1002/cpe.938>.
- [98] K. Wette et al. “Deep exploration for continuous gravitational waves at 171–172 Hz in LIGO second observing run data”. In: *Physical Review D* 103.8 (2021), p. 083020. DOI: [10.1103/PhysRevD.103.083020](https://doi.org/10.1103/PhysRevD.103.083020). arXiv: [2103.12976](https://arxiv.org/abs/2103.12976) [gr-qc].
- [99] R. Tenorio et al. *in preparation*. Tech. rep. LIGO-P2100277. LIGO Scientific Collaboration, 2021. URL: <https://dcc.ligo.org/P2100277/>.
- [100] E. J. Gumbel. “Les valeurs extrêmes des distributions statistiques”. fr. In: *Annales de l’institut Henri Poincaré* 5.2 (1935), pp. 115–158. URL: http://www.numdam.org/item/AIHP_1935__5_2_115_0/.
- [101] R. A. Fisher and L. H. C. Tippett. “Limiting forms of the frequency distribution of the largest or smallest member of a sample”. In: *Mathematical Proceedings of the Cambridge Philosophical Society* 24.2 (1928), pp. 180–190. DOI: [10.1017/S0305004100015681](https://doi.org/10.1017/S0305004100015681).
- [102] M. Isi et al. “Establishing the significance of continuous gravitational-wave detections from known pulsars”. In: *Physical Review D* 102.12 (2020), p. 123027. DOI: [10.1103/PhysRevD.102.123027](https://doi.org/10.1103/PhysRevD.102.123027). arXiv: [2010.12612](https://arxiv.org/abs/2010.12612) [gr-qc].
- [103] *Einstein Telescope project*. <http://www.et-gw.eu/>. Accessed: 2021-08-25.

- [104] *CERN Document Server*. <https://cds.cern.ch/>. Accessed: 2021-08-25.
- [105] S. Hild et al. “Sensitivity Studies for Third-Generation Gravitational Wave Observatories”. In: *Classical Quantum Gravity* 28 (2011), p. 094013. DOI: [10.1088/0264-9381/28/9/094013](https://doi.org/10.1088/0264-9381/28/9/094013). arXiv: [1012.0908](https://arxiv.org/abs/1012.0908) [gr-qc].
- [106] B. Sathyaprakash et al. “Scientific Objectives of Einstein Telescope”. In: *Classical Quantum Gravity* 29 (2012). Ed. by Mark Hannam et al. [Erratum: *Class.Quant.Grav.* 30, 079501 (2013)], p. 124013. DOI: [10.1088/0264-9381/29/12/124013](https://doi.org/10.1088/0264-9381/29/12/124013). arXiv: [1206.0331](https://arxiv.org/abs/1206.0331) [gr-qc].